UNIVERSITY OF CALIFORNIA, SAN DIEGO

# Investigating the structure of the core-mantle boundary region using S and P diffracted waves

A dissertation submitted in partial satisfaction of the
requirements for the degree Doctor of Philosophy
in
Earth Sciences

by

Ursula J. Manners

Committee in charge:

Professor Guy Masters, Chair
Professor William Coles
Professor Yuri Fialko
Professor Jeffrey Gee
Professor Peter Shearer

2008

The dissertation of Ursula J. Manners is approved, and it is acceptable in quality and form for publication on microfilm:

_____

_____

_____

_____

_____

Chair

University of California, San Diego

2008

*To my parents*

TABLE OF CONTENTS

LIST OF FIGURES

LIST OF TABLES

# ACKNOWLEDGMENTS

My scientific journey really began in high school, when I had the good fortune of taking Honors Physical Science with Dr. Hermann Prossinger. HPS, as we called it, was the first class that really challenged me. In fact, I believe I did quite poorly on the first test. As my mother tells me, Doc did not initially believe that I was interested in science, but she told him to give me a chance. I suppose I eventually proved I was not just interested in getting good grades, because by the end of the school year, Doc had convinced me to take IB Biology, Physics, and Chemistry, which was well beyond what I needed to graduate. Sadly, we moved to Belgium in my senior year, so I only had the opportunity to take the first year of IB Physics with Doc. But I remember those classes fondly and many of my classmates went on to study science as well, thanks to him.

With happy memories of high school Physics, I started at Brown with the intent of being a Physics major. Somewhere along the line, I lost my passion, bogged down in endless equations and abstract concepts that seemed to have no real meaning. After contemplating changing my major to linguistics, I followed several of my fellow Physics majors and switched over to Geophysics instead. Jan Tullis and Karen Fischer showed me that science could be exciting again and with their encouragement, I started thinking about a Ph.D.

After a detour to be a Peace Corps volunteer in Guinea, I came to Scripps - a little quirkier and not quite adjusted to Western life - and started my life as a grad student. My six years here have been interesting and I am glad I stuck it out. I have met so many interesting people and learned so much, that it has been well worth it.

My time at Scripps has been influenced by so many people, all of whom I wish to thank. Working with Guy has been a formative experience and it is hard to find the right words to thank him. Not only is Guy an amazing seismologist, but he cares about his students. His door was always open and he encouraged me to ask the same stupid questions over and over again. I'm grateful that he didn't give up on me when I was being hopelessly unproductive and that he let me abandon the anisotropy project. I

also feel very lucky that he sent me to CIDER, which helped me become excited about research again. I never would have made it to the end without him. I know we got off to a bit of a rocky start, but I've really enjoyed the last few years.

Special thanks also go to Christine Houser, who understands what it is like to be a Guy student. I do not think I would have survived grad school without Christine. Not many people can discuss the finer points of seismology as well as the possibility of llamas in the lower mantle. She has been a translator, surrogate advisor, cheerleader, and of course, very good friend. She put up with all my phone calls and convinced me many, many times not to drop out of grad school.

I'd also like to thank my committee: Peter Shearer, Jeff Gee, Yuri Fialko, and Bill Coles, for their interest and support in my research. Thanks also to Gabi Laske, who always had comments and advice on my research, and Sophia Akber, who was willing to answer my mineral physics questions. Thanks as well, to my co-authors on my last chapter: Qinya Liu and Jeroen Tromp.

I would also like to thank my many friends from the past six years. In no particular order: my classmates German Prieto and Vince Morton, who shared the pains of the first year of grad school and who drank many a coffee with me at Cups. Bettina Allmann, who shares my love of ballet and has been a great friend. Renee Bulow, my fellow crossword puzzle addict. Linda Warren, who introduced me to the farmer's market. Tegan Blaine, who understood what it was like to be a RPCV and a grad student. My officemates, Leah Ziegler and Sylvain Barbot and particularly their great shoulder rubs, but also, their emotional support. Jill Pearse, for being so much fun to talk to. Lindsay Smitth, for always being available for procrastination in these last few months. Ali La Bonte, for taking me on crazy hiking trips. I'd also like to thank Karen Weitemeyer, Karen Luttrell, Kristin Lawrence, Satoko Oki, Kate Rychert, Nick Harmon, Jen Bowen, Elinor Lichtenberg, Susy McKay, and all the many others I came to know during my time here. A special thank you as well to Jessica Kleiss, Liz Douglass, and Oliver Sun. I looked forward to quartet practice every week. Thanks as well to all the others I played music with: Diana de Leeuw, Ping Wang, Wayne Chen, Lisa Tauxe, and

Steve Cande. I have really enjoyed performing with all of you.

Last, but most certainly not least, I would also like to express my thanks to family, for always being there, no matter what.

Some of the chapters have been submitted for publication. Chapter 2 (Manners, U.J. and G. Masters (2008), A comparison of methods for global teleseismic earthquake relocation.) has been submitted in full for publication in the *Bulletin of the Seismological Society of America*. The dissertation author was the primary investigator and author of this paper. Chapter 3 (Manners, U.J. and G. Masters (2008), An analysis of core-mantle boundary structure using S and P diffracted waves.) has been submitted in full for publication in *Geophysical Journal International*. The dissertation author was the primary investigator and author of this paper. Chapter 4 (Manners, U.J. and G. Masters (2008), Relations between shear velocity and bulk sound speed.) has been submitted in full for publication in *Geophysical Journal International*. The dissertation author was the primary investigator and author of this paper. Chapter 5 (Manners, U.J., Q. Liu, G. Masters, and J. Tromp (2008), Modeling the lowermost mantle using diffracted phases and finite frequency kernels.) has been submitted in full for publication in *Geophysical Journal International*. The dissertation author was the primary investigator and author of this paper.

## VITA

| | |
|---|---|
| 2000 | B.Sc., Geology-Physics/Math<br>Brown University, Providence, RI |
| 2000-2002 | Peace Corps Volunteer<br>Siguiri, Guinea |
| 2002–2008 | Research Assistant<br>Scripps Institution of Oceanography,<br>University of California, San Diego |
| 2008 | Ph.D., Earth Sciences<br>Scripps Institution of Oceanography,<br>University of California, San Diego. |

## FIELDS OF STUDY

Major Field: Seismology

Studies in Seismology:
Professors Peter Shearer and Guy Masters

Studies in Data Analysis:
Professors Cathy Constable and Frank Vernon

Studies in Geodynamics:
Professor David Sandwell

Studies in Physics of Earth Material:
Professors Duncan Agnew and Yuri Fialko

Studies in Gravity and Geomagnitism:
Professors Cathy Constable and Bob Parker

ABSTRACT OF THE DISSERTATION

Investigating the structure of the core-mantle boundary region using S and P diffracted waves

by

Ursula J. Manners
Doctor of Philosophy in Earth Sciences
University of California, San Diego, 2008
Professor Guy Masters, Chair

The base of the mantle is characterized by many unusual features, including the anti-correlation of shear velocity and bulk sound speed. The spatial extent of the anti-correlation, however, is not well determined, due to poor coverage by standard seismic phases. To improve coverage at the base of the mantle, we created a new data set of 27,000 Sdiff and 35,000 Pdiff arrival times from long period seismograms, using a new picking technique. The inclusion of diffracted data in our inversions greatly improves coverage and resolution at the base of the mantle.

Earthquake mislocation is a potentially large source of error in tomographic inversions. We compared three methods of dealing with location error. We find that models made using iterative relocation do not fit the data well, whereas models made using projection and a joint inversion for perturbation in velocity and earthquake location do. An examination of the effects of different relocation techniques on the correlation of shear velocity with bulk sound speed shows that iterative relocations results in lower and possibly negative correlations between shear velocity and bulk sound speed over the entire mantle.

We present the results of inversions using ray theory and finite frequency kernels for our new data set of long period Sdiff and Pdiff travel time measurements. Finite frequency kernels for diffracted phases are quite different from ray theory kernels and

have increased sensitivity to structure at depths well above the CMB. Shear velocity models derived from our data are very similar, with the finite frequency model showing larger amplitudes at the base of the mantle. Compressional velocity models display greater differences in the lower mantle, particularly at shorter wavelengths. To model bulk sound speed, we jointly inverted for shear velocity and bulk sound speed. Bulk sound speed is anti-correlated with shear velocity over most of the base of the mantle, starting at a depth of 2000 km, confirming the results of previous studies. This anti-correlation suggests the presence of chemical or phase heterogeneity at the base of the mantle.

# 1

# Introduction

## 1.1 Motivation

Much of our knowledge of the Earth's interior comes from the travel times of seismic waves, which allow us to determine the velocity structure of the Earth. To first order, the Earth is spherically symmetric, with the largest changes in seismic velocity occurring with as a function of depth. Tomographic inversions of travel times allow us to map the lateral changes in seismic velocity relative to a 1D model of the Earth. The largest amplitude features occur in the upper and lowermost mantle, while the mid-mantle is characterized by lower-amplitude features. One of the most interesting regions of the Earth is the core-mantle boundary (CMB), which separates the solid silicate mantle from the liquid iron core. This region of the lowermost mantle, also known as the D" layer, is defined by a decrease in seismic velocity gradient (Bullen, 1949) and is believed to be a thermal and chemical boundary layer. Understanding the structure and composition of the D" is key to understanding the large-scale dynamics of the Earth.

Studies of the D" layer have shown that it is highly heterogeneous, with many unusual features. The top of the D" is defined by an increase in seismic velocity, which occurs between 150 to 450 km above the base of the mantle (e.g. Lay and Helmberger, 1983; Revenaugh and Jordan, 1991; Kendall and Shearer, 1994). While the D" discontinuity has been observed globally, it is unclear if it a continuous feature (Nataf and

Houard, 1993). Tomographic models show large-scale structures, with amplitudes that are high in comparison to the rest of the mantle (e.g. Grand, 1997; Ritsema et al., 1999; Masters et al., 2000; Antolik et al., 2003). Of particular note are the large, slow velocity anomalies underneath the Pacific and Africa, which normal mode data suggest may also be of higher density (e.g. Ishii and Tromp, 1999, 2001). Smaller scale features include rapid lateral variations in anisotropy (e.g. Garnero, 2000), strong scattering (e.g. Haddon and Cleary, 1974; Bataille et al., 1990; Shearer et al., 1998) and ultra low velocity zones (ULVZs) (Garnero, 2000). Investigations of the relative variations in shear and compressional velocity, given by *R*, where $R = \frac{\partial ln v_s}{\partial ln v_p}$, show that *R* increases with depth. (e.g. Robertson and Woodhouse, 1995, 1996; Masters et al., 2000; Ritsema and van Heijst, 2002). Additionally, studies have found that shear velocity is negatively correlated with bulk sound speed at the base of the mantle, which suggests the presence of chemical or phase heterogeneity (e.g. Su and Dziewonski, 1997; Masters et al., 2000; Antolik et al., 2003; Ishii and Tromp, 2004).

The relative variations of shear velocity and bulk sound speed are of particular interest to us, because they allow us determine the physical cause of a velocity anomaly. Since compressional velocity, $v_p$, is sensitive to both shear and compression, as given by:

$$v_p{}^2 = \frac{1}{\rho}(\kappa + \frac{4}{3}\mu) \tag{1.1}$$

and

$$v_p{}^2 = v_c{}^2 + \frac{4}{3}v_s{}^2 \tag{1.2}$$

we prefer to use bulk sound speed, $v_c$, which isolates the compressional component, such that:

$$v_c = \sqrt{\frac{\kappa}{\rho}} \tag{1.3}$$

where $\kappa$ is the bulk modulus and $\rho$ is density. We then have a velocity analagous to shear velocity, $v_s$, which is:

$$v_s = \sqrt{\frac{\mu}{\rho}} \tag{1.4}$$

where $\mu$ is the shear modulus. Ordinarily, we expect shear velocity and bulk sound speed to be positively correlated, as for a thermal anomaly, where slow velocities are caused by hot material and fast velocities are caused by cold material. However, if shear velocity and bulk sound speed are negatively correlated, the anomaly cannot be explained by thermal effects alone, implying chemical or phase heterogeneity.

Many theories have been proposed to explain the presence of chemical heterogeneity in the lowermost mantle. Suggestions have included iron enrichment due to core-mantle interactions (Knittle and Jeanloz, 1991) or the remains of subducted slabs (e.g. Davies and Gurnis, 1986; Kendall and Silver, 1996), as well as the presence of a compositionally distinct layer at the base of the mantle (Kellogg et al., 1999; van der Hilst and Karason, 1999). Phase heterogeneity may be explained by the recent observations of a phase transition from perovskite to post-perovskite (Murakami et al., 2004; Oganov and Ono, 2004). Post-perovskite is hypothesized to exist at the base of the mantle, although the depth of the transition is strongly temperature dependent. Hence, it is possible that post-perovskite is prevalent throughout the entire lowermost mantle, only exists in isolated regions, or does not exist at all (e.g. Wookey et al., 2005). The properties of post-perovskite provide a favorable explanation for several of the features we see at the base of the mantle. First principles calculations suggest a 1-2% increase in shear velocity, compressional velocity, and density relative to perovskite (Tsuchiya et al., 2004), which could also explain the D" discontinuity. Post-perovskite is also believed to be anisotropic (Tsuchiya et al., 2004), so it could contribute to the strong anisotropic signature at the base of the mantle. Less certain is whether the phase transition to post-perovskite can explain the observed anti-correlation between shear velocity and bulk sound speed, since the phase transition results in an increase in shear velocity, with a corresponding decrease in bulk sound speed, which is the opposite of what has been observed.

Studies of the base of the mantle, however, have been hampered by poor resolution. While the presence of anti-correlation between shear velocity and bulk sound speed is common to most models of the lower mantle (e.g. Su and Dziewonski, 1997;

Masters et al., 2000; Antolik et al., 2003; Ishii and Tromp, 2004), the depth at which the negative correlation starts is poorly constrained. In order to explain the cause of the negative correlation, we need to first have a better constraint on the large-scale structure of the lowermost mantle and the spatial extent of the negative correlation between shear velocity and bulk sound speed.

Despite increasingly large data sets of travel time measurements, our understanding of the large-scale structure of the lowermost mantle is poor, due to limited sampling by standard seismic phases. Figure 1.1 shows a plot of S and P travel time residuals binned in caps of $5^\circ$ radius and plotted at their turning point. Coverage is good only in the Northern Hemisphere, with parts of the Southern Hemisphere remaining entirely unsampled. While some of the gaps can be filled in using core-reflected or transmitted phases, such as ScS-S and PKP, holes in coverage remain, particularly for our P data. To improve coverage, we have created a new data set of diffracted S and P travel times using cluster analysis (Houser et al., 2008). Since diffracted waves travel along the CMB, they are particularly well-suited to a study of the base of the mantle (Figure 1.2).

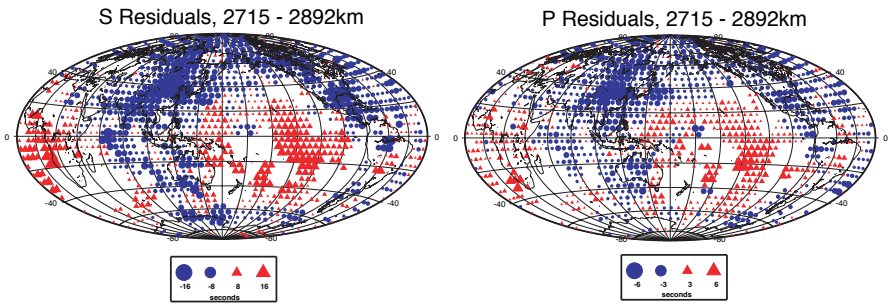


**Figure 1.1**: Slices of the base of the mantle showing S (left) and P (right) residuals binned in $5^o$ caps and plotted at their turning points.

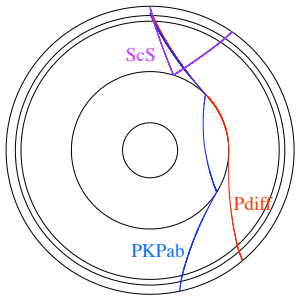


**Figure 1.2**: A cross-section of the Earth showing phases which sample the base of the mantle.

## 1.2 Thesis Organization

Travel time measurements require knowledge of the location of both the earthquake and the receiver. While receiver location is well known, determining the locations of earthquakes is more difficult. Organizations such as the International Seismological Centre and the National Earthquake Information Center publish global catalogues of earthquake locations and show typical differences in location of 15 km or more. If location error is not corrected for, it can be propagated into velocity structure. Earthquake mislocation is a particularly large source of error for our P data, because the size of the error is similar in size to the signal (Bolton and Masters, 2001). Consequently, location error must be dealt with prior to or during inversion. In Chapter 2, we discuss various techniques for dealing with location error in global tomography and present a new set of earthquake locations, which are then used in subsequent chapters.

Having determined a new set of earthquake locations, we can now discuss the diffracted data sets. Chapter 3 details how we measured the travel times and examines how well coverage at the base of the mantle is improved. We also present new models of the base of the mantle, as well as the results of a joint inversion for shear velocity and bulk sound speed.

In Chapter 4, we examine the correlation between shear velocity and bulk sound speed in the lower mantle in more detail. We present a new technique for con-

straining bulk sound speed, by combining S and P residuals for common source and receiver pairs. Using this technique, we also investigate how different earthquake locations affect the depth extent of the negative correlation between shear velocity and bulk sound speed. We also present the results of a joint inversion for shear velocity and bulk sound speed using projected data.

The work thus far presented has been done using ray theory. Ray theory assumes that waves propagate as rays through the Earth, with sensitivity to structure only along the ray path. Recently, global tomographic models have been made using finite-frequency theory (e.g. Zhou et al., 2006; Montelli et al., 2006), which takes into account the sensitivity to structure off the ray path as well as wave front healing. Finite frequency kernels for diffracted waves show that sensitivity to structure can extend as much as 500 km above the CMB, which could potentially change the results of our inversions. In Chapter 5, we apply the sensitivity kernels of Liu and Tromp (2008) to our new data and compare the resulting models to our ray theory models. In order to investigate how finite frequency kernels change the depth extent of the negative correlation between shear velocity and bulk sound speed, we also do another joint inversion for shear velocity and bulk sound speed using the finite-frequency kernels. We conclude the thesis with a summary of the results.

# 2

# A comparison of methods for global teleseismic earthquake relocation

**Abstract**

Earthquake mislocation is a potentially large source of error in tomographic inversions. Existing methods of correcting for location error include projecting the data to make them insensitive to location, and iterative relocation, in which seismic arrival times are iteratively relocated to solve for location. Projection, however, is computationally expensive, since it involves taking linear combinations of the data thus making potentially sparse matrices dense. Iterative relocation preserves the sparseness of the matrix, however, it does not always return the correct answer, since there is a trade-off between location and structure. It is also possible to correct for location error by jointly inverting for perturbations in velocity and event location. We test how well projection, iterative relocation, and joint inversion work by relocating approximately 6500 events of magnitude 5.5 and larger, occurring between 1976 and 2005, using the arrival times of P, PP-P, Pdiff, S, SS-S, ScS-S, and Sdiff data sets. In order to better constrain focal depth, we include a new data set of depth phases (pP-P, sP-P, and sS-S). The three methods of relocation are first tested on synthetic data. We find that models made using iterative relocation do not fit the data well, whereas projection and joint inversion do. An examination of the effects of different relocation techniques on the correlation of shear velocity with bulk sound speed shows that iterative relocations results in lower

and possibly negative correlations between shear velocity and bulk sound speed over the entire mantle. We then present the results of projection and joint inversion on real data. Both projection and joint inversion result in similar models, which fit the data well. The addition of depth phases improves constraints on depth and results in a systematic pattern of residuals in subduction zones. The relocated earthquakes are systematically shifted away from the slab in subduction zones, particularly in the Aleutians.

## 2.1 Introduction

Earthquake mislocation is a major source of error in the travel time data sets used for tomographic models. Global compilations of earthquake locations are available through organizations such as the International Seismological Centre (ISC) and the National Earthquake Information Center (NEIC), which primarily use teleseismic arrival times to determine hypocenter locations. However, the quality of the catalogue locations is uneven, due to problems with phase misidentification, uneven distribution of earthquakes and receivers, errors in the reference earth models, and lateral variations in velocity (Engdahl et al., 1998). Creager and Boyd (1992) show that the epicenters of subduction zone earthquakes can be systematically incorrect by as much as 40 km. Focal depths, in particular, are poorly constrained and can be offset by several tens of kilometers (Dziewonski and Anderson, 1983; Engdahl and Gubbins, 1987; van der Hilst and Engdahl, 1992). Furthermore, both the ISC and the NEIC use default depths when focal depth cannot be resolved (Bolton et al., 2006). The magnitude of location error can change predicted arrival times by approximately one second, which is similar in size to the signal of 3D structure in our P data (Bolton and Masters, 2001). In fact, Davies (1992) estimates that 35% of travel-time variance for teleseismic earthquakes is due to mislocation. If not corrected for, this error is then mapped into tomographic inversions and interpreted as 3D velocity structure.

A failure to properly deal with location error can have ramifications beyond simply adding structure to our P models, but can also affect our interpretation of the

processes in the mantle. The question of slab penetration into the lower mantle, for example, influences our interpretation of mantle convection. Creager and Boyd (1992) note that slabs appear in the lower mantle in models in which event location has been properly handled and suggest that the absence of slabs in the lower mantle in some tomographic models may be due to bias as a result of event mislocation. The correlation of shear velocity and bulk sound speed, as another example, can tell us about the physical cause of velocity anomalies in the mantle. Inversions for bulk sound speed, however, require P travel times, and are thus sensitive to location error. Several studies (e.g. Antolik et al., 2003; Masters et al., 2000; Su and Dziewonski, 1997) have examined the correlation between shear velocity and bulk sound speed in the mantle and have shown that the lower mantle is anti-correlated. However, there is disagreement over the depth at which the anti-correlation starts. Location error, which has not been properly accounted for, may explain this discrepancy.

Attempts have been made to improve the global catalogues. Engdahl et al. (1998) reprocessed the ISC data set by including later phase arrival times, depth phases, and station corrections, as well as using a more up-to-date 1D model (ak135, Kennett et al., 1995). While the reprocessing improves location accuracy, the effects of un-modeled lateral heterogeneity still contribute to location error (Nicholson et al., 2004; Nicholson, 2006). Lateral heterogeneity can be accounted for by using 3D models in relocation - an approach which has been used with success (e.g. Antolik et al., 2001; Ritzwoller et al., 2003; Smith and Ekström, 1996). Other approaches for improving global catalogues include using nonlinear techniques (e.g. Kennett, 2006; Rodi, 2006). However, as yet, these have not been applied to the ISC and NEIC data sets. Thus, we can not rely on global catalogues to provide accurate enough earthquake locations for our inversions. This necessitates another approach for dealing with location error.

A variety of approaches have been used to deal with location error in global tomographic inversions. One such approach is to project the data for each event in order to make linear combinations of the data that are insensitive to location (e.g. Masters et al., 2000; Houser et al., 2008). Projection, however, is computationally expensive.

Ordinarily, travel time matrices are sparse, since the non-zero elements for each row is equal to the number of blocks that the ray travels through, and thus do not require a lot of computer power to invert them. Projected matrices, however, are not, since each projected datum is a linear combination of all data for an event. As a result, inversions take significantly longer to run and require more memory, which is a drawback.

An alternative, and less computationally expensive approach, is iterative relocation (e.g. Dziewonski, 1984; Su et al., 1994; Su and Dziewonski, 1997). Source locations are relocated using least squares, prior to inverting for velocity structure. The travel times are then corrected for lateral heterogeneity, using the new velocity model, and the process is repeated until it converges. Unlike projection, the sparseness of the matrices is preserved. However, the problem with iterative relocation is that there is a trade off between structure and mislocation (e.g. Pavlis and Booker, 1980). By trying to force all of the signal to initially be due to location error, velocity structure is mapped into location error. Furthermore, when using travel times, hypocenters can be easily trapped into local minima (Kennett, 2006; Nicholson, 2006). Additionally, Thurber (1992) shows that a failure to explicitly couple hypocenters to velocity models in inversions can lead to systematically biased velocity models, as well as resulting in velocity perturbations being underestimated by a factor of four. Kissling (1988) also shows that solving the hypocenter and velocity structure problems separately can result in artificial velocity anomalies being produced in error.

This points to the need for an alternate method of dealing with location error. Rather than solving separately for perturbations in velocity and location, we solve for both, simultaneously. Global tomographic inversions that include perturbation for location are not new (e.g. Bijwaard et al., 1998; Vasco and Johnson, 1998; Li et al., 2006) , however, their accuracy have not been properly tested on global data sets. Several studies (e.g. Buland, 1976; Pavlis and Booker, 1980; Spencer and Gubbins, 1980; Engdahl and Gubbins, 1987) do test various approaches to joint inversions on synthetic data, however, these were tested on very small data sets. With more computational power available to us now, we can examine how well a joint inversion for location and velocity

works with a global data set.

We examine the efficacy of the three methods discussed above of dealing with location error, by testing them on a data set of teleseismic synthetic travel times. To improve constraints on depth, we include S and P travel times, as well as a new data set of depth phases. We then present the results of inversions using our real data.

## 2.2 Method

We test three methods of dealing with location error. In the tomographic inversions described below, the models are parameterized as 18 layers, which are 200 km thick in the lower mantle and 100 km thick in the upper mantle. Each layer is divided into $4^o$ equal area blocks. The models are all inverted using LSQR (Paige and Saunders, 1973). First difference smoothing is applied both radially and laterally.

### 2.2.1 Projection

The first method that we test is projection, in which we take linear combinations of data that are insensitive to location. A vector of travel time residuals, $\delta\mathbf{t}$, can be described as:

$$\delta\mathbf{t} = \mathbf{A} \cdot \delta\mathbf{h} + \mathbf{B} \cdot \delta\mathbf{v} \tag{2.1}$$

where $\mathbf{A}$ is a matrix containing the travel time derivatives with respect to location, $\delta\mathbf{h}$ is a vector representing the perturbation in location and origin time, $\mathbf{B}$ is the matrix of ray, and $\delta\mathbf{v}$ is a vector representing the 3D perturbations in velocity. Ray paths are calculated relative to ak135. We multiply the above equation with a projection matrix, $\mathbf{P}$, which is chosen such that $\mathbf{P} \cdot \mathbf{A}$ is equal to zero and that $\mathbf{P} \cdot \mathbf{E}\mathbf{P}^{\mathbf{T}}$ is diagonal, where $\mathbf{E}$ is the covariance matrix of the observations, meaning that the projected data are independent. We thus end up with the equation

$$\mathbf{P} \cdot \delta\mathbf{t} = \mathbf{P} \cdot \mathbf{B} \cdot \delta\mathbf{v} \tag{2.2}$$

where $\mathbf{P} \cdot \delta\mathbf{t}$ are now insensitive to location. The projected travel times are then inverted. Our S and P data sets are projected and inverted separately.

### 2.2.2 Iterative Relocation

A standard method for solving equation (2.1) is to solve it iteratively. We first solve the first half of the equation, such that

$$\delta\mathbf{t} = \mathbf{A} \cdot \delta\mathbf{h} \rightarrow \delta\mathbf{t_1} = \delta\mathbf{t} - \mathbf{A} \cdot \delta\mathbf{h} \tag{2.3}$$

This gives us a new set of travel time residuals, $\delta\mathbf{t_1}$, which are inverted to obtain independent P and S velocity models, as given by:

$$\delta\mathbf{t_1} = \mathbf{B} \cdot \delta\mathbf{v} \rightarrow \mathbf{c_1} \tag{2.4}$$

The resulting model prediction, $\mathbf{c_1}$, is subtracted from the travel time residuals and we repeat the process, this time solving:

$$\delta\mathbf{t_1} - \mathbf{c_1} = \mathbf{A} \cdot \delta\mathbf{h} \rightarrow \delta\mathbf{t_2} \tag{2.5}$$

The process is repeated until it converges, which typically happens after just a few iterations. While inverting for perturbation to location, we combine all of our data sets, since the addition of S phases helps to constrain location. The inversions for velocity structure are done for S and P separately.

### 2.2.3 Joint Inversion

The third method that we tested was a joint inversion for structure and location, such that

$$\delta\mathbf{t} = \begin{bmatrix} \lambda\mathbf{A} & \mathbf{B} \end{bmatrix} \begin{bmatrix} \lambda^{-1}\delta\mathbf{h} \\ \delta\mathbf{v} \end{bmatrix} \tag{2.6}$$

Changing the value of $\lambda$ allows us to control how much we want to weight the relocation versus the velocity part of the inversion. A large value of $\lambda$ forces most of the signal to go into the relocation, whereas a small value weights the inversion towards the velocity model. All data sets are inverted simultaneously.

### 2.2.4 Azimuthal Coverage

Poor azimuthal coverage can result in poorly located events. Thus, it is important to restrict relocations to events which are well-constrained. A common way to ensure good azimuthal coverage is to limit the data set to events which have measurements in at least three quadrants (e.g. Su and Dziewonski, 1997). We find that by limiting our data set to those events which have at least ten measurements, the vast majority of events meet the three quadrant condition, making this condition a suitable alternative. Tests on synthetic data also show that using the three quadrant condition, as opposed to the 10 measurement minimum has no effect on the results. Placing a lower bound on the number of measurements also ensures that there are enough data to constrain the inversion.

### 2.2.5 Data

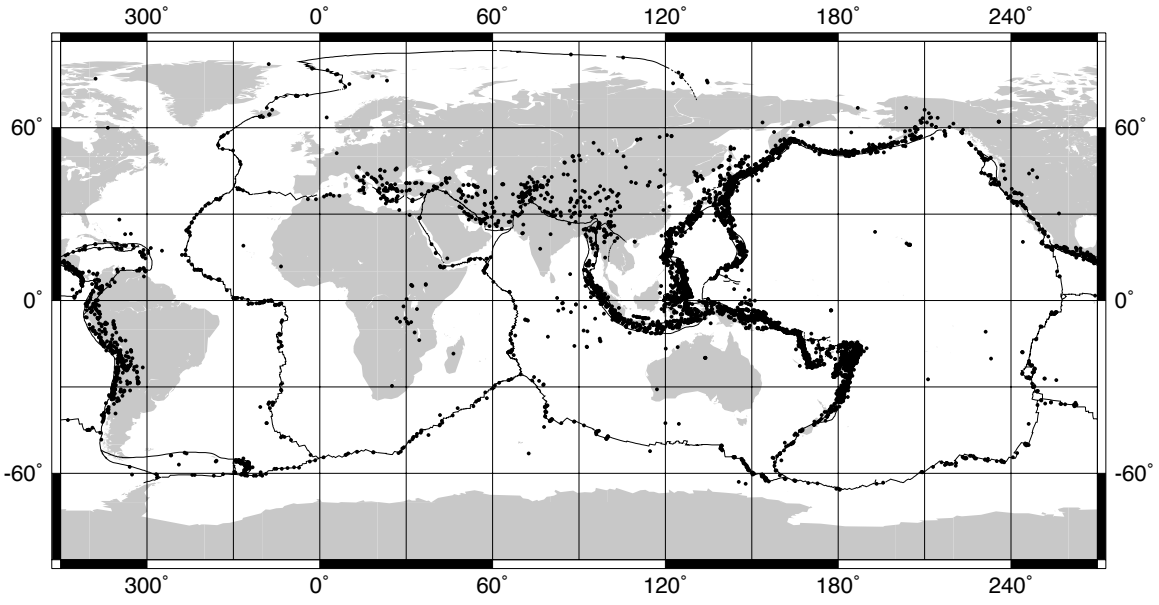


**Figure 2.1**: Initial earthquake locations for events occurring between 1976 and 2005. Events must have a minimum of ten measurements to be included.

Our data sets consist of existing S, Sdiff, SS-S, ScS-S, P, Pdiff, and PP-P travel

times (see Table 2.1), which were picked manually or using cluster analysis (Houser et al., 2008). The measurements are made on long-period data, which have a dominant period of 20s. We also include surface wave dispersion measurements (Masters et al., 2000, *Laske*, personal communication) to constrain structure in the upper mantle.

The use of long-period data points to yet another reason why we must relocate. The NEIC and ISC locations are determined using short-period data, which "see" arrivals coming from the onset of rupture earlier, giving an earlier origin time and different location than long-period data. This offset must be corrected for during relocation. Our data set corresponds to roughly 6500 events, occurring between 1976 and ending 2005 (see Figure 2.1). The events are all of magnitude 5.5 or greater, although events with a moment magnitude greater than 7.8 are excluded. The benefit of using multiple data sets is that the travel-time derivatives for different phases (particularly S and P) are significantly different with respect to distance, which places a better constraint on location (Engdahl et al., 1998; Engdahl, 2006; Kennett, 2006). Errors are assigned to the data based on the quality of the travel time measurements. The data are weighted by their errors in the inversion, meaning that better quality data is weighted more heavily in the inversion. The data are corrected for the ellipticity of the Earth (Kennett and Gudmundsson, 1996) as well as for crustal structure, using CRUST 2.0 (Bassin et al., 2000).

Although our data are initially picked using the NEIC locations, we use the Engdahl et al. (1998) (EHB) locations as a starting point. Both the NEIC and ISC catalogues use the JB travel time tables (Jeffreys and Bullen, 1940) to calculate arrival times. However, the JB travel-time tables are not consistent with observed travel times (Engdahl et al., 1998). Thus, the use of ak135 in preferable, since it was constructed to provide a good fit to the travel times of 19 seismic phases (Kennett et al., 1995). Since we pick our data relative to ak135, using the EHB locations removes any systematic misfit in origin time due to different reference models. Furthermore, it is believed that the EHB locations are closer to the true locations, increasing the likelihood of finding the true location rather than remaining in a local minimum.

**Table 2.1**: Phases and number of measurements included in study

| Phase | Number of Picks | Years |
|---|---|---|
| P | 182724 | 1976 - 2005 |
| Pdiff | 34774 | 1986 - 2005 |
| PP-P | 26116 | 1976 - 1999 |
| S | 169832 | 1976 - 2005 |
| Sdiff | 26706 | 1986 - 2005 |
| SS-S | 32266 | 1976 - 2003 |
| ScS-S | 26840 | 1976 - 2003 |
| pP-P | 23184 | 1976 - 2005 |
| sP-P | 26615 | 1976 - 2005 |
| sS-S | 30223 | 1976 - 2005 |

### 2.2.6 Depth Phase Measurements

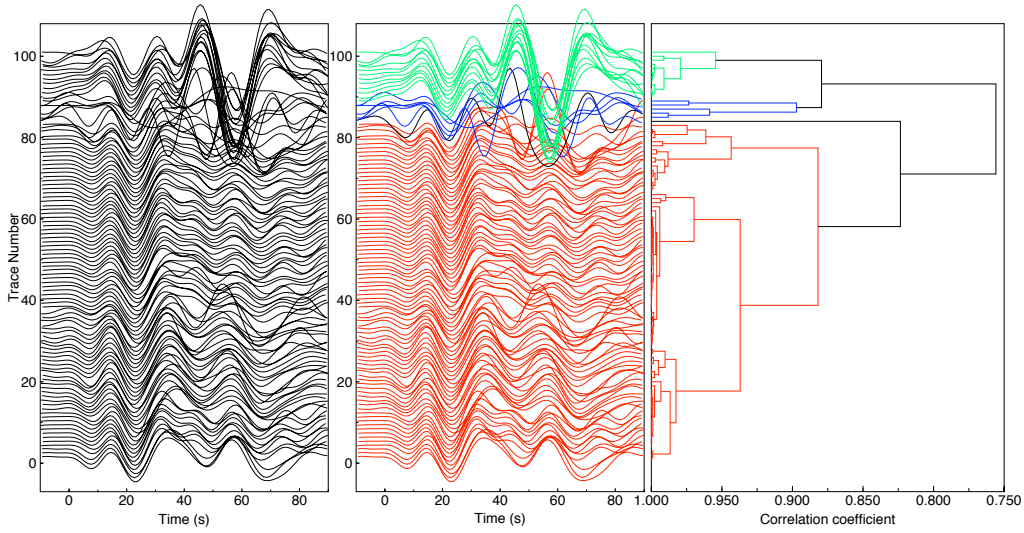


**Figure 2.2**: All pP waveforms for an event in 1998 aligned along their predicted arrival times (left). The same pP waveforms grouped according to their similarity giving us two groups (red and green) (right). The P waveforms are then added to each cluster and all the waveforms within the cluster are cross-correlated again, to give the relative arrival times of pP and P for the entire cluster.

To better constrain focal depth, we include a new data set of depth phase travel times for pP-P, sP-P, and sS-S. Since depth phases initially travel up, their travel time derivatives with respect to depth are of opposite sign to those of direct phases, allowing a more precise determination of depth (Engdahl and Gubbins, 1987; Engdahl et al.,

1998; van der Hilst and Engdahl, 1992; Engdahl, 2006; Kennett, 2006). The depth phase arrival times were measured using a variant of cluster analysis, altered to handle differential phases.

First, the waveforms of the chosen depth phase are cross-correlated and grouped into clusters, based on waveform similarity (see Figure 2.2). Each cluster of waveforms is then cross-correlated a second time with the addition of the first arrivals (i.e. S for sS and P for pP and sP), which are shifted by their predicted arrival time to align with their corresponding depth phase. The second cross-correlation gives the relative arrival times of all of the depth phases and first arrivals in the cluster. These relative arrival times are then inverted, using LSQR, to determine the differential arrival times. Using this method, we were able to create a data set of approximately 23,000 pP-P, 26,500 sP-P, and 30,000 sS-S arrival times. To avoid contamination with the first arrival, we used events with a depth greater than 100 km for sP-P and pP-P and deeper than 80 km for sS-S.

### 2.2.7 Station Corrections

Unmodeled lateral heterogeneity can result in systematic shifts in hypocenter locations. Variations in crustal and upper mantle structure, in particular, can be large and introduce large error into locations determined from 1D models. To counteract this, we have experimented with applying corrections to account for differences in crustal and upper mantle structure underneath seismic stations. The corrections were calculated by combining all the relative P arrival times that are measured using cluster analysis for all stations. The relative arrival times are then inverted to find the best set of differential times for all stations. A separate set of station corrections for the S data was made as well. A map of the P station corrections can be seen in Figure 2.3. The pattern of the corrections reflects mantle and crust structure beneath the station, with the slowest residuals occurring in areas of rifting, such as Eastern African and the Western US.

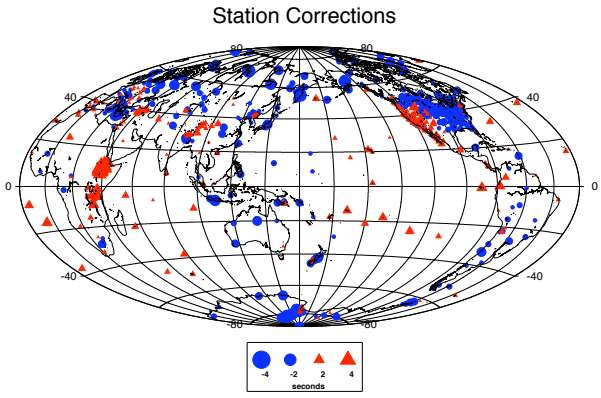


**Figure 2.3**: Station corrections for P data.

## 2.3 Tests With Synthetic Data

We test the different relocation methods on two different synthetic data sets. The first synthetic data set was created by tracing rays through a 1D model (ak135). The second synthetic data set includes a 3D velocity component as well. We used a shear model made using our existing S, Sdiff, SS-S, ScS-S, sS-S data sets to create our 3D S data sets. The P data sets were traced through a scaled version of the shear model. To mimic the effects of mislocation, we then randomly perturbed the origin time and location (latitude, longitude, and depth) of the locations. The average mislocation was 4s for time, 10km for latitude and longitude, and 8 km for depth.

### 2.3.1 1D Synthetics

The simplest test of our relocation methods is to use synthetic data that have no 3D signal. For this test, we used only the S and P data. Both iterative relocation and the joint inversion successfully relocated the perturbed 1D synthetic data in one iteration. For the joint inversion, we weighted the model and the location part of the model equally (ie. lambda was set equal to one). For the joint inversion, the rms misfits to the origin time, x direction, y direction, and depth were 0.37 s, 0.31 km, 0.27 km, and 2.1 km, respectively. For iterative relocation, these values are 0.34s, 0.32 km, 0.34 km, and 2.9 km, respectively.

### 2.3.2 3D Synthetics

The tests using 3D synthetic data produced more varied results and demonstrated some of the problems of the various approaches.

**Projection**

To test if projection is indeed insensitive to location error, we projected both our perturbed 3D synthetic S and P data sets. To determine how well the models fit the data, we look at the $\chi^2/N$ fit. In our experiments with the synthetic data, we use the observed errors for our data. Since the synthetic signals are small compared to the observed errors, the expected $\chi^2$ value should be close to zero. As expected, the fit of the models to the data is extremely good, with a $\chi^2$ value of 0.04 for the S model and 0.01 for the P data. As a test of how well we are able to determine the original velocity structure, we correlate our models with the original models that we used to make the 3D synthetic data (see Figures 2.4 and 2.5). Prior to examining the correlation of our projected models, it is worth looking at the correlation of the models made using the unperturbed synthetic data with the original models (black line), as this represents our best estimate of velocity structure. Both the S and P models correlate well with the original models in the lower mantle, with correlation values of almost 1. In the upper mantle, correlation values decrease to 0.6, since we did not use surface waves, which provide the best constraint on upper mantle structure, in our synthetic experiments. The correlation of the projected P and S models with the original models is almost identical to the correlation of the original models with the unperturbed synthetic data, indicating that projection is a safe approach to dealing with location error.

**Iterative Relocation**

While iterative relocation was able to return the correct solution for 1D synthetic data, it did not do as well with synthetic data that had an additional signal from 3D structure. Many of the events were poorly located, with shifts in origin time of several tens of seconds and shifts in location of over 100 km. The large shifts in depth also

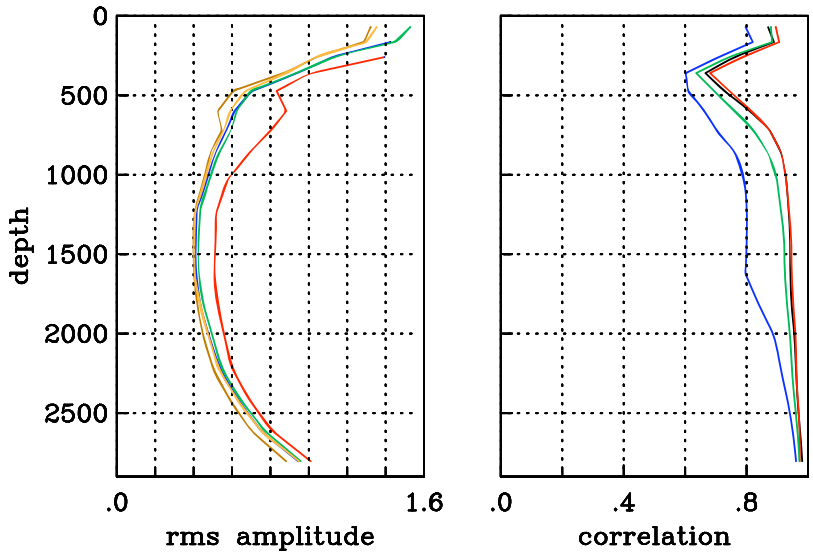


**Figure 2.4**: Amplitude and correlation of synthetic S models. The red line shows the amplitude of the original model, from which the synthetic data were made. The amplitudes are slightly lower for the unperturbed synthetic model (blue), projected (green), iteratively relocated (brown), and jointly inverted (yellow) models. The unperturbed synthetic (black), projected (red), and jointly inverted (green) models correlate well with the original model in the lower mantle. The lower correlation in the upper mantle reflects the absence of surface wave data, which were not used in the synthetic experiments. The iteratively relocated model (blue) correlates less well.

resulted in roughly 2000 above-ground earthquakes. Since throwing out all the events with negative depth would represent a large loss of data, we tried a number of ways of constraining the inversion.

To constrain the inversion, we added a constraint matrix to the bottom of the matrix, which prevents large shifts in position and time, unless really required by the data, as given by:

$$\begin{bmatrix} 0 \\ 0 \\ 0 \\ 0 \end{bmatrix} = \begin{bmatrix} 1/c_1 & 0 & 0 & 0 \\ 0 & 1/c_2 & 0 & 0 \\ 0 & 0 & 1/c_3 & 0 \\ 0 & 0 & 0 & 1/c_4 \end{bmatrix} \begin{bmatrix} \delta z \\ \delta x \\ \delta y \\ \delta t \end{bmatrix} \tag{2.7}$$

The strength of the constraint on displacement in depth, x direction, y direction, and

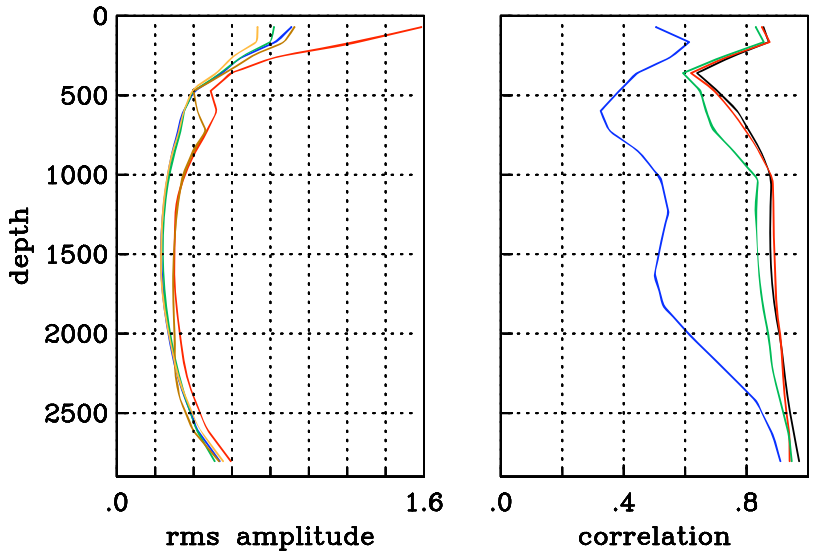


**Figure 2.5**: Amplitude and correlation of synthetic P models. The red line shows the amplitude of the original model, from which the synthetic data were made. The amplitudes are slightly lower for the unperturbed synthetic model (blue), projected (green), iteratively relocated (brown), and jointly inverted (yellow) models. The unperturbed synthetic (black), projected (red), and jointly inverted (green) models correlate well with the original model in the lower mantle. The lower correlation in the upper mantle reflects the absence of surface wave data, which were not used in the synthetic experiments. The iteratively relocated model (blue) correlates less well.

origin time is set by changing the values of $c_1$, $c_2$, $c_3$, and $c_4$, respectively. We used a constraint of 4 seconds for time, 10 km for depth, and 15 km for latitude and longitude. These initial constraints were found to allow the events to move within the range predicted by the perturbed locations. Since depth phases provide a stronger constraint on depth, events which have depth phase measurements were given a weaker constraint of 50 km for depth. Using these constraints, we reduced the number of above ground earthquakes to 1377, which is still 20% of the total number of events. In order to reduce the number of above-ground earthquakes to less that 10% of the data set, the depth constraint had to be reduced to 1 km, resulting in 99 above-ground earthquakes. With suitable constraints in place, we found that the models converged after two iterations, with a significant improvement in $\chi^2$ fit of the models to the data in the second iteration. This improvement in fit suggests that doing only a single iteration of relocation, as was

done in Su and Dziewonski (1997), is not a safe approach. The fit of the models to the data can be seen in Table 2.2. For the P model, the fit of the model to the data is around 0.2, however, the velocity model does not correlate well with the models made using the original unperturbed synthetic data, with a correlation of less than 0.6 for most of the mantle (Figure 2.5). The correlation at the base of the mantle was close to one and the model fit the diffracted data well, suggesting that the diffracted data are able to constrain the structure at the base of the mantle, despite location error. A comparison of the features in the original and relocated models shows significant change in the velocity structure of the mid-mantle. In particular, there are very strong fast velocity structures at the top of the lower mantle, which do not exist in the original model. The low velocity zones in the mid-Pacific are also much smaller in scale in the iteratively relocated model. The presence of these new features suggests that velocity structure is being mapped into mislocation. For the S model, the fit to the data is worse, with a $\chi^2$ value of only 0.46 for the S data. However, the resulting model does correlate reasonably well with the original model, with a correlation value above 0.8 for the entire mantle. This is not surprising, since, unlike the P data, the S signal from 3D structure is larger than the location error, and thus S models are less affected by location error. Unlike the P model, the iteratively relocated S model does not have any artificial structures in it. Again, the correlation and fit at the base of the mantle are better than the rest of the mantle, implying that the diffracted data do a good job of constraining structure at the base of the mantle.

A major source of error, when attempting to relocate earthquakes is unmodeled lateral heterogeneity. Since we are using a 1D model in our first iteration, we attempted to correct for this by using station corrections, which represent mantle structure beneath each station. Using stations corrections is also a better test of Su and Dziewonski (1997) approach, since they corrected for mantle structure in the first iteration by using an existing 3D model. We determined station corrections by calculating the median residual at each station for the synthetic P and S data sets. The mean station correction was then subtracted out of the P and the S station corrections, respectively, to ensure a mean of zero for the corrections. We found that the station corrections did not

improve the fit of the model to the data, although the station corrections provide a good representation of mantle structure (see Table 2.2). The resulting models look very similar to those made without station corrections. In particular, the unusual features noted in the earlier P model are still present, indicating that station corrections do not prevent location error from being mapped into structure. These results are in agreement with Antolik et al. (2001), who found that the addition of station corrections to a 1D model did not significantly improve the rms misfit to known locations.

In addition to station corrections, we tried a number of other approaches to better constrain the inversion. Since the S and P data sets have different means, we tried demeaning the data sets prior to inversions. We also tried removing the average residuals per event prior to relocation. Neither of these approaches improved the results. The failure to return the true location could be due to locations being trapped in local minima and suggests that this approach is not suitable for 3D data.

### 2.3.3 Joint Inversion

We tested the joint inversion on the perturbed 3D synthetic data and found that it was able to return the events to their original locations. The data were inverted for a range of different weights ($\lambda$), to determine the optimal weighting of model versus location. We found that equally weighting the location and velocity parts of the model (ie. setting $\lambda$ equal to one), produced the best results. This value was chosen by looking at how close the relocated locations were to the original unperturbed locations, as well as looking at the $\chi^2$ fit of the model to the data. Weighting the velocity part of the model more heavily, by setting $\lambda$ equal to 0.1, prevented the perturbed locations from moving to their original locations. Weighting the location part of the model more allowed the locations to move too much and mapped some of the velocity structure into location. Similarly to the iterative relocation approach, some of the events were poorly constrained, resulting in 47 above-ground earthquakes. However, since this represents less than 1% of the data set, it was not deemed necessary to constrain the inversion. The resulting models, using a weighting of 1, correlated well with models made using the

original data sets, with a correlation greater than 0.9 in the entire mantle (see Figures 2.4 and 2.5). The fit of the model to the data sets can be seen in Table 2.2. The fit of the the model to the data was good for all the data sets except for the Pdiff data. The poorer fit of the model to the Pdiff data is probably due to the larger errors assigned to the Pdiff data, meaning that they are weighted less in the inversion.

**Table 2.2**: $\chi^2$ fit of models to synthetic data for various test cases. It. reloc. gives the fits for the iteratively relocated models. It. Reloc. w/stat is the iterative relocation with the addition of station corrections. Joint, no const. indicates the fits for models from the joint inversion with no constraint on locations. Joint, 2.5 km is the fit for models from the joint version in which the depth displacement has been constrained to 2.5 km (see equation 2.7).

| Phase | It. Reloc. | It. Reloc. w/ stat. | Joint, no const. | Joint, 2.5 km |
|---|---|---|---|---|
| P | 0.24 | 0.22 | 0.06 | 0.08 |
| Pdiff | 0.13 | 0.14 | 0.46 | 0.43 |
| PP-P | 0.22 | 0.24 | 0.07 | 0.07 |
| pP-P | 0.17 | 0.16 | 0.06 | 0.06 |
| S | 0.46 | 0.38 | 0.12 | 0.13 |
| Sdiff | 0.13 | 0.11 | 0.13 | 0.13 |
| SS-S | 0.34 | 0.37 | 0.15 | 0.15 |
| ScS-S | 0.28 | 0.25 | 0.10 | 0.10 |
| sS-S | 0.21 | 0.21 | 0.10 | 0.09 |

## 2.4 Effects on Bulk Sound Speed

As noted earlier, location error can also affect our interpretation of bulk sound speed. As a simple test, we can create bulk sound speed models from our synthetic S and P models and see how well they correlate using the different methods of relocation. To create bulk sound speed models, we use :

$$v_c{}^2 = v_p{}^2 - \frac{4}{3} v_s{}^2 \tag{2.8}$$

The resulting bulk sound speed model can then be correlated with the synthetic S model. Although Antolik et al. (2003) did create a bulk sound speed model by combining their

shear and compressional models in this fashion, most bulk sound speed models are typically created by jointly inverting for bulk sound speed and shear velocity. Nevertheless, using this method does provide us a with a basic test.

We created four different bulk sound speed models for our three different methods of relocation as well as a model of our original, unperturbed synthetic data. The resulting correlations can be seen in Figure 2.6. We see that the models made using projection and joint inversion show similar correlation values to the original, unperturbed shear and bulk sound speed models. It is interesting to note that all of these models have a correlation of approximately 0.6, although the expected correlation is one, since the synthetic P data were made using a scaled shear model. We made a fifth bulk sound speed model by jointly inverting for shear velocity and bulk sound speed, using the unperturbed synthetic data (brown line). The correlation of these two models is 0.9, which is much closer to the expected results, demonstrating that combining separate S and P models to obtain a bulk speed model is not a safe approach. The models made using iterative relocation, however, are distinctly less well correlated and have a correlation of only 0.4 throughout most of the mantle. Thus, iterative relocation can result in lower and possibly negative correlations between shear velocity and bulk sound speed over the entire mantle and skew results.

In conclusion, our synthetic tests demonstrate that iterative relocation is not a safe approach to the mislocation problem, even with an initial correction for 3D structure or the use of station corrections. Both projection and joint inversions for velocity and hypocenter are viable alternatives. This is in agreement with tests by Thurber (1992), who uses synthetic data to show that joint inversions for locations and velocity models can produce better results than when the velocity and location problems are solved separately.

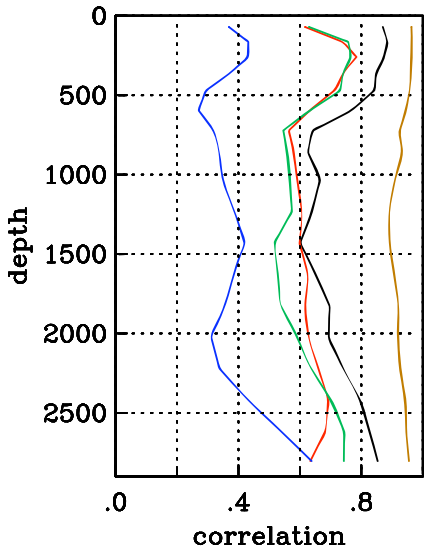


**Figure 2.6**: Correlation of bulk sound speed with shear velocity for synthetic models using the unperturbed (black), iteratively relocated (blue), projected (red) and jointly relocated (green) synthetic data. The brown line shows the same correlation but for models obtained by doing a joint inversion for shear velocity and bulk sound speed using the unperturbed synthetic data.

## 2.5 Real Data

Having tested the three methods of dealing location error on synthetic data, we now jointly invert our real data and compare it to the results of our inverted projected data.

### 2.5.1 Projection

Figures 2.7 and 2.8 show the results of our projected P and S models for different layers in the mantle. The velocity perturbations are relative to ak135. The fit of all the projected P data sets to the projected P model is 0.57. For the real data, a $\chi^2$ fit of 1 indicates that we have fit the data well. The rather low values here indicate that the errors are probably too large for the P data. The fit of the P model to just the projected P data is 0.56, reflecting that the P data dominate the signal, since the data set is so much larger. For the S model, the fit is 1.06 for all the projected S data sets and 1.05 for the

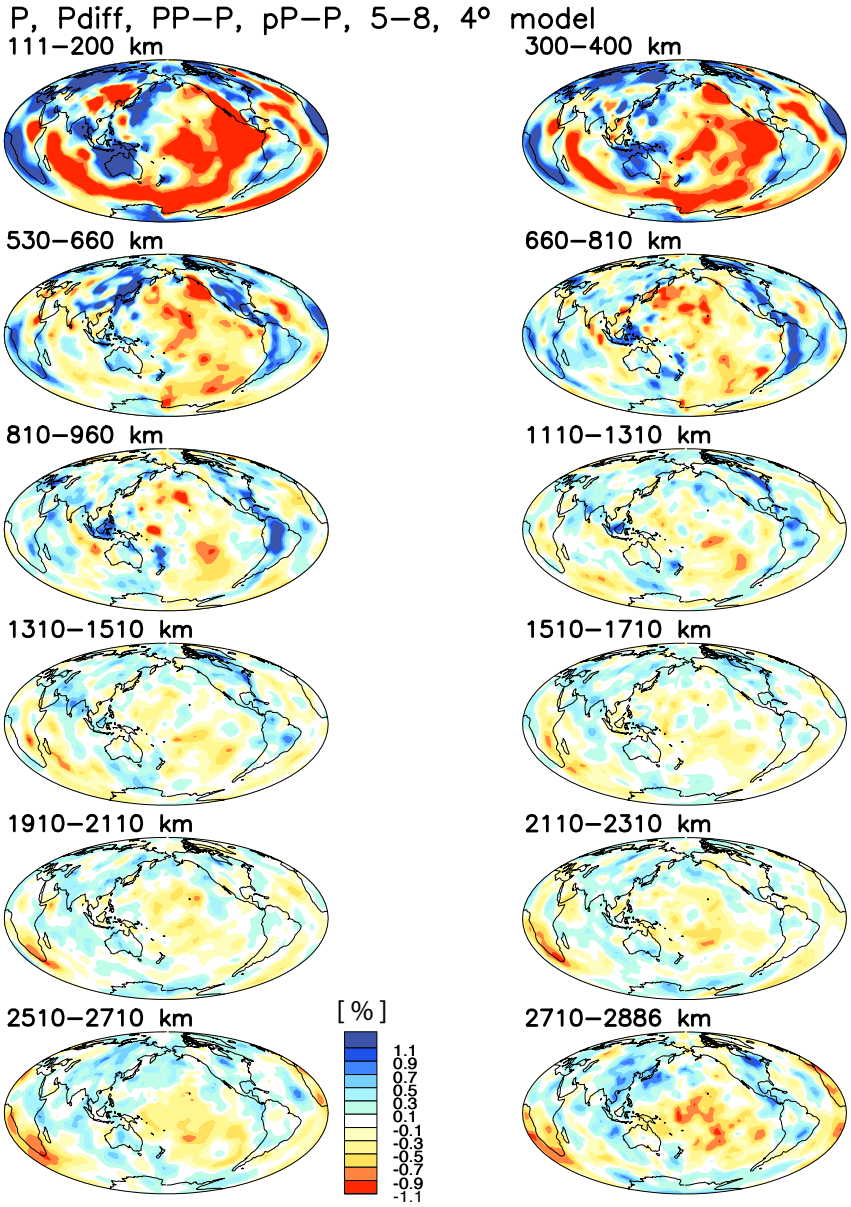


**Figure 2.7**: Slices of the mantle showing perturbation in compressional velocity in percent, made using projected data. Models are made using P, Pdiff, PP-P, and pP-P data sets.

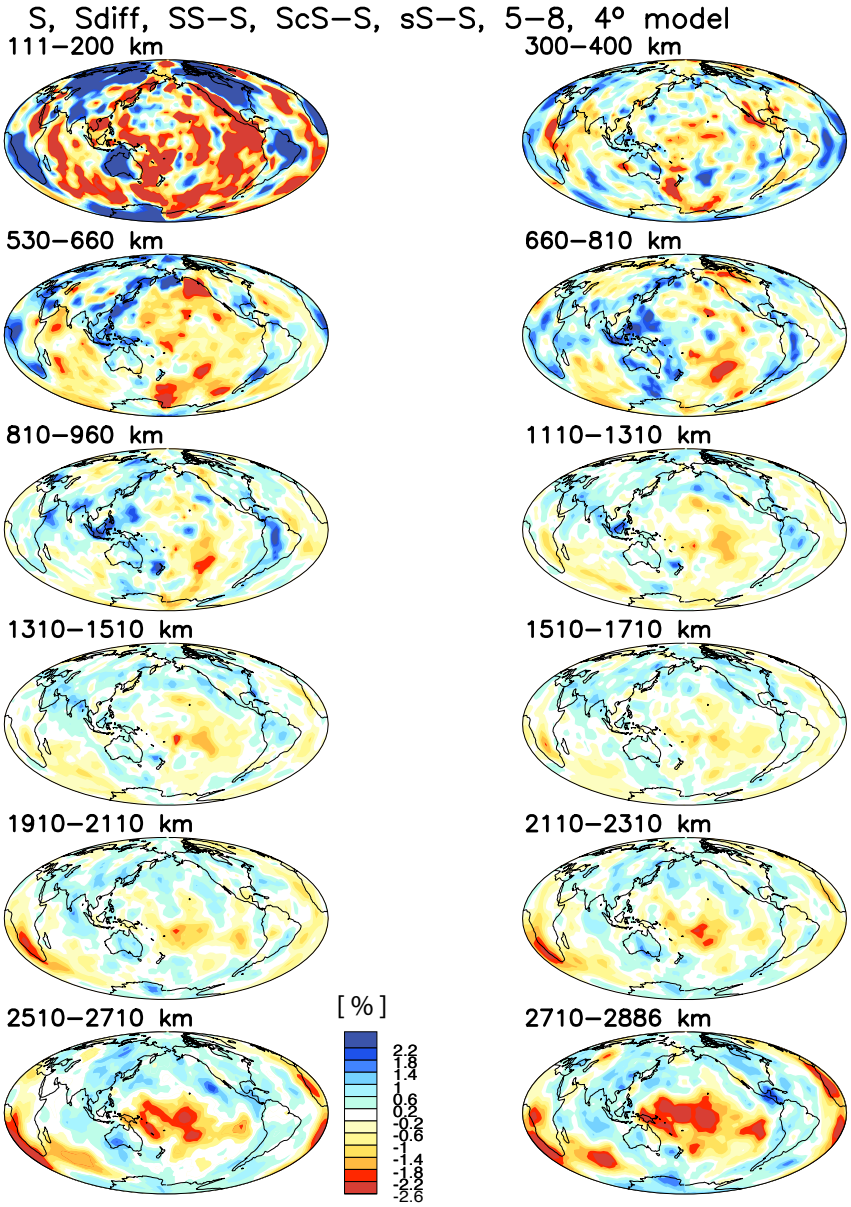


**Figure 2.8**: Slices of the mantle showing perturbation in shear velocity in percent, made using projected data. Models are made using the S, Sdiff, SS-S, ScS-S, and sS-S data sets, as well as surface waves.

projected S data on its own. The models are similar to existing models with large slow velocity anomalies underneath Africa and the Pacific and fast velocity anomalies where we expect to see subducting slabs.

### 2.5.2 Iterative Relocation

Although we demonstrated with the synthetic data that iterative relocation is not a safe approach to dealing with location error, we include an example of a P model made using the real data in order to illustrate how different the resulting model is (Figure 2.9). We note that due to the additional noise in the real data, we had to tighten the constraints on location, since the values that we used for the synthetic tests were not strong enough and allowed too many earthquakes to relocate above-ground. The resulting P model is quite different from the projected P model, particularly in the mid and upper mantle. The iteratively relocated model lacks slab-like features in the subduction zones, an observation that was also noted by Creager and Boyd (1992) in their study on the effects of mislocation on subduction zone velocity structure. Furthermore, the large slow velocity anomalies in the Pacific are smaller in size, particularly in the mid-mantle. Despite the differences between the projected and iteratively relocated models, the iteratively relocated models do fit the data well, with $\chi^2$ fits of 0.88, 0.89, 1.41, and 2.13 for the P, Pdiff, PP-P, and pP-P data sets, respectively. These fits are similar to those of the joint inversion (see Table 2.3). The S model, which is not shown, is more similar to the projected S model, illustrating again that signal from 3D structure in S data is larger than the location error and thus dominates the inversions.

### 2.5.3 Joint Inversion

The initial results of the joint inversion, using a weighting ($\lambda$) of one, were not as promising. Real data are inherently noisier than synthetic data, and as a result, the location of many events were poorly constrained. While we only had 45 above-ground earthquakes when testing the method on synthetic data, for the real data, we ended up with 1180 above-ground out of 6451 earthquakes. This is roughly 20% of the data set.

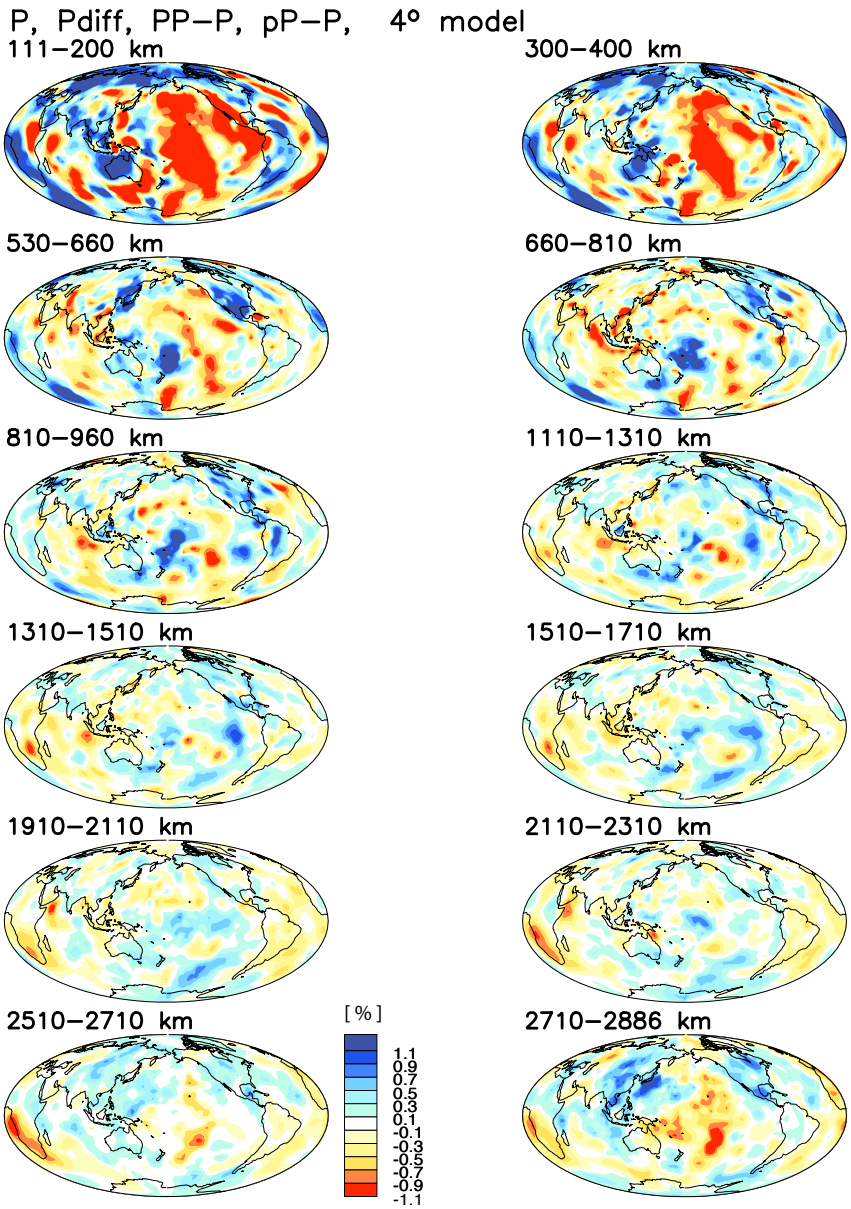


**Figure 2.9**: Slices of the mantle showing perturbation in compressional velocity in percent, made using iterative relocation. The model was made using the P, Pdiff, PP-P, and pP-P data sets.

As an initial fix, we tried setting all above-ground earthquakes to a default depth of 5km, but this resulted in a decreased fit of the models to the data. We experimented with changing the value of the weighting between the location and the velocity parts of the model, however, from tests on the synthetic data, we know that a $\lambda$ of one is the optimal weighting. Since there is a trade-off between origin time and depth, we tried subtracting the average residual per event out of the origin time and inverting the data. The remaining residual should then have been taken up by the depth. However, we still ended up with over 1000 airquakes. Lastly, we tried constraining the depth in the first iteration, similarly to Buland (1976), and then allowing the depth to move in the second iteration. Nevertheless, we still ended up with a large proportion of above-ground earthquakes. Furthermore, the shift in origin time, latitude, and longitude were also poorly constrained, moving as much as 50 s in time and 200 km in space. These factors all indicated that the inversion needed to be constrained.

To constrain the joint inversion, we added a constraint matrix for each event as we did in the iterative relocation (see equation 2.7). Initially, we constrained the events to move less than 4 s in time, 10 km in depth, and 15 km in latitude and longitude. These were the same constraints we initially tried when constraining the matrix while using iterative relocation. A constraint of 10 km in depth reduced the number of airquakes to approximately 500. Halving the depth constraint decreased the number of airquakes again to 250. A stronger depth constraint of 2.5 km, reduced the number of airquakes to 75, which was deemed acceptable. These events were excluded from the data set. To test the constraints, we added the same constraint matrix to our synthetic data set and found that constraints did not change the fit of the data significantly (see Table 2.2). Additionally, since none of the P data sets constrain the upper mantle very well, we also loosely constrain our P model to the S model down to a depth of 660 km, using a scaling value of 1.7, which is the expected value of $\frac{\delta v_s}{\delta v_p}$ in the upper mantle (Woodward and Masters, 1992). Tests on synthetic data indicate that the model constraint matrix does not change the fit of the model to the data. Likewise, the same is true for our real data.

The results of the constrained inversion can be found in Figures 2.10 and

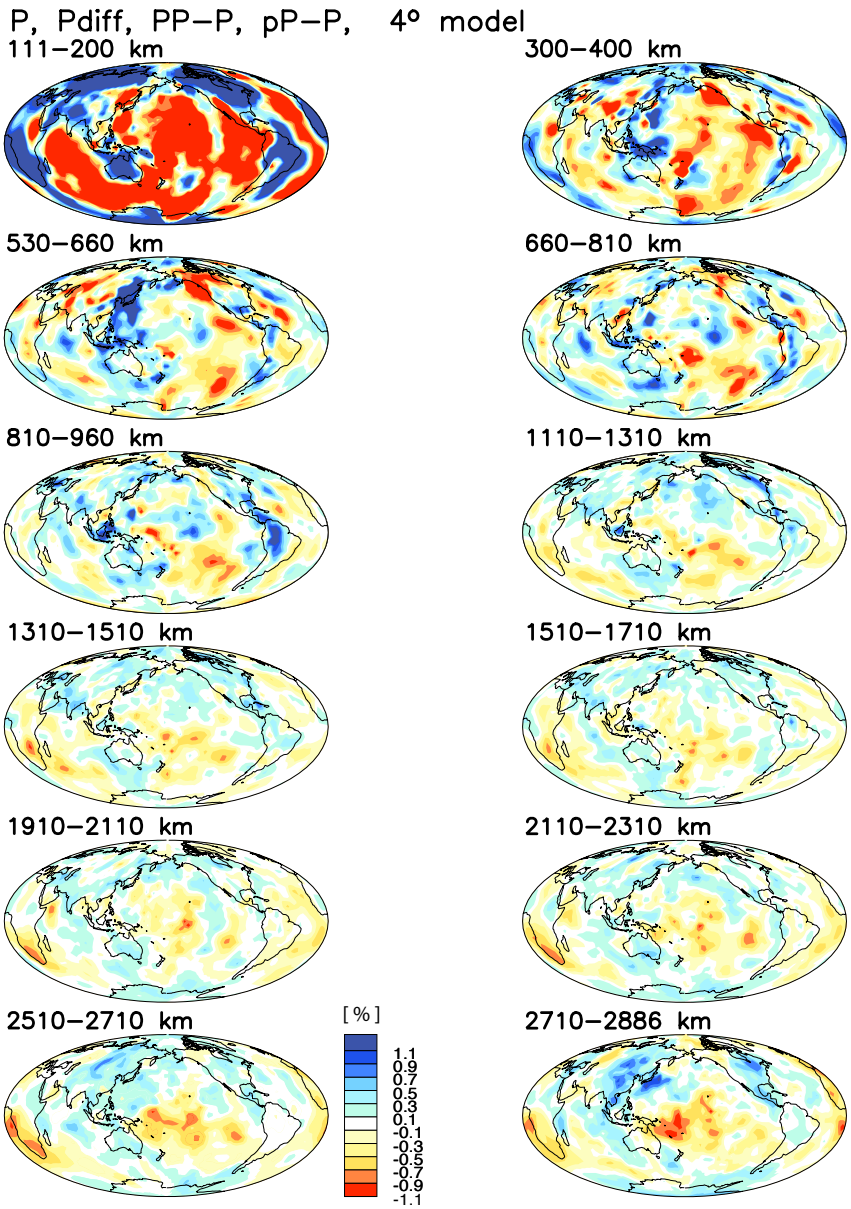


**Figure 2.10**: Slices of the mantle showing perturbation to compressional velocity in percent. This model was made by jointly inverting for structure and hypocenter. The upper mantle is loosely constrained to the S model during the inversion.

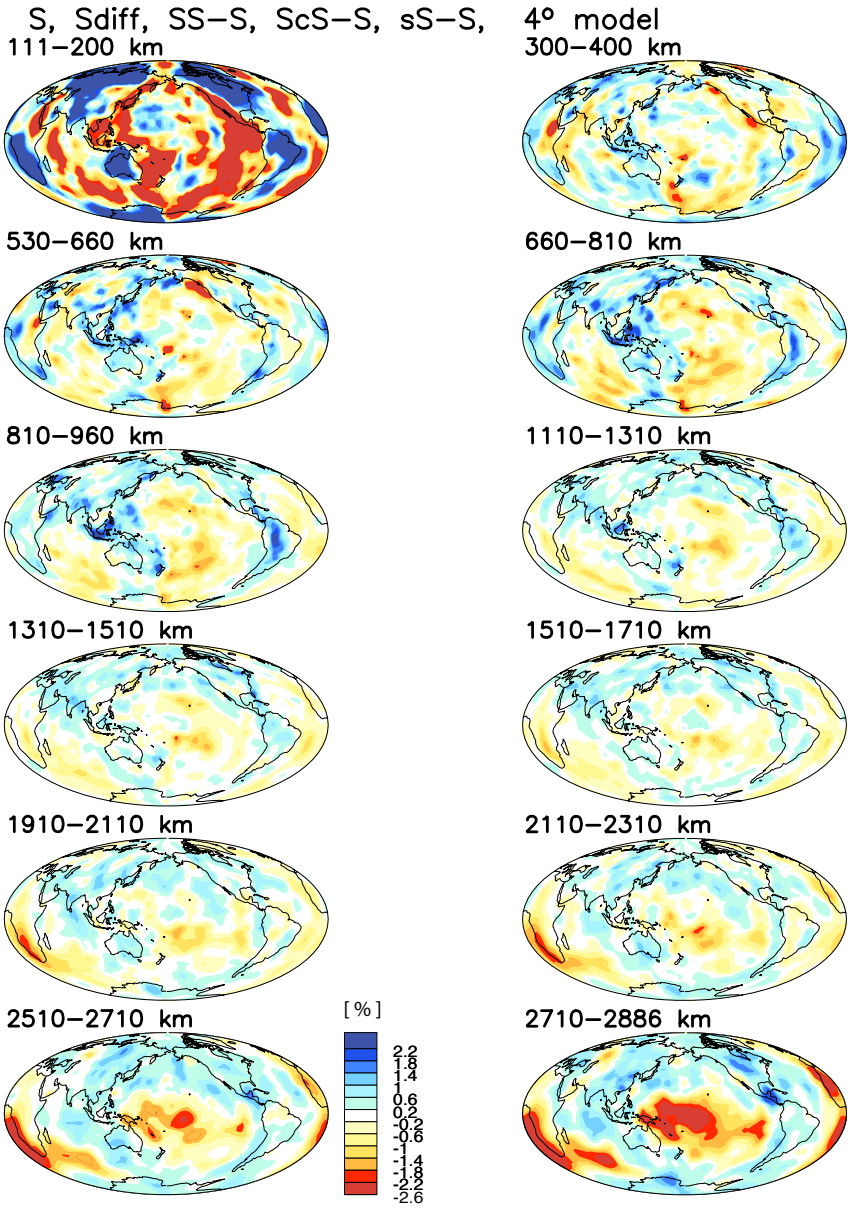


**Figure 2.11**: Slices of the mantle showing perturbation in shear velocity in percent. This model is the result of the joint inversion for structure and hypocenter and was made using our entire data set.

2.11. The fit of the models to the data can be seen in Table 2.3. We find that the model fits the data well, with the exception of the depth phase data sets, which is discussed in more detail later.

**Table 2.3**: $\chi^2$ fit of jointly inverted models to data sets

| Phase | $\chi^2$ | Phase | $\chi^2$ |
|---|---|---|---|
| P | 0.64 | S | 1.13 |
| Pdiff | 0.71 | Sdiff | 0.73 |
| PP-P | 1.26 | SS-S | 1.44 |
| pP-P | 2.40 | ScS-S | 1.34 |
| sP-P | 3.36 | sS-S | 2.22 |

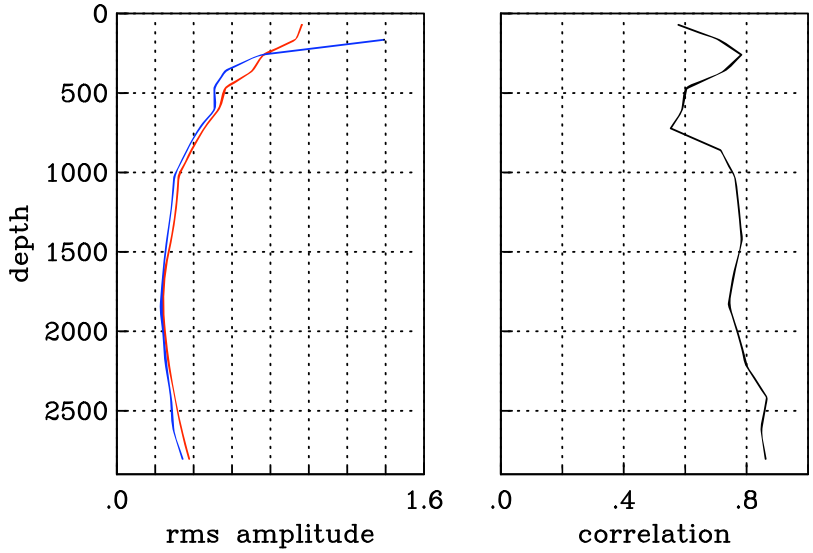


**Figure 2.12**: Amplitude and correlation of projected (red) and jointly relocated (blue) P models.

As a test of our inversion, we compare the models to models made with our projected data, since synthetic tests indicate that projection is indeed the safest approach to dealing with location error. The correlation plots can be seen in Figures 2.12 and 2.13. Whereas the synthetic projected and jointly inverted models had a correlation of almost 1 throughout the entire mantle, the correlations for the same models using the real data did not correlate as well. For the real data, the projected P model correlates well with the P model resulting from the joint inversion, with a correlation coefficient above

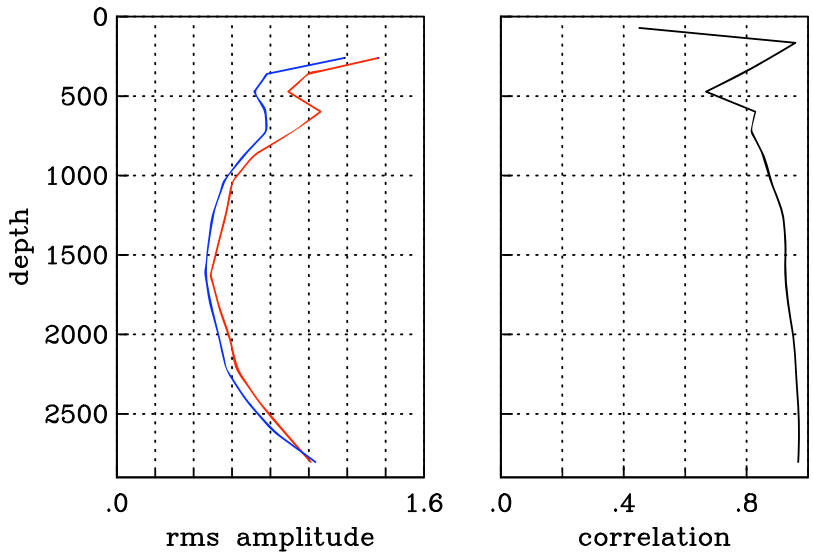


**Figure 2.13**: Amplitude and correlation of projected (red) and jointly relocated (blue) S models.

0.8 in most of the mantle. The models are most similar at the base of the mantle, again indicating that the diffracted data constrain structure well, and are least similar in the upper mantle, where resolution is the poorest. The reduced correlation, in comparison to the synthetic data, is probably the result of additional noise in the data, which make the locations harder to constrain. Additionally, in the joint inversion, the P model is constrained to the S model in the upper mantle, whereas it is not in the projected model, so we expect a decrease in correlation between the projected and jointly inverted P models in the upper mantle. The S projected and jointly inverted models correlate very well in the lower mantle, with correlation values approaching one at the base of the mantle. As with the P models, the upper mantle and in particular, the transition zone, do not correlate as well. Again, since the 3D signal from structure in S is larger, the better correlation with the projected model is unsurprising.

Comparing the models, we see the same large-scale features in both the projected and jointly inverted models. For the P models, the main differences are in the smaller scale structure of the low velocity zones in the Pacific, particularly at the base of the mantle. Structure in the upper mantle is also different, reflecting that the P model

was constrained to the S model in the joint inversion. The projected and jointly inverted S models are remarkably similar at the base of mantle, which is well sampled by ScS-S, which is largely insensitive to location error, since it is a differential phase. The joint inversion has smaller amplitude low velocity anomalies in the lower and mid-mantle, but otherwise, the shape of the structures is the same.

## 2.6 Depth Phases

As discussed earlier, the inclusion of depth phases in our inversion potentially provides a strong constraint on focal depth. It is illustrative to look at how changing the depths changes the pattern of depth phase residuals. Figure 2.14 shows binned residuals plotted at their surface bounce points for four different sets of event depths: the NEIC depths, the EHB depths, the depths from the joint inversion, as well as the best depths predicted by the depth phases. The best depth predicted by the depth phases is determined by summing the absolute values of all depth phase residuals for one event and looping over a range of depths until the depth that results in the smallest sum of residuals is found. These new depths can be as much as 50 km off from the original NEIC depths, demonstrating the need for relocation. Whereas the residuals for the NEIC depths produce a somewhat inconsistent pattern of fast and slow regions, the new depths produce a very systematic pattern of slow and fast areas in relation to the subduction zones, that are probably a reflection of slab and back-arc structure. We see this same pattern of fast and slow areas in other subduction zones around the world. Looking at the binned residuals for the EHB depths, we again see that the pattern of residuals is not quite as apparent, despite the inclusion of depth phases in their relocation procedure. The residuals for the depths from the joint inversion resemble the best depths predicted by the depth phases, reflecting their inclusion in the inversion. The poor fit of the models resulting from the joint inversion to the depth phase data is probably because the depth phases are sensitive to these rapid change in velocity, which occur on a smaller scale than the $4^o$ blocks that we use in our models.

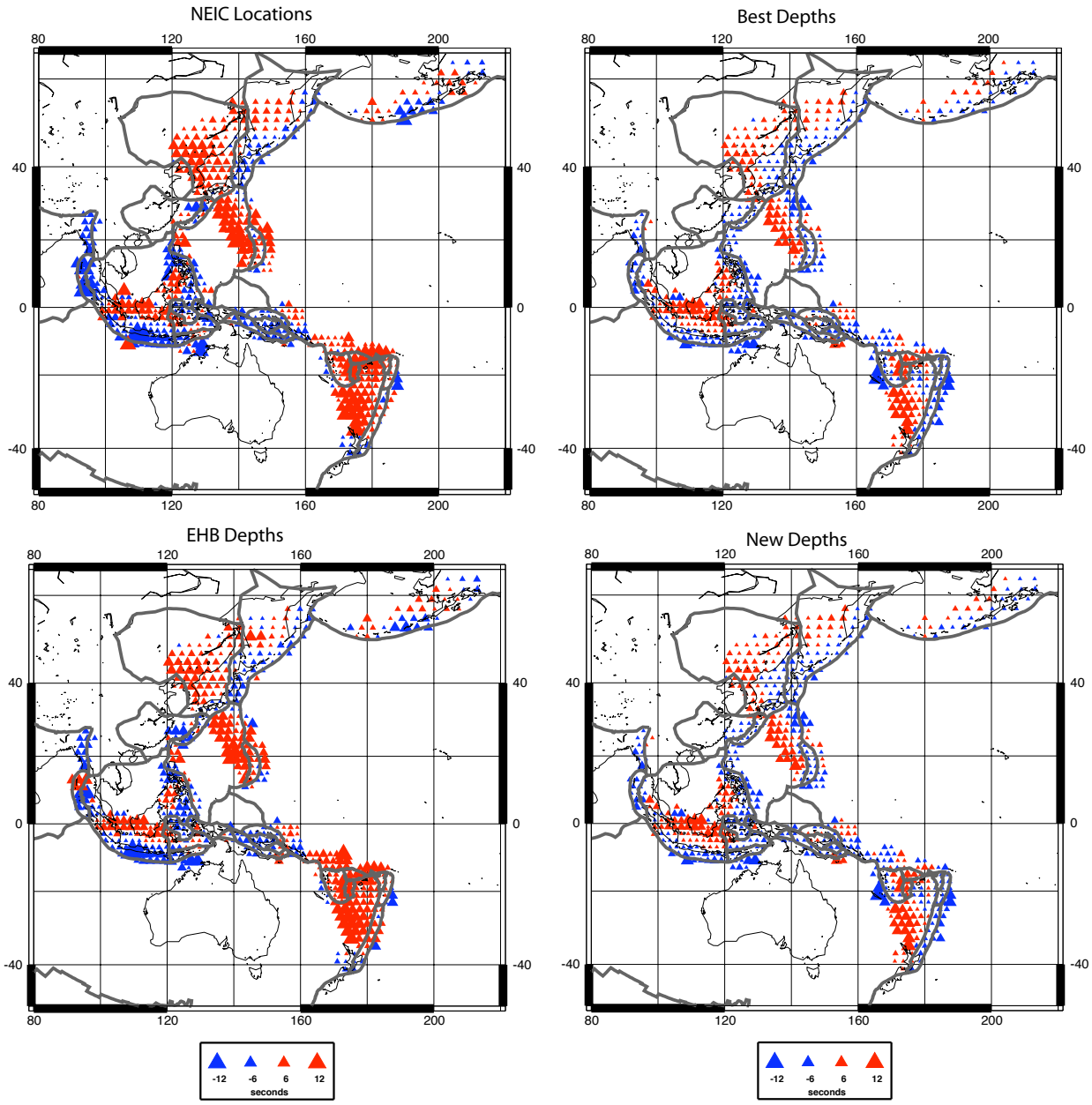


**Figure 2.14**: Binned sS-S residuals plotted at their sS surface bounce points for the NEIC locations (top left), best depths (top right), EHB locations (bottom left), and locations from the joint inversion (bottom right). The residuals are binned in $2^o$ caps.

## 2.7 Comparison with NEIC and EHB Locations

The average offset in origin time relative to the NEIC and EHB data sets is 3.7 s and 2.5 s, respectively. The smaller shift in time relative to the EHB data reflects the use of ak135 in the EHB locations, which is what we also use to pick our data. This delay in origin time in our newly relocated data is not unexpected. The NEIC and EHB locations are located using short-period data, whereas we use long-period data. There is also a clear relation between the shift in mean origin time and the moment of the event (see Figure 2.15), with offset increasing with moment. Included on the plot is the empirical $(moment)^{1/3}$ relationship which is expected for the source time (Kanamori and Anderson, 1975). We note that the average residual offset fits the predicted shift at low moments for the P data (red line), but diverges for larger events. This behavior is expected and observed on tests of synthetic data as well and results from the finite bandwidth of the long period data. The S data (blue line) show the same relationship but are offset from the P data. The offset between the S and P data may be due to imperfections in ak135 or due to the wrong choice of t* when picking (Oki et al., 2004).

The offset as a function of magnitude demonstrates the importance of relocation when mixing long-period and short-period data sets, lest the origin time offset be mapped into structure. The green and brown lines show the mean residuals per event for our new locations, which no longer show the moment dependence, since the offset has been corrected for in the relocation. Geographically, the largest shifts in origin time happen in subduction zones, which is unsurprising, since that is where the largest magnitude earthquakes generally occur.

One can also look at the relative shifts in location. The average shift in horizontal location is 16.1 km and 13.4 km relative to the NEIC and EHB locations, respectively. Systematic patterns of shifts can be seen when relocation vectors are plotted for those events which have a minimum of 200 measurements (Figure 2.16). In particular, we note a systematic shift away from the slab for events occurring in the Aleutians.

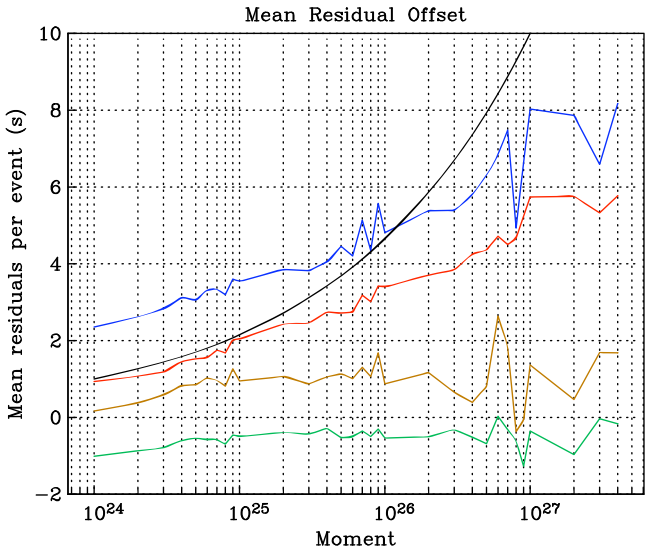


**Figure 2.15**: Mean residual offset (relative to ak135) per event as a function of moment. The red and the blue lines are for the S and P data, respectively, using the EHB locations. The green and brown lines are for the S and P data, respectively, using the new locations. The black line shows the empirical $moment^{1/3}$ relationship expected for source time processes.

Kennett and Engdahl (1991) show that that events in subduction zones are systematically shifted towards the overriding plate and have mislocation vectors of 20-40 km. In the Aleutians, in particular, Fujita et al. (1981) and Nieman et al. (1986) find, using a local array, that shallow-focus events are systematically mislocated north by 30 to 40 km. In light of these studies, the systematic shift of shallow events in the Aleutians back south in our study is sensible. Along the other subduction zones, the shifts are less systematic, although we do observe a large number of events in South America and the Kurils shifting away from the slab.

The average shift in depth relative to the EHB data set is -0.97 km and -2.1 km relative to the NEIC locations, meaning that on average, the new depths are a little shallower. The largest shifts in depths occur at subduction zones and are often controlled by depth phase measurements, which put a strong constraint on depth.

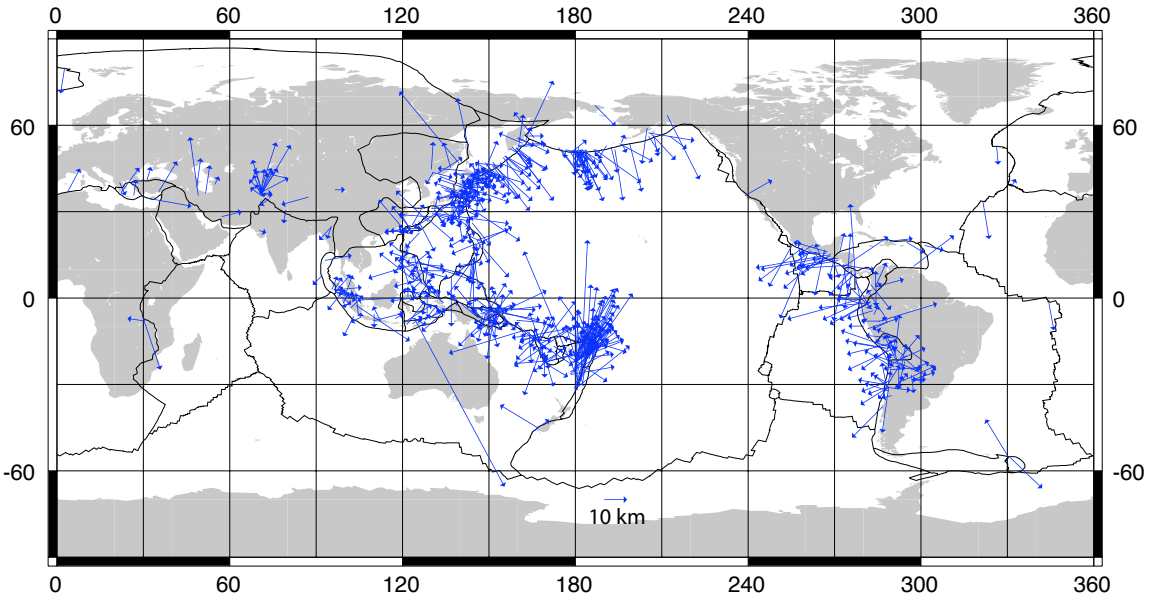


**Figure 2.16**: Relocation vectors relative to EHB locations for all events with 200 or more measurements. The head of the vector points towards the new locations.

## 2.8 Comparison With Test Events

Unlike with synthetic data, we cannot test the accuracy of our relocations, because we do not know the original locations of the earthquakes. However, a set of ISC test events exists, whose locations are thought to be known to 5 km or better and whose origin times are absolute (Bondar et al., 2004). We can use these events to test our relocation, by looking at the rms misfit to the known origin time and known location (see Table 2.4). While the list includes over 1000 test events, many of these are for nuclear explosions, for which we have no arrival times. Additionally, we are limited to using earthquakes for which we have at least 10 measurements, reducing the number of test events that we can use to 34. The test events also allow us to compare our relocations to global catalogues. As regards focal depth, the new locations do as well as the EHB locations in predicting depth, and both do better than the NEIC locations. While we do include depth phases in our inversion to improve depth constraint, we only have measurements for events with depths greater than 80 km. Since the test events are all shallower than 35 km, meaning that we have no depth phase measurements for these

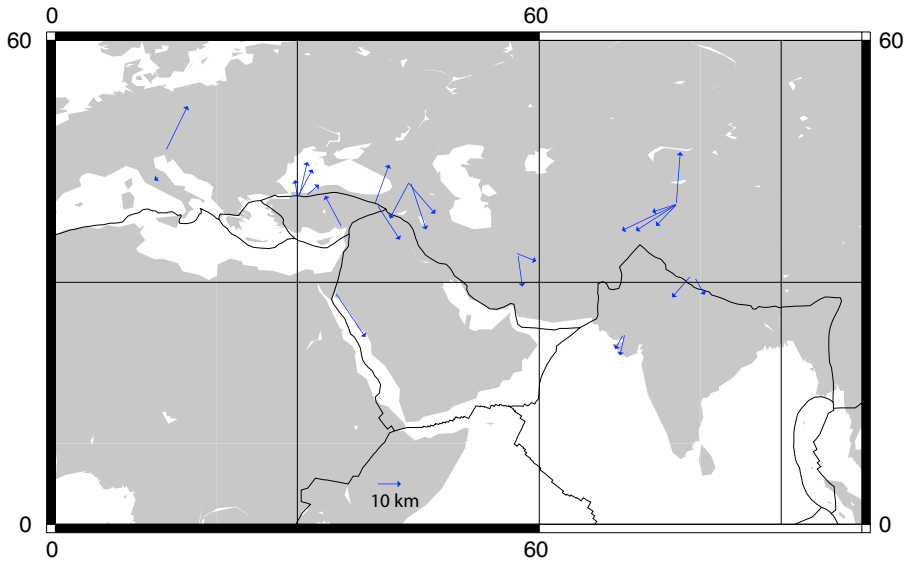


**Figure 2.17**: Mislocation vectors relative to ISC test event locations. The tail of the vector is at the true location.

events, we do not have as good a constraint on these depths and thus do not improve upon the EHB locations. Both the NEIC locations and EHB locations are better at predicting the offset in horizontal displacement and origin time. However, as noted earlier, there is a systematic offset in origin time relative to moment and the origin times of the test events were all determined using short period data. Thus, we expect the origin time to be shifted relative to magnitude. Correcting for this shift should improve the rms misfit in time. Nevertheless, with respect to the test events, we have not improved upon the locations of Engdahl et al. (1998). A plot of the mislocation vectors can be seen in Figure 2.17.

**Table 2.4**: Rms displacement from test events

| Locations | Origin Time (s) | Lateral Displacement (km) | Depth (km) |
|---|---|---|---|
| NEIC | 1.73 | 11.2 | 9.6 |
| EHB | 1.83 | 11.6 | 5.6 |
| New | 4.8 | 15.2 | 5.5 |

## 2.9 Conclusions

Earthquake mislocation is a large source of error in our tomographic inversions, particularly for our P data, where the effect of the mislocation is similar to the size of the signal from 3D structure. We tested three methods of dealing with location error: iterative relocation, projection, and a joint inversion for velocity and hypocenter. Based on tests of synthetic data, we found that projection and joint inversion were both able to correct for location error, with projection providing the best fit of the models to the data. Both resulting models correlated well with the original models used to make the synthetic data. Iterative relocation only worked for 1D synthetic data, but failed to return the correct answer for 3D synthetic data. The resulting models did not correlate well with models made using the original synthetic data sets, nor did the models fit the data well. The iteratively relocated velocity models also exhibited structures not seen in the original models, which could significantly change the interpretation of the results. This suggests that iterative relocation is not a good approach to use for teleseismic data sets.

We also examined the effects of different relocation methods on the correlation of shear velocity and bulk sound speed, by combining our synthetic shear and compressional models to make bulk sound speed models. Models made using iterative relocation gave distinctly lower correlations than models made using the other methods. However, the correlations for all of the models were significantly lower than the expected value of one. Only the joint inversion for shear velocity and bulk sound speed gave a correlation value of 0.9, indicating that combining separate S and P models to obtain a bulk speed model is not a safe approach.

Tests on real data yielded good results for both the projected and jointly inverted data sets. The resulting models correlate well with each other, particularly in the lower mantle. Projection is probably the ideal method, but due to the computational expense, a joint inversion for location and velocity is a reasonable substitute. However, care must be taken to properly constrain the inversion. The addition of depth phases im-

proves constraints on depth and results in a systematic pattern of residuals in subduction zones. We see systematic shifts of earthquakes away from the slab in subduction zones, particularly in the Aleutians.

## 2.10 Acknowledgements

Chapter 2 (Manners, U.J. and G. Masters (2008), A comparison of methods for global teleseismic earthquake relocation.) has been submitted in full for publication in the *Bulletin of the Seismological Society of America*. The dissertation author was the primary investigator and author of this paper.

# 3

# Analysis of core-mantle boundary structure using S and P diffracted waves

**Abstract**

Existing tomographic studies of the base of the mantle have been limited by poor coverage in the Southern Hemisphere. Using a new picking technique that allows us to process a large amount of data, we have created a new data set of diffracted P and S arrival times from long period seismograms. We used events from 1986 to 2005, obtaining approximately 35,000 Pdiff and 27,000 Sdiff measurements, with a distance range extending to 170 degrees. Coverage in the Southern Hemisphere is greatly improved by the addition of the diffracted data. Our new S model is similar to existing models of the base of the mantle, with improved definition of smaller scale structure of the large slow velocity anomalies beneath Africa and the Pacific. Our P model shows similar large-scale features to existing P models, however, smaller wavelength features are dissimilar. In general, models derived from our data show improved resolution at the base of the mantle. We also do a joint inversion for shear velocity and bulk sound speed. The addition of diffracted data to our model improves the resolution of bulk sound speed significantly. The models show the pattern of anti-correlation between shear velocity and bulk sound speed observed in earlier studies.

## 3.1 Introduction

While models of the large-scale seismic structure of the Earth's interior are in general agreement with each other, the structure of the core-mantle boundary remains poorly understood. The D" layer acts as a thermal, chemical, and mechanical boundary between the liquid iron core and the solid silicate mantle and is also the possible location of a phase boundary. Consequently, the large number of unusual features observed in the region is not surprising.

The D" layer is laterally heterogeneous, varying on both long and short wavelengths. The top of the D" layer is defined by a sharp increase in velocity, known as the D" discontinuity (e.g. Lay and Helmberger, 1983; Revenaugh and Jordan, 1991; Kendall and Shearer, 1994), which occurs between 150 to 450 km above the base of the mantle. While observations of the discontinuity indicate that it is a global feature, it remains unclear if it is continuous. Within the D", tomographic models show long wavelength velocity anomalies that are high in amplitude, particularly when compared to the rest of the mantle. Normal mode data indicates that these large slow regions may also be regions of higher density (Ishii and Tromp, 2001). The region is also characterized by large and rapid lateral variations in anisotropy (e.g. Vinnik et al., 1995; Kendall and Silver, 1996). Shorter wavelength structure includes ultra low velocity zones (ULVZs) and scatterers (Garnero, 2000).

One particularly intriguing observation at the base of the mantle is the anti-correlation between shear velocity and bulk sound speed (e.g. Su and Dziewonski, 1997; Masters et al., 2000; Antolik et al., 2003). Unlike compressional velocity, which is sensitive to both the shear and bulk modulus, bulk sound speed is sensitive only to the bulk modulus, as given by:

$$v_c{}^2 = \frac{\kappa}{\rho} = v_p{}^2 - \frac{4}{3} v_s{}^2 \tag{3.1}$$

Investigating the relative behaviour of shear velocity and bulk sound speed in the mantle allows one to determine the origin of a velocity anomaly. Ordinarily, we expect shear velocity and bulk sound speed to be positively correlated, which is indicative of a ther-

mal anomaly. However, if shear velocity and bulk sound speed are negatively correlated, the anomaly cannot be explained by thermal effects alone, implying chemical or phase heterogeneity. The anti-correlation observed at the base of the mantle suggests that the velocity anomalies observed may be chemical in origin. Current tomographic models of the base of the mantle, however, are limited by poor resolution, meaning that we do not have a good understanding of the spatial extent of the anti-correlation. This lack of resolution prevents us from fully understanding the processes occurring at the CMB.

Compressional models of the Earth have traditionally been made using short period data, taking advantage of the huge data set of P arrival times available from the ISC (International Seismological Centre) (e.g. Bijwaard et al., 1998; Kennett et al., 1998; Vasco and Johnson, 1998; Boschi and Dziewonski, 2000; Karason and van der Hilst, 2001; Li et al., 2006). While ISC data are typically noisy, due to the large variety of instruments used as well as the large number of operators making the measurments, the size of the data set, which numbers in the millions, compensates for the variable quality of individual picks. However, despite the size of the data set, coverage at the base of the mantle is poor, particularly in the Southern Hemisphere, due to the uneven distribution of stations and earthquakes.

Models made using ISC S arrival times, on the other hand, are less common. ISC S data are typically very noisy, since the arrivals are measured on vertical component instruments, which have a dominant period of 1s, whereas S arrivals have a dominant period of 4s. Furthermore, S picks past $80^o$ are often misidentified with SKS phases, meaning that resolution of the deep mantle in models made using ISC data is typically poor. Nevertheless, S models made using ISC S arrivals do exist (e.g. Robertson and Woodhouse, 1995, 1996; Vasco and Johnson, 1998; Kennett et al., 1998). Since we ultimately wish to compare shear velocity and bulk sound speed anomalies, the absence of reliable S models of the base of the mantle implies that we need to use other data sets.

An alternate approach is to use long-period data. While long-period data are not as sensitive to smaller scale structure, they are generally of better quality. Addi-

tionally, the inclusion of good quality secondary phases means that resolution can be improved. Studies using long-period data include waveform modeling (e.g. Su and Dziewonski, 1997; Megnin and Romanowicz, 2000; Antolik et al., 2003; Panning and Romanowicz, 2006), as well as models made using absolute and differential arrival times (e.g. Grand, 1997; Ritsema et al., 1999; Masters et al., 2000; Simmons et al., 2006; Houser et al., 2008). Recently, there has been a move to apply finite-frequency kernels to long-period data sets (Montelli et al., 2006). The results of finite-frequency modeling show that the amplitudes of deep, small-scale velocity heterogeneities are underestimated by ray theory. However, these models still lack resolution at the base of the mantle.

A number of studies have used core-reflected and diffracted phases, which are more sensitive to CMB structure, to improve resolution of the deep mantle. Shear velocity models are generally better resolved at the base of the mantle than P models, due to the inclusion of long-period ScS-S (e.g. Masters et al., 2000; Grand, 1997; Montelli et al., 2006; Houser et al., 2008), as well as absolute ScS, SKS, and SKKS (e.g. Grand, 1997; Ritsema et al., 1999; Simmons et al., 2006) travel times. Ritsema et al. (1999) also include some Sdiff measurements, however, the data set is quite small. Despite the different techniques and data sets used, the features seen in the various models at the base of mantle, such as the large slow regions underneath the Pacific and Africa, are generally similar (Figure 3.1). While these shear velocity models correlate well at the base of the mantle (Figure 3.2), differences in the finer scale structure and amplitudes of the large slow velocity anomalies remain, indicating that the structure at the base of the mantle can be better constrained.

Improving coverage of the CMB in P models is more difficult. Whereas inversions for shear velocity can incorporate ScS travel times to improve sampling, long period PcP arrivals are difficult to pick, due to the low impedance contrast at the CMB. At shorter periods, several studies have included ISC PKP (e.g. Su and Dziewonski, 1997; Vasco and Johnson, 1998; Boschi and Dziewonski, 2000; Antolik et al., 2003) and PcP (e.g. Vasco and Johnson, 1998; Boschi and Dziewonski, 2000) travel times.

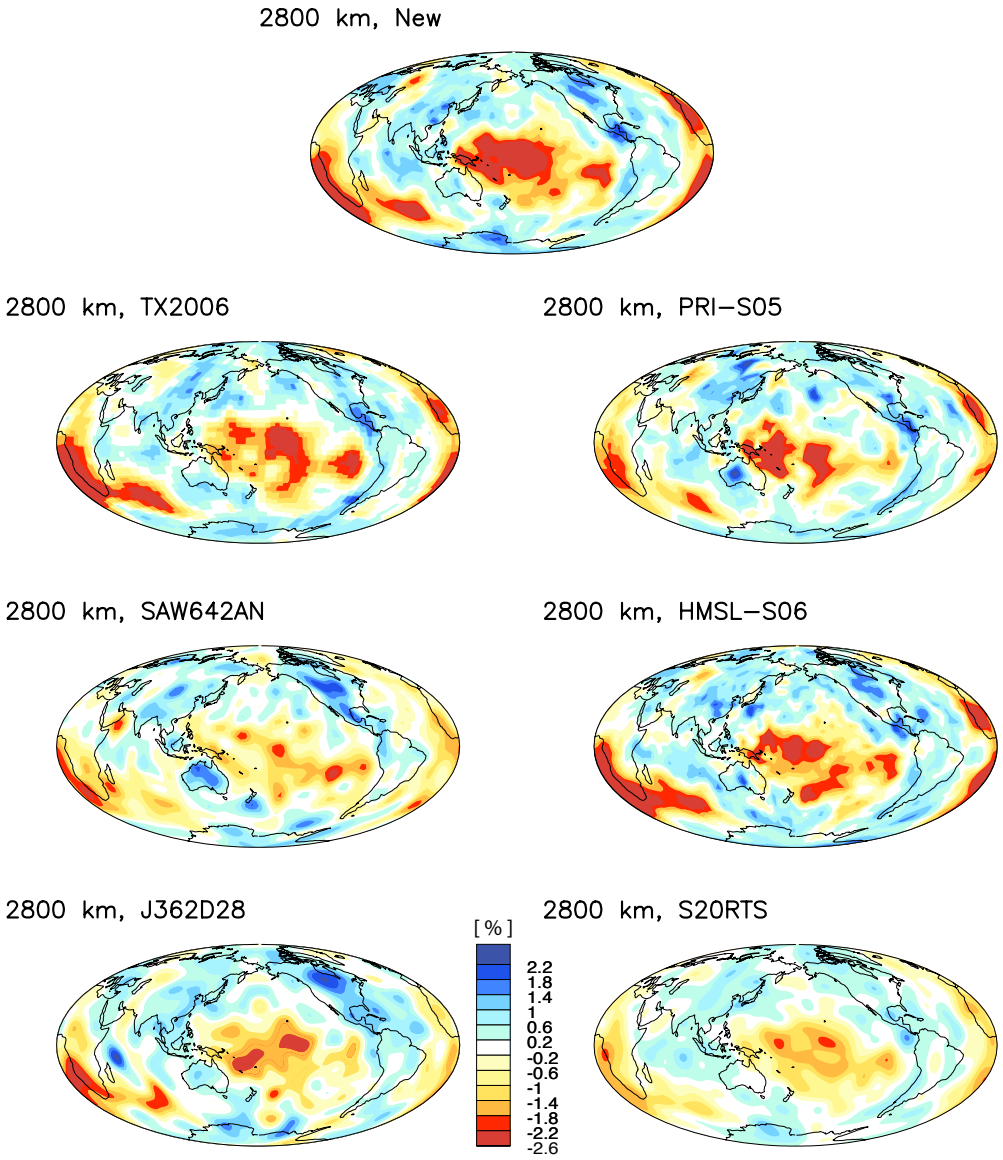


**Figure 3.1**: Slices of the base of the mantle showing perturbation in shear velocity for seven different models. The models are J362D28 (Antolik et al., 2003), HMSL-S06 (Houser et al., 2008), SAW642AN (Panning and Romanowicz, 2006), PRI-S05 (Montelli et al., 2006), S20RTS (Ritsema et al., 1999), TX2006 (Simmons et al., 2006), as well as our new model.

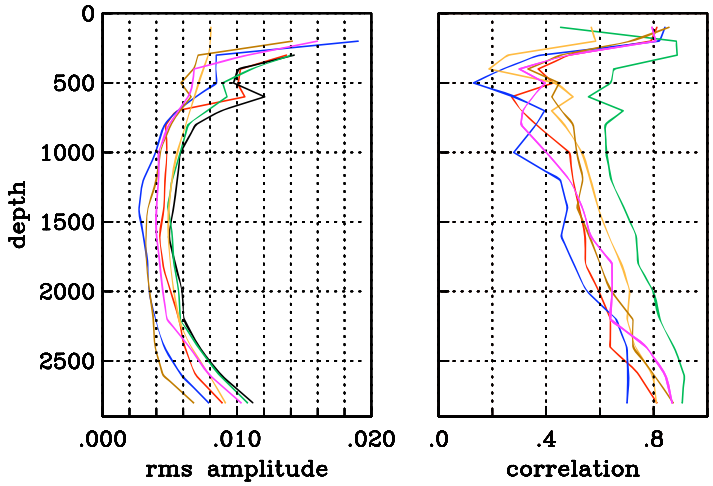


**Figure 3.2**: Amplitude (left) and correlation (right) plots for existing shear velocity models with our new model. The models are: New (black), J362D28 (red), HMSL-S06 (green), SAW642AN (blue), PRI-S05 (yellow), S20RTS (brown), TX2006 (pink).

However, the high noise level of later arriving phases in the ISC data sets makes their use more problematic. To circumvent this problem, Karason and van der Hilst (2001) incorporated hand-picked data sets of PKP and PKP-Pdiff travel times measured by McSweeney (1995) and Wysession (1996), respectively. While their inclusion into the inversion did improve CMB coverage, both of the data sets were small. Figure 3.3 shows the lowermost layer for four current P models, as well as a new model, which will be discussed later. The varying shape and size of the large slow velocity anomalies beneath the Pacific and Africa demonstrate how different current models of the CMB are, even at long wavelengths. The lack of correlation between existing P models illustrates that structure at the base of the mantle is still poorly constrained (see Figure 3.4). To fully understand processes at the base of the mantle, both our S and P models models need to be well resolved and this is best achieved by improving coverage.

We improve the coverage of the CMB by using diffracted phases. Diffracted waves are well suited to a study of the base of the mantle, because they spend a significant portion of their ray path along the CMB. Additionally, they sample regions

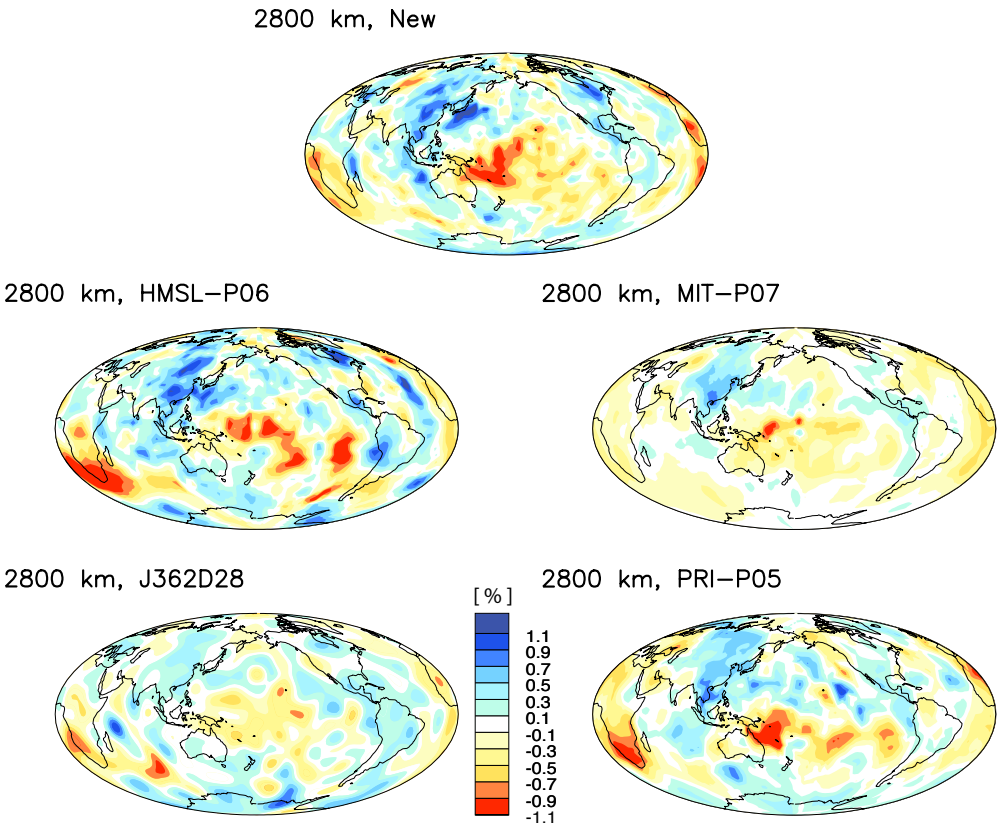


**Figure 3.3**: Slices of the base of the mantle showing the perturbation in P velocity for several different models at the base of the mantle. The models are J362D28 (Antolik et al., 2003), HMSL-P06 (Houser et al., 2008), MIT-P07 (Li et al., 2006), as well as a new model made using our diffracted data.

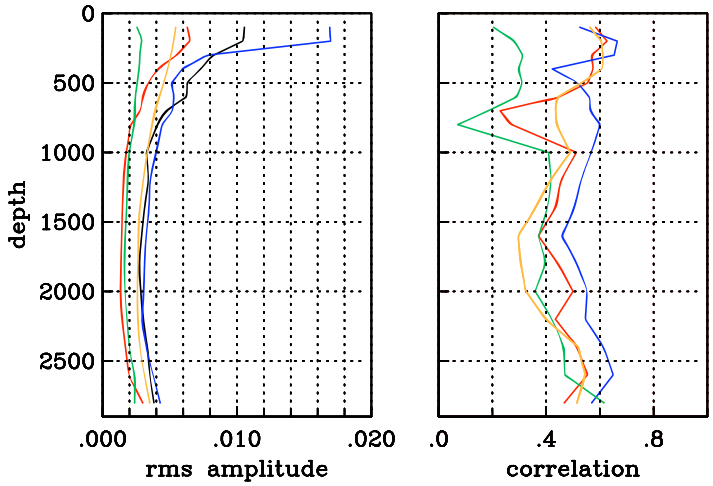


**Figure 3.4**: Amplitude (left) and correlation (right) plots for existing models with our new model. The models are: new (black), J362D28 (red), HMSL-P06 (blue), MIT-P07 (green), PRI-P05 (yellow).

otherwise inaccessible to other phases. However, due to their emergent nature, the arrival times of diffracted waves are difficult to pick using traditional techniques. Using a new picking technique known as cluster analysis, we are able to skirt this problem by measuring relative arrival times. Cluster analysis has the additional benefit of allowing us to process a large amount of data in a short amount of time. The resulting diffracted data sets are inverted with existing data sets to model the base of the mantle. We also do a joint inversion for shear velocity and bulk sound speed to investigate anti-correlation at the base of the mantle.

## 3.2 Method

### 3.2.1 Data

#### Cluster Analysis

To construct our diffracted data set, we use long-period data obtained from all the networks and PASCAL experiments that submit LH data to the IRIS DMC (Incorporated Research Institution for Seismology Data Management Center). The data

are restricted to earthquakes with a magnitude greater than 5.5 and to events occurring between 1986 and 2005. Before being picked, the waveforms are filtered to the SRO station response, which ensures that they have the same frequency content, giving them a dominant period of 20s. To improve coverage beneath South Africa, we include BH data from the SASE experiment, which are resampled to one sample per second and also filtered to the SRO station response.

Increasingly large data sets make picking individual traces infeasible. However, automated techniques, which employ more stringent quality checks, are poorly suited for diffracted data since they are emergent. In order to improve coverage of the CMB, we have created a data set of diffracted P and S wave travel times using cluster analysis (Houser et al., 2008). Cluster analysis is a combination of manual and automated picking techniques that takes advantage of the similarity of long-period waveforms over a long range of distances. This similarity is used to measure the relative arrival times at multiple stations. For each event, the traces for all stations are compared to each other using cross-correlation and then grouped according to their degree of similarity (Figure 3.5). The traces within each group are then cross-correlated a second time to obtain relative arrival times. All the traces within the cluster are stacked to create an average trace, which is then picked relative to a synthetic to obtain an absolute travel time. The relative arrival times are then used to calculate the absolute travel times for the entire cluster. To identify mistakenly picked phases, we check the polarity of the data against the polarities predicted by the Harvard CMT catalogue. Polarity mismatches that have a travel time residual greater than 4 seconds are removed. Using this technique, we are able to process a large amount of data in a short amount of time while retaining quality control. The resulting data set consists of approximately 35,000 Pdiff and 27,000 Sdiff traces extending to a range of $170^o$.

**Correction for Diffraction Effects**

Prior to measuring the arrival times of the data, we have to correct for waveform distortion due to diffraction effects. Due to interactions with the core, the diffracted

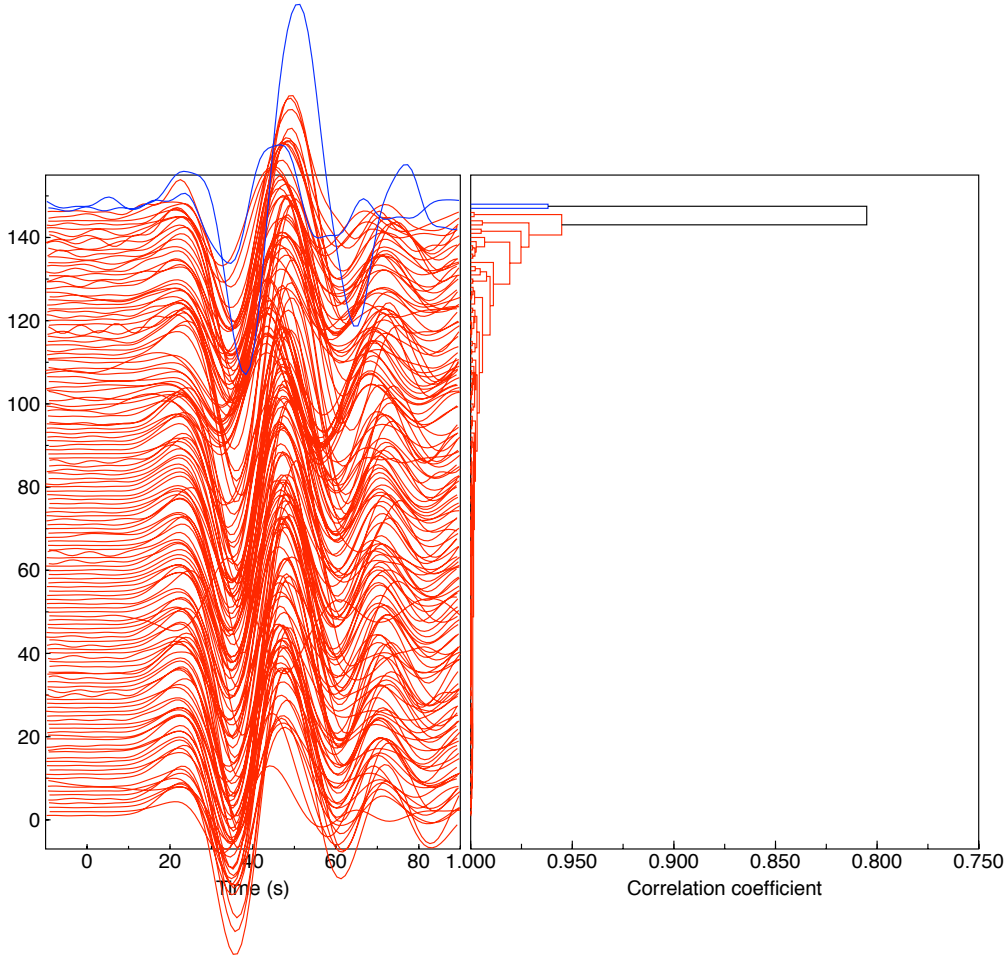


**Figure 3.5**: All Pdiff waveforms for an event on 2001:1:6:57:4.2. The waveforms are grouped according to similarity, giving just one group in this example (red). The waveforms are cross-correlated to give the relative arrival times within the cluster.

data are effectively low-pass filtered as they pass along the CMB (Scholte, 1956; Duwalo and Jacobs, 1959). The removal of high frequencies results in a phase shift and amplitude decay, dependent on the frequency, $\omega$, the ray parameter, p, and the distance from the core shadow edge, $\delta\theta$. This amplitude decay of waves in the shadow zone has been used to study the velocity structure of the D". The value of the decay constant, $\gamma(\omega)$, which is a measure of amplitude decay as a function of frequency, has been determined using long-period diffracted data (e.g. Alexander and Phinney, 1966; Phinney and Alexander, 1969) as well as numerically (e.g. Alexander and Phinney, 1966; Phinney and Alexander, 1966; Phinney and Cathles, 1969; Chapman and Phin-

ney, 1970, 1972). Since amplitude decay is largely dependent on the velocity gradient across the D", it has also been used to constrain radial velocity structure (e.g. Doornbos and Mondt, 1979; Mula, 1981; Valenzuela et al., 2000).

We are, however, more interested in the effect of phase shift, which is particularly important, because it changes the apparent slowness. Scholte's work shows that seismograms at a distance $\theta$ and $\theta + \delta\theta$ are related by:

$$\frac{u(\theta + \delta\theta)}{u(\theta)} = \sqrt{\frac{sin(\theta + \delta\theta)}{sin\theta}} e^{i\lambda\delta\theta} e^{-\gamma\delta\theta} \tag{3.2}$$

where

$$\lambda = c(\omega p)^{\frac{1}{3}} \tag{3.3}$$

and

$$\gamma = \sqrt{3}\lambda \tag{3.4}$$

The value of c, which is a constant and depends on structure near the CMB, was empirically determined from tests using synthetic data and was found to be 0.5 for the Pdiff data and 0.45 for the Sdiff data. A failure to correct for diffraction effects can result in systematic shifts of arrival times, which are then mapped into velocity structure. Filtering the waveforms also has the added benefit of increasing the similarity of waveforms, making picking easier, since waveforms can be grouped into fewer clusters.

Before picking, the data are corrected for diffraction effects to a reference distance of $105^o$ (Figure 3.6). The reference distance was chosen to maximise amplitudes, which are larger at shorter distances. After the waveforms are cross-correlated and grouped into clusters according to their similarity, a reference trace for each cluster is chosen by finding the trace with the highest signal-to-noise ratio, that is closest to $105^o$. The waveforms in each cluster are then refiltered to the distance of the new reference trace and stacked to construct the average trace, which is used to pick the absolute times and determine absolute times for the entire cluster.

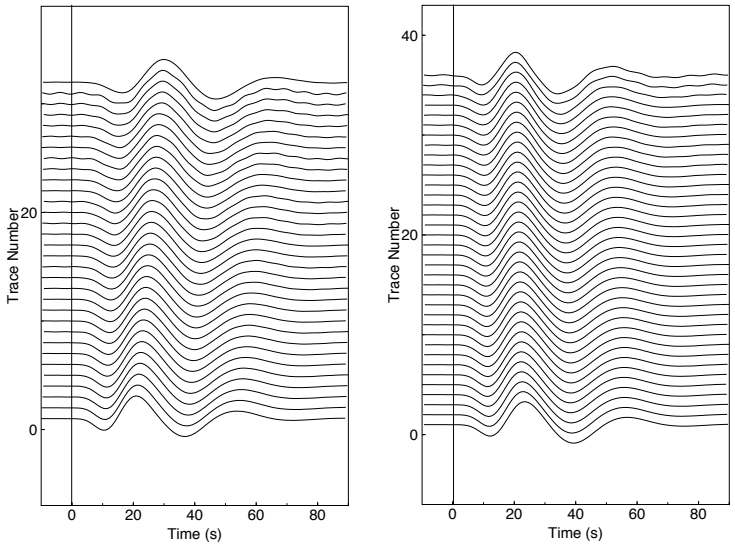


**Figure 3.6**: An example of unfiltered (left) and filtered (right) synthetic Sdiff waveforms. The waveforms are plotted in order of distance, with the shortest distance ($98^o$) at the bottom and the largest distance ($160^o$) at the top. The unfiltered waveforms show a clear shift to the right at longer distances which is corrected by filtering.

### Errors

Before inverting the data, we need to determine the errors in the data set. The overall data variance, $\sigma_T$, is dependent on 3D structure, $\sigma_{3D}$, mislocation error, $\sigma_x$, and remaining picking error, $\sigma_N$, as given by:

$$\sigma_T{}^2 = \sigma_{3D}{}^2 + \sigma_x{}^2 + \sigma_N{}^2 \tag{3.5}$$

Our picks are assigned a grade of A, B, or C, based on the quality of the measurement. Since $\sigma_N$ is dependent on pick quality, this gives us a total of three equations to solve. To estimate the signal from 3D structure, we invert the Sdiff data using surface waves to constrain the upper mantle. The resulting model prediction is then subtracted from the travel time residuals and any outliers are removed. We then calculate the scaled median absolute deviation (SMAD) of the travel time residuals both with and without the correction for 3D structure for our A, B, and C quality picks. Using a mislocation error of 1.2 seconds, we can then solve for $\sigma_N$ for the three different pick qualities, using non-negative least squares (see (Bolton and Masters, 2001) for more details). We find

that the contribution from 3D structure is 3.8 seconds, giving us errors for our A, B, and C picks of 1.8, 2.3, and 3.4 seconds, respectively. The Pdiff errors are determined similarly, giving us errors of 0.8, 1.1, and 1.7 for our A, B, and C picks, respectively.

**Additional Data Sets**

To constrain mid and upper mantle velocity structure, we combined our diffracted data sets with pre-existing data sets of absolute and differential body wave travel times, for events occurring between 1976 and 2005. These data sets include P, PP-P, pP-P, sP-P, sS-S, S, SS-S, and ScS-S measured (see Tabel 3.1, picked manually or using cluster analysis (Houser et al., 2008). We also include surface wave data (Masters et al., 2000, *Laske*, personal communication). The effects of crustal thickness variations are removed using CRUST 2.0 (Bassin et al., 2000) and the data are corrected for the Earth's ellipticity (Kennett and Gudmundsson, 1996). Data are weighted by their errors during inversion, so that better quality measurements receive more weight.

**Table 3.1**: Phases and number of measurements included in study

| Phase | Number of Picks | Years |
|---|---|---|
| P | 182724 | 1976 - 2005 |
| Pdiff | 34774 | 1986 - 2005 |
| PP-P | 26116 | 1976 - 1999 |
| S | 169832 | 1976 - 2005 |
| Sdiff | 26706 | 1986 - 2005 |
| SS-S | 32266 | 1976 - 1999 |
| ScS-S | 26840 | 1976 - 2005 |
| pP-P | 23184 | 1976 - 2005 |
| sP-P | 26615 | 1976 - 2005 |
| sS-S | 30223 | 1976 - 2005 |

### 3.2.2 Inversion

Earthquake mislocation is a large source of error in our data sets, particularly for our P data, where the effect of the mislocation is similar in size to the signal from 3D structure (Bolton and Masters, 2001). We find that the best method of dealing

with mislocation error is by inverting simultaneously for location and velocity structure, (Manners and Masters, 2008a), such that:

$$\delta \mathbf{t} = \begin{bmatrix} \gamma \mathbf{A} & \mathbf{B} \end{bmatrix} \begin{bmatrix} \gamma^{-1} \delta \mathbf{h} \\ \delta \mathbf{v} \end{bmatrix} \tag{3.6}$$

where $\mathbf{A}$ is a matrix containing the travel time derivatives with respect to location, $\delta \mathbf{h}$ is a vector representing the perturbation in location and origin time, $\mathbf{B}$ is the matrix of velocity derivatives, and $\delta \mathbf{v}$ is a vector representing the 3D perturbations in velocity. Ray paths are calculated relative to ak135 (Kennett et al., 1995). Changing the value of $\gamma$ allows us to control how much we want to weight the relocation versus the velocity part of the inversion. A large value of $\gamma$ forces most of the signal to go into the relocation, whereas a small value weights the inversion towards the velocity model.

We did an initial joint inversion, using all of our data sets, for velocity structure and location. The locations determined from this initial inversion are then used in subsequent inversions (Manners and Masters, 2008a). S models are made using the S, Sdiff, SS-S, ScS-S, and sS-S data sets, as well as surface wave dispersion measurements for Rayleigh waves. P models are made using the P, Pdiff, PP-P, and pP-P data sets. Since our P data do not resolve the upper mantle well, we loosely constrain the P model to the S model down to a depth of 660 km, using a scaling value of $\frac{\delta v_p}{v_p} = \frac{1}{1.7} \frac{\delta v_s}{v_s}$, which is the expected relationship between S and P in the upper mantle (Woodward and Masters, 1992). The models are parameterised by 18 layers, which are 100 km thick in the upper mantle and 200 km thick in the lower mantle. Each layer is divided into 4° equal area blocks, giving a total of 46,404 blocks.

We use first-difference smoothing radially and laterally, choosing our smoothing parameters by weighing the roughness of the model, $\mathbf{R}$, against the $\chi^2$ fit of the model to the data. We seek to minimize:

$$(\mathbf{Am} - \mathbf{d})^2 + \lambda^2 (\mathbf{Sm})^2 \tag{3.7}$$

which leads to the set of equations:

$$\begin{bmatrix} \mathbf{A} \\ \lambda\mathbf{S} \end{bmatrix} \begin{bmatrix} \mathbf{m} \\ 0 \end{bmatrix} = \begin{bmatrix} \mathbf{d} \\ 0 \end{bmatrix} \tag{3.8}$$

that is solved using LSQR (Paige and Saunders, 1973). The model roughness,$\mathbf{R}$, is thus given by:

$$\mathbf{R} = \mathbf{m^T} \cdot \mathbf{S^T} \cdot \mathbf{S} \cdot \mathbf{m} \tag{3.9}$$

where $\mathbf{S}$ is the roughness matrix and $\mathbf{m}$ is the model. We find that changing the radial smoothing does not change the fit of the models to the data significantly. We thus choose as low a value of radial smoothing as possible. The models are somewhat more sensitive to lateral smoothing, nevertheless, fit to the body wave data is not significantly improved by decreasing smoothing. Surface wave measurements are more sensitive to smoothing, so we use their fit to guide us in choosing the strength of lateral smoothing.

### 3.2.3 Joint Inversion for Shear Velocity and Bulk Sound Speed

In addition to separate inversions for S and P velocity, we jointly invert for shear velocity and bulk sound speed, solving the following system of equations:

$$\begin{bmatrix} \delta t_p \\ \delta t_s \end{bmatrix} = \begin{bmatrix} x\mathbf{B_p} & (1-x)\mathbf{B_p} \\ \mathbf{B_s} & 0 \end{bmatrix} \begin{bmatrix} \delta\mathbf{v_s} \\ \delta\mathbf{v_c} \end{bmatrix} \tag{3.10}$$

where $x = \frac{4}{3}(\frac{{v_s}^2}{{v_p}^2}) = 0.4$. We solve for relative perturbation in velocity, such that $\delta\mathbf{v_s} = \frac{\delta v_s}{v_s}$ and $\delta\mathbf{v_c} = \frac{\delta v_c}{v_c}$. The perturbation in P velocity, $\delta v_p$, is given by:

$$\frac{\delta v_p}{v_p} = (1-x)\frac{\delta v_c}{v_c} + x\frac{\delta v_s}{v_s} \tag{3.11}$$

Since bulk sound speed amplitudes are not well constrained in the joint inversion, we loosely constrain bulk sound speed to shear velocity throughout the entire mantle, using a scaling value of $\frac{\delta v_c}{v_c} = 0.3\frac{\delta v_s}{v_s}$, which is determing using the relationship: $\frac{\delta v_p}{v_p} = \frac{1}{1.7}\frac{\delta v_s}{v_s}$ (Woodward and Masters, 1992).

## 3.3 Results and Discussion

### 3.3.1 Coverage

To look at the coverage of our data, we plot the travel time residuals at their turning points, which is where rays are most sensitive to structure. Figure 3.7 shows travel time residuals binned in caps with a radius of 5° for our existing S and P data sets for rays turning in the bottom 200km of the mantle. As noted earlier, coverage is poor, particularly in the Southern Hemisphere, where large regions remain entirely unsampled. When we add diffracted residuals to the plots (plotted at the midpoint of their path along the CMB), coverage is greatly improved in the Southern Hemisphere, particularly for the P data. The remaining gaps in coverage for the S data are filled with our ScS-S data set.

### 3.3.2 Patterns in the Data

Plotting the residuals of our data sets also allows one to see the signal in the data. For both the S and P data, we see large, slow regions underneath the Pacific and Africa and fast regions underneath Asia and the Americas. These features are seen in existing tomographic models of the base of the mantle. The addition of diffracted data results in larger residuals, particularly under the Pacific and Africa.

Before inverting, we examine the patterns in our data by looking at histograms of S, P, Sdiff, and Pdiff cap averages (plotted in Figure 3.7) for five different bins of turning depth in the lower mantle (Figure 3.8). Previous studies (e.g. Bolton and Masters, 2001) have shown that the distributions of P and S residuals behave differently in the lower mantle, with S residuals showing increased variance with greater turning depth. Like Bolton and Masters (2001), we note that the distribution of S and Sdiff residuals is not Gaussian, but exhibits a distinct lump of positive residuals, which becomes smaller with decreasing depth. The positive residuals are associated with the large slow velocity anomalies underneath Africa and the Pacific. This pattern of positive residuals is also observed in the distribution of seismic velocity anomalies calculated for different

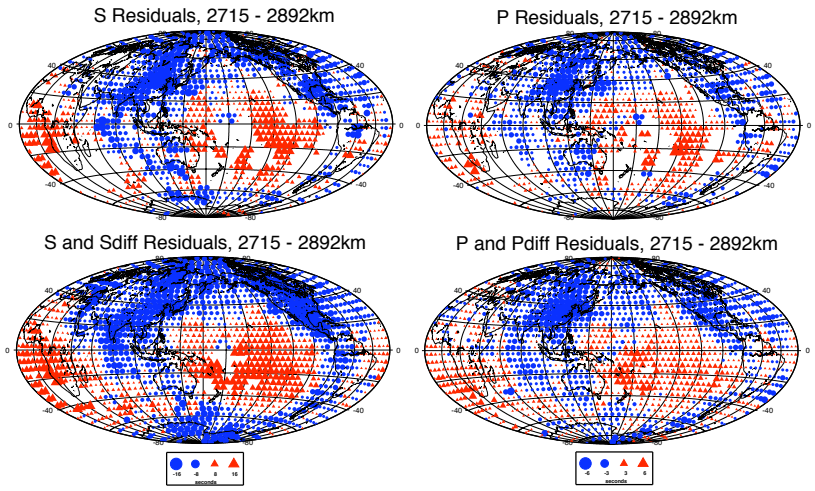


**Figure 3.7**: Coverage plots showing residuals binned in $5^o$ caps and plotted at their turning points for S (top left), P (top right), S and Sdiff (bottom left), and P and Pdiff (bottom right). Residuals for diffracted data are plotted at the midpoint of the path along the CMB. The addition of diffracted data clearly improves coverage at the base of the mantle.

S models (Hernlund and Houser, 2008). The distribution of the P and Pdiff residuals is less skewed. In fact, the Pdiff residuals do not display any obvious asymmetry at all. The deepest-turning P residuals show a small positive tail, which disappears with decreasing depth.

The correlation of shear velocity with compressional velocity, while always positive, can provide insight into the causes of velocity anomalies and thus it is worth investigating the similarity in patterns of S and P residuals. To examine the relative behavior of shear and compressional velocity, we take our previously calculated turning depth binned cap averages (Figure 3.7) and construct scatterplots of the S versus P residuals for corresponding caps (Figure 3.9). At the base of the mantle, we include our Sdiff and Pdiff residuals. The slope is steepest at the base of the mantle, with a value of 5.5, reflecting the greater variance in S and Sdiff residuals relative to P and Pdiff. As we move up in the depth, the slope decreases to 3.8 and does not decrease further for the layers shown. The higher slope at the base of the mantle has been observed in other studies (e.g. Robertson and Woodhouse, 1996; Bolton and Masters, 2001) and implies

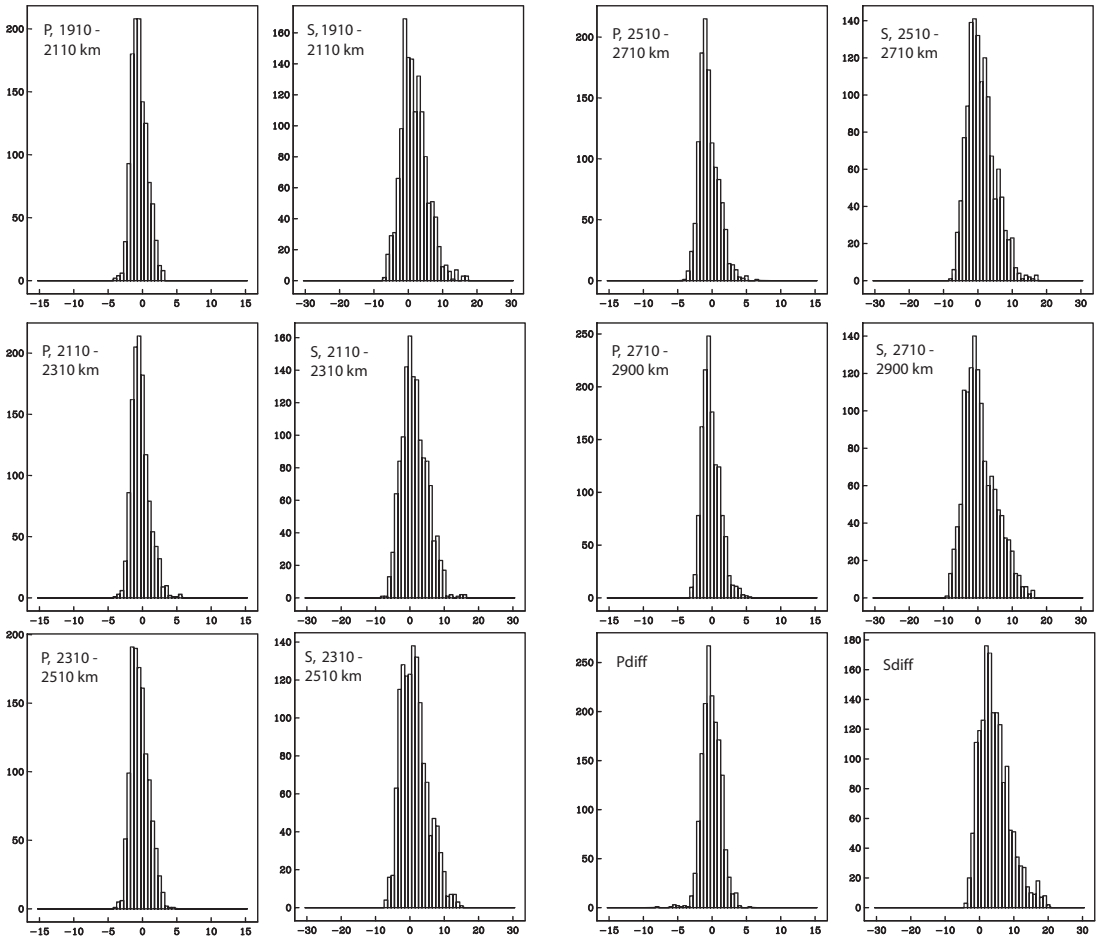


**Figure 3.8**: Histograms of P and S cap averages for five layers of ray turning depth.

that the causes of velocity anomalies cannot be due to thermal effects alone.

### 3.3.3 S and P Models

Figure 3.10 shows the results of our shear and compressional velocity inversions. The S model is similar to existing models with large slow anomalies beneath the Pacific and Southern and Western Africa and fast anomalies beneath eastern Asia and the Americas. However, the addition of the diffracted data does result in improved definition of the slow region beneath the Pacific. The model fits the data well, with a $\chi^2$ fit of 1.1, 1.02, 1.47, 1.29, and 2.17 for our S, Sdiff, SS-S, ScS-S, and sS-S data sets, respectively.

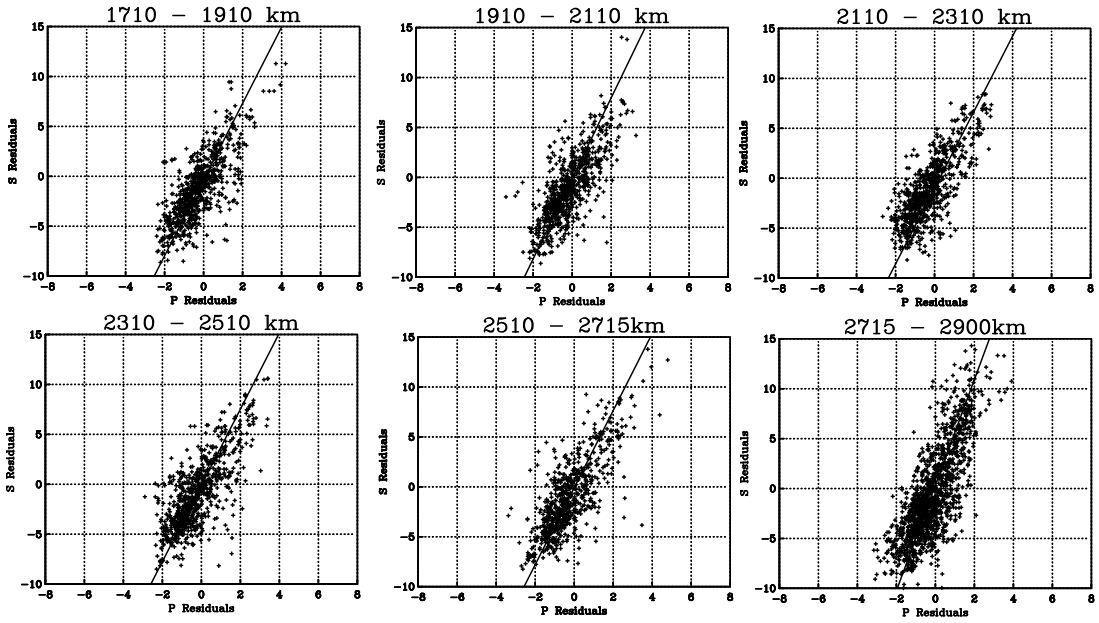


**Figure 3.9**: Scatterplots of P and S residuals for five layers of ray turning depth. The lowermost layer includes the Sdiff and Pdiff residuals. The slope is 5.5 at the base of the mantle and approximately 3.8 for the remaining layers of the mantle shown.

The P model shows a similar pattern of anomalies to our shear velocity model, although, in contrast to the shear velocity model, the amplitudes are smaller. The model fits the data well, with a $\chi^2$ fit of 1.07, 1.17, 1.23, and 2.24 for the P, Pdiff, PP-P, and pP-P data sets, respectively. The poor fit of the models to the depth phase data sets reflects their sensitivity to structure at the bouncepoint of pPthat is smaller than our block size.

**Resolution and Errors**

To test resolution, we create a checkerboard model for a single layer and use it to make synthetic data. The synthetic data are then inverted to determine how well our ray path geometry can retrieve the structure and amplitudes of the velocity perturbations. Figure 3.11 shows the results of the checkerboard resolution test for the S model both with and without diffracted data. The addition of diffracted data improves resolution, particularly in the Southern Hemisphere, where structure was previously not as well resolved. The improvement in resolution is even better for the Pdiff data (Figure

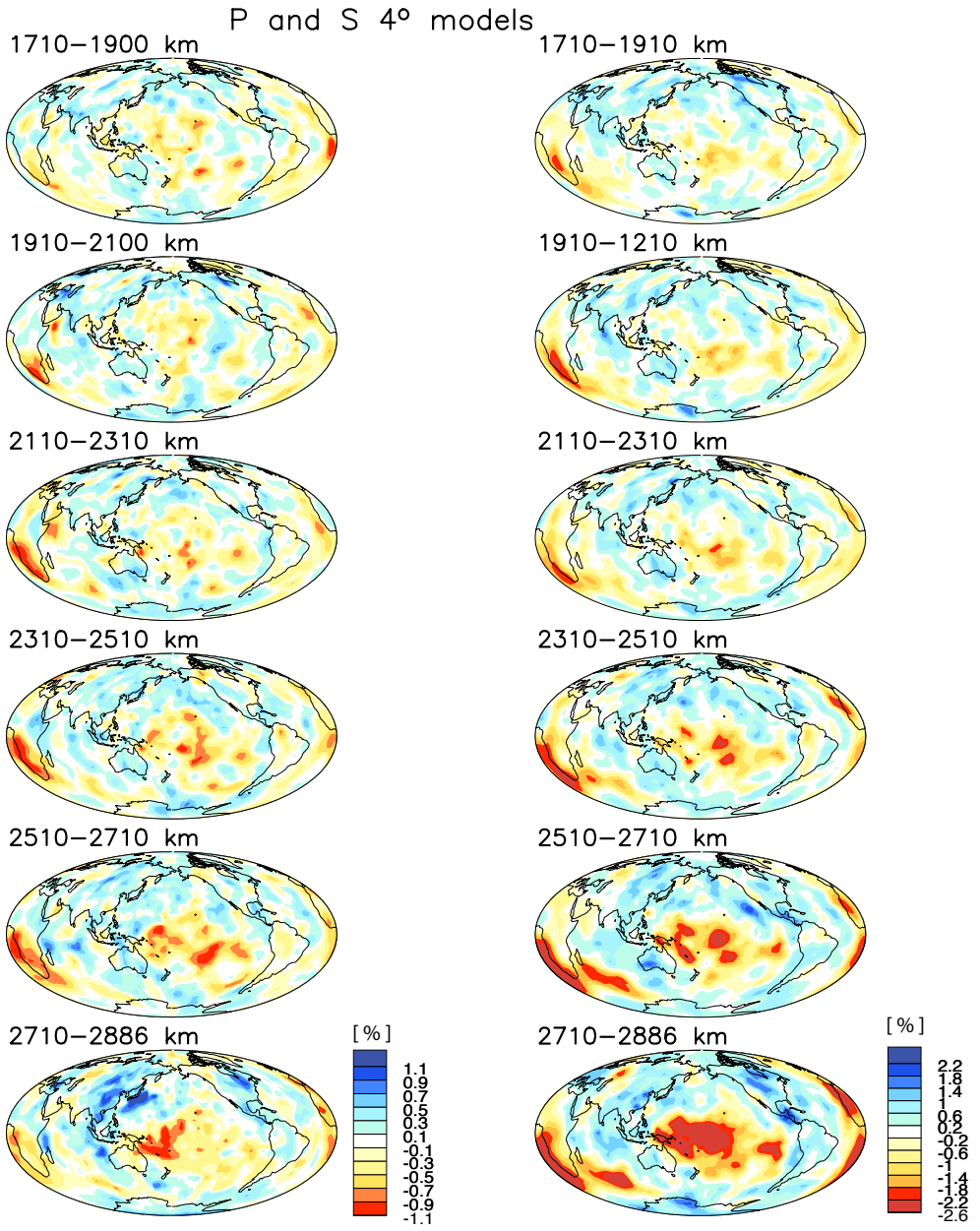


**Figure 3.10**: Slices of the bottom six layers of the mantle showing perturbation in compressional (left) and shear (right) velocity relative to ak135. The S model was made using the S, Sdiff, SS-S, ScS-S, and sS-S data sets. The P model was made using the P, Pdiff, PP-P, and pP-P data sets.

3.12). Without the diffracted data, resolution is quite poor, with limited pattern recovery in the Northern Hemisphere only. The addition of the Pdiff data set improves resolution significantly, with almost all of the Northern and Southern Hemisphere now well resolved.

To determine the stability of our models, we make error maps using a Monte Carlo error analysis. Gaussian noise is added to our data, which are then inverted. The process is repeated 50 times and the standard deviation of the resulting 50 models is calculated, which is taken to be an estimate of error. The standard deviations are plotted in Figure 3.13. For both models, errors at the base of the mantle are low, at least an order of magnitude lower than the signal, indicating that the features that we see at the base of the mantle are robust and well-constrained. Errors are lowest in the Northern Hemisphere, where coverage is the best.

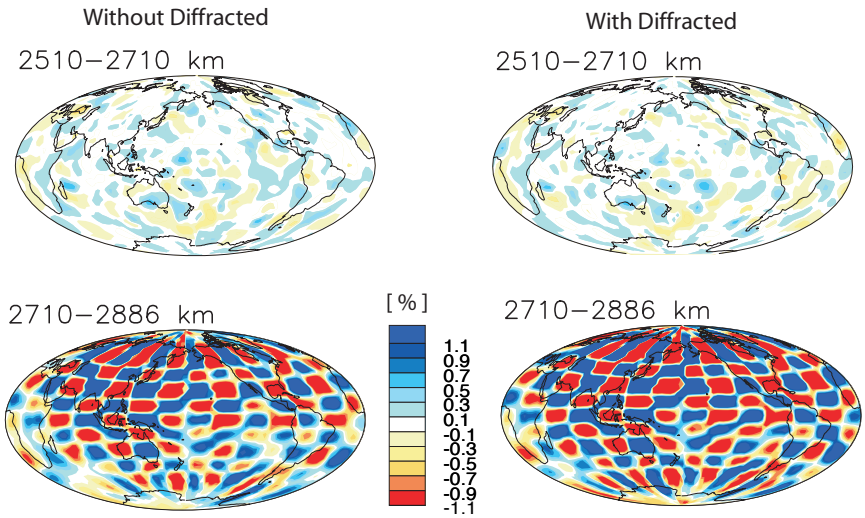


**Figure 3.11**: Slices of the base of the mantle showing the results of checkerboard test for the S model, both with (left) and without (right) diffracted data. The addition of diffracted data clearly improved resolution.

### Comparison With Other Models

By comparing our model to existing S models, we can examine how the addition of diffracted data changes our resolution (Figure 3.1). The models include J362D28 (Antolik et al., 2003), SAW642AN (Panning and Romanowicz, 2006), HMSL-S06

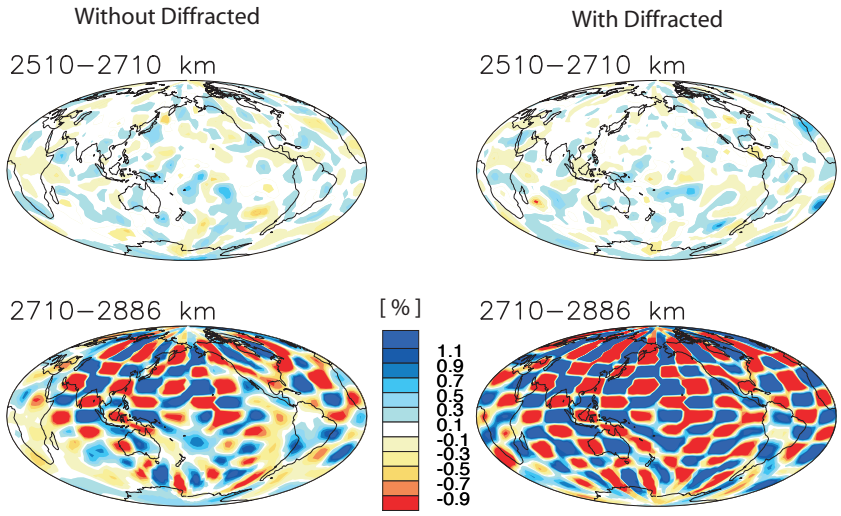


**Figure 3.12**: Slices of the base of the mantle showing the results of checkerboard test for the P model, both with (left) and without (right) diffracted data. The addition of diffracted data clearly improved resolution.

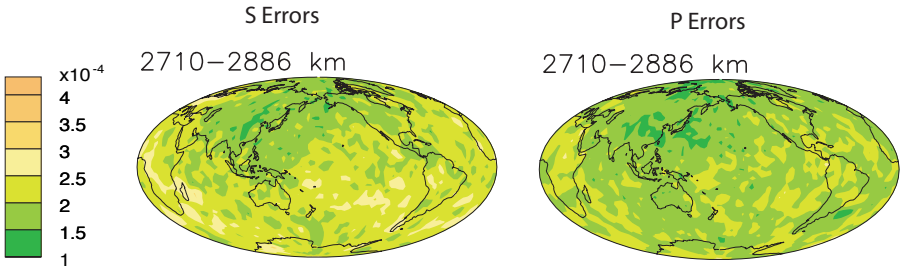


**Figure 3.13**: Slices of the base of the mantle showing error maps for the S (left) and P(right) model.

(Houser et al., 2008), S20RTS (Ritsema et al., 1999), TX2006 (Simmons et al., 2006), and PRI-S05 (Montelli et al., 2006). As noted earlier, the models exhibit the same long-wavelength structure (i.e. large slow velocity anomalies underneath the Pacific and Africa surrounded by a ring of fast velocity anomalies), but the finer scale structure, as well as the strength of the anomalies differ. There is quite a range in the amplitudes of the large slow velocity regions underneath the Pacific and Africa, in particular, with both S20RTS and SAW642AN having lower amplitudes.

The correlation of the models with the new model (Figure 3.2) is relatively high in the lower mantle, with correlation values greater than 0.8 for four of the five

models (J362D28, HMSL-S06, S20RTS, and TX2006). Our new model correlates best with HMSL-S06, which is not surprising, since the two models use the same S, SS-S, and ScS-S data sets. Only SAW642AN correlates less well with our model, with correlations of less than 0.6 at the base of the mantle. The differences in the models can probably be attributed to the different data sets and methodologies that were used in their construction. The models that are most similar to our model (HMSL-S06, S20RTS, TX2006, and PRI-S05) all use arrival times to map shear velocity at the base of the mantle, whereas SAW642AN uses waveforms and also includes anisotropy. The use of finite-frequency kernels in PRI-S05, as opposed to ray theory, does not result in a significantly different model at long wavelength.

Whereas existing shear velocity models of the base of the mantle show similar features, compressional models of the base of the mantle are not as robust and the structures are not as well constrained. As shown in Figure 3.7, P waves alone provide poor coverage at the base of the mantle. This lack of resolution becomes evident when we compare existing P models at the base of the mantle (Figure 3.3). The models include J362D28 (Antolik et al., 2003), HMSL-P06 (Houser et al., 2008), MIT-P07 (Li et al., 2006), and PRI-P05 (Montelli et al., 2006). All exhibit large slow velocity anomalies underneath Africa and the Pacific, however, the extent and shape of these slow anomalies varies from model to model. The amplitudes at the base of the mantle vary as well, with much lower amplitudes in MIT-P07 and J362D28. None of the models correlate particularly well with our new model at the base of the mantle, with correlations between 0.5 and 0.6 (Figure 3.4), which is probably due to the lack of coverage in the existing P models.

### 3.3.4 Bulk Sound Speed Inversion

As discussed earlier, the correlation of shear velocity with bulk sound speed can provide insight into the physical origin of velocity anomalies. Observations of a negative correlation between shear velocity and bulk sound speed in the lower mantle in previous studies (e.g Su and Dziewonski, 1997; Masters et al., 2000; Antolik et al.,

2003) suggest the presence of chemical or phase heterogeneity at the base of the mantle. The results of our joint shear and bulk sound speed inversion for the lowermost layer of the mantle can be seen in Figure 3.14. The shear model is, as expected, similar to previous models, with large slow velocities underneath the Pacific and Africa and a faster ring surrounding the Pacific. The bulk sound speed model shows the expected pattern of anti-correlation seen in earlier models (e.g. Su and Dziewonski, 1997; Masters et al., 2000), with fast regions underneath the Pacific and Africa and slow regions surrounding the Pacific. The presence of anti-correlation implies the presence of chemical or phase heterogeneity. The lateral and vertical extent of the anti-correlation will be examined in more detail in another paper.

Figure 3.15 shows the results of a checkerboard resolution test for the joint inversion both with and without the diffracted data. We only show the results of the test for the bulk sound speed model, since the resolution of the shear velocity model was already discussed earlier. The addition of diffracted data improves the resolution significantly. Without diffracted data, we are only able to resolve structure in parts of the Northern Hemisphere, since that is where we have good coverage from both deep-turning S and P data. In fact, parts of the Southern Hemisphere, in particular, underneath Africa, remain entirely unresolved. With the addition of diffracted data, we are able to resolve structure in both the Northern and Southern hemisphere, although amplitude recovery is still limited in parts of the Southern hemisphere.

## 3.4 Conclusions

Using cluster analysis, we have created a data set of 35,000 Pdiff and 27,000 Sdiff arrival times. The inclusion of these data sets into our inversion improves coverage and resolution at the base of the mantle, particularly in the Southern Hemisphere. Plots of travel time residuals at their turning points show large, slow regions underneath the Pacific and Africa and fast regions underneath Asia and the Americas for both the Pdiff and Sdiff data sets. The addition of diffracted data results in larger residuals, particularly

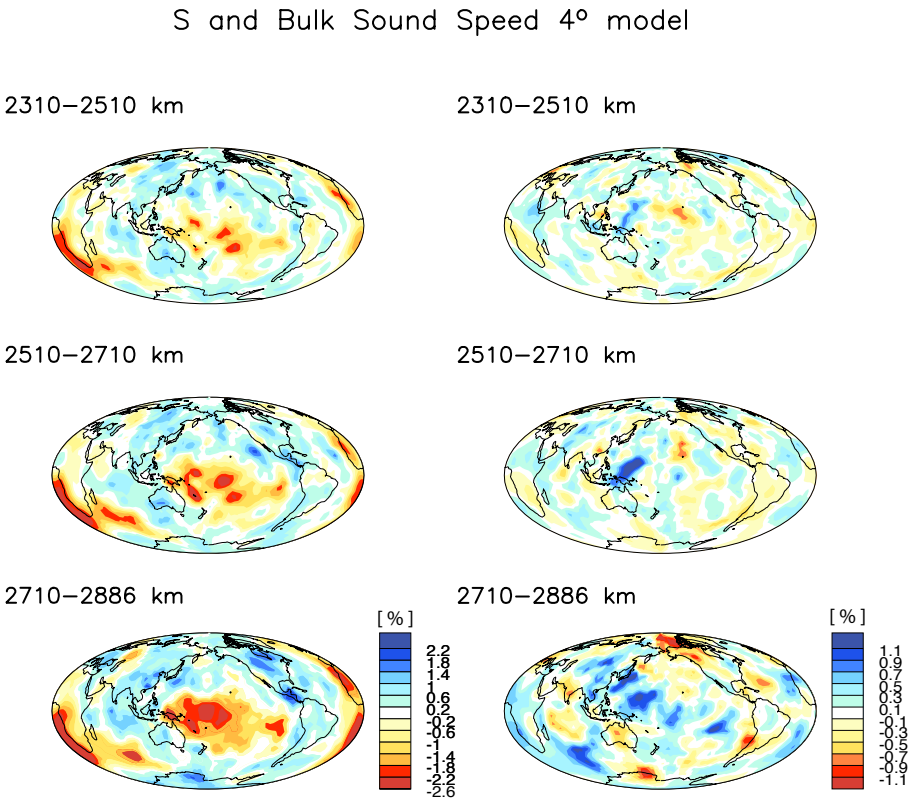


**Figure 3.14**: The bottom three layers of the mantle showing the results of our joint inversion for shear velocity and bulk sound speed.

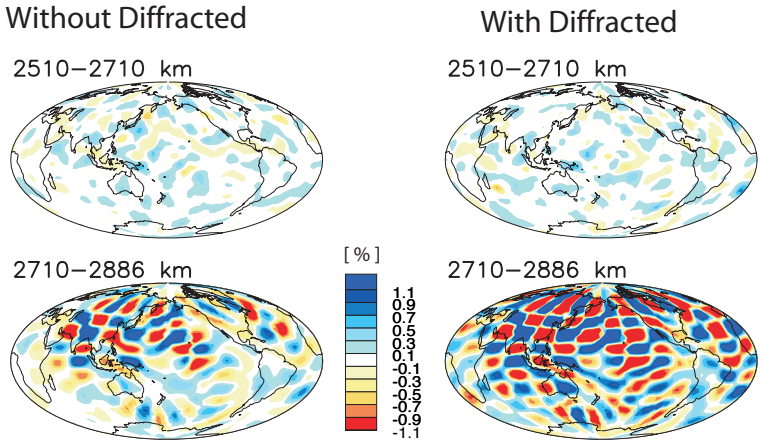


**Figure 3.15**: Slices of the base of the mantle showing the results of checkerboard test for the bulk sound speed model, both with (left) and without (right) diffracted data. The addition of diffracted data clearly improved resolution.

in the large, slow regions underneath the Pacific and Africa. Histograms of the S and Sdiff residuals show a non-Gaussian distribution, with a large positive tail that decreases in size with decreasing depth. This tail is not as prominent in the P data and not present at all in the Pdiff data. Plots of S versus P residuals have a steeper slope at the base of the mantle, indicating that the velocity anomalies cannot be due to thermal effects alone.

Our new shear velocity model is similar to existing models, with improved definition of slow velocity regions underneath the Pacific and Africa. Our new compressional velocity model correlates less well with existing P models at the base of the mantle, with large differences in both the shape and amplitudes of the large slow velocity anomalies underneath the Pacific and Africa.

We also jointly inverted for shear velocity and bulk sound speed. The pattern of anti-correlation observed in earlier studies is still seen at the base of the mantle. Resolution tests show that the inclusion of diffracted data improves resolution significantly. Without diffracted data, we are only able to resolove parts of the Northern Hemisphere, whereas with diffracted data, we are able to recover structure in both hemispheres.

The models in this study were made using ray theory. In the future, we plan to apply finite-frequency kernels to the diffracted data set.

## 3.5 Acknowledgements

Chapter 3 (Manners, U.J. and G. Masters (2008), An analysis of core-mantle boundary structure using S and P diffracted waves.) has been submitted in full for publication in *Geophysical Journal International*. The dissertation author was the primary investigator and author of this paper.

# 4

# Relations between shear velocity and bulk sound speed in the lower mantle

**Abstract**

The base of the mantle is characterized by many unusual features, including the anti-correlation of shear velocity and bulk sound speed. The spatial extent of the anti-correlation, however, is not well determined, due to poor coverage by standard seismic phases. In this paper, we directly image bulk sound speed by combining S and P residuals for matching source-receiver pairs to create a 'bulk sound speed' residual. These residuals can be plotted to determine the coverage and nature of the signal. Using this technique, we created a data set of approximately 93,000 bulk sound speed residuals, by combining our S and P, Sdiff and Pdiff, and SS-S and PP-P travel times. Plots of residuals at their turning points show the pattern of anti-correlation seen in earlier studies, however, coverage is limited by the relatively small size of our data set. To evaluate the effects of earthquake mislocation on the correlation of shear velocity with bulk sound speed, we made bulk sound speed residuals with three different sets of earthquake locations. We also show the results of a joint inversion for shear velocity and bulk sound speed, made using projected data, which are insensitive to earthquake location. Models derived from our data show that correlation is dependent on earthquake location, although shear velocity is negatively correlated with bulk sound speed at the base of the mantle for all models. The largest changes in correlation occur at long wavelengths.

The anti-correlation of shear velocity with bulk sound speed at the base of the mantle implies the presence of chemical heterogeneity.

## 4.1 Introduction

The base of the mantle is one of the most enigmatic regions of the Earth. One of the more unusual observations in this region is the anti-correlation of shear velocity and bulk sound speed (e.g. Su and Dziewonski, 1997; Masters et al., 2000; Antolik et al., 2003; Ishii and Tromp, 2004). Tomographic models of the mantle typically invert for shear and/or compressional velocity. Compressional velocity, however, is sensitive to both shear and compression, as given by:

$$\rho {v_p}^2 = K_s + \frac{4}{3}\mu \tag{4.1}$$

where $K_s$ is the bulk modulus, $\mu$ is the shear modulus and $\rho$ is density. Shear velocity is just:

$$v_s = \sqrt{\frac{\mu}{\rho}} \tag{4.2}$$

In order isolate the compressional component, one can look at the variations in bulk sound speed, which is defined to be:

$$v_c = \sqrt{\frac{K_s}{\rho}} = \sqrt{{v_p}^2 - \frac{4}{3}{v_s}^2} \tag{4.3}$$

One is now able to separate out the effects of shear and compression. Studying the relative variations in shear velocity and bulk sound speed allows one to determine the cause of velocity anomalies. For a thermal anomaly, one expects shear velocity and bulk sound speed to be positively correlated. A negative correlation cannot be explained by thermal effects alone and thus implies the presence of phase or chemical heterogeneity. Previous studies of the base of the mantle (e.g. Su and Dziewonski, 1997; Masters et al., 2000; Antolik et al., 2003) have shown that shear velocity and bulk sound speed are anti-correlated in the lower mantle, indicating the presence of chemical heterogeneity or phase changes in this region.

Historically, three-dimensional models of the mantle have been made using short period data obtained from the International Seismological Centre (ISC) (e.g. Bijwaard et al., 1998; Kennett et al., 1998; Vasco and Johnson, 1998; Boschi and Dziewonski, 2000; Karason and van der Hilst, 2001; Li et al., 2006). The ISC data set has the benefit of being very large, with P arrival times now numbering in the millions. ISC S wave arrivals, however, tend to be noisy because they are not well recorded on short period instruments and are frequently misidentified, particularly with interfering SKS phases beyond $80^o$. Consequently, models made using ISC data typically only invert for compressional velocity. The lack of a corresponding shear velocity model means that one cannot compare variations in shear velocity and bulk sound speed. Nevertheless, several shear and compressional models using ISC data have been made (e.g. Robertson and Woodhouse, 1995, 1996; Kennett et al., 1998; Vasco and Johnson, 1998).

Studies using ISC data have reached different conclusions about the behavior of shear velocity and bulk sound speed at the base of the mantle. Robertson and Woodhouse (1996) showed that the ratio of relative S to P velocity heterogeneity from their models indicates that the shear and bulk moduli are uncorrelated in the deep mantle. However, due to the contamination of S with SKS past 80 $^o$, they only inverted to a depth of 2000km. Similarly, Kennett et al. (1998) determined that the correlation between shear velocity and bulk sound speed diminishes with depth. A more recent study by Saltzer et al. (2001) looked at P and S wave heterogeneity in the mantle using ISC P and S travel times for common source-receiver pairs. Unlike Robertson and Woodhouse (1995) and Bolton and Masters (2001), they found that the ratio of shear velocity to P velocity decreased with depth. Their models, however, are poorly resolved at the base of the mantle. Saltzer et al. (2001) also combined their S and P models to make a bulk sound speed model, but saw no significant correlation between shear velocity and bulk sound speed through most of the mantle. They did note a negative correlation between 1700 and 2100 km depth and a positive correlation between shear velocity and bulk sound speed at the base of the mantle, which is not in agreement with previous studies (e.g. Su and Dziewonski, 1997; Masters et al., 2000).

Given the inherent problems of using ISC data, an alternative approach is to use long period data collected from global databases of long period and broadband seismic waveforms. Long period data sets have the benefit of being of better quality, but their long wavelength means that smaller scale structure cannot be resolved. However, many secondary phases can be picked, which improve resolution. Several studies have combined long period data with ISC data, which allow them to take advantage of the huge ISC P travel time data set, while using better quality measurements for other phases (e.g. Su and Dziewonski, 1997; Antolik et al., 2003). Su and Dziewonski (1997) jointly inverted for shear velocity and bulk sound speed, whereas Antolik et al. (2003) made a bulk sound speed model by combining their shear and compressional velocity models. Both of these studies show a negative correlation of shear velocity and bulk sound speed throughout the entire lower mantle. Masters et al. (2000), on the other hand, used only long period data sets, consisting of surface wave measurements, body wave travel times, and normal mode structure coefficients to jointly invert for shear velocity and bulk sound speed. The results of this study show a negative correlation of shear velocity and bulk sound speed starting at a depth of approximately 2000km. While the presence of anti-correlation between shear velocity and bulk sound speed is a feature common to many models, the spatial extent of the anti-correlation is clearly not well constrained.

At the longest wavelengths are models derived from normal mode spectral measurements (e.g. He and Tromp, 1996; Resovsky and Ritzwoller, 1998; Masters et al., 2000; Beghein et al., 2002; Ishii and Tromp, 2004). Free oscillation structure coefficients have been used to look at the relative variation of shear and bulk sound speed (e.g. Masters et al., 2000; Ishii and Tromp, 2001, 2004). Both Masters et al. (2000) and Ishii and Tromp (2004) found shear velocity and bulk sound to be strongly anti-correlated at the base of the mantle, particularly at long wavelengths.

Also hampering our understanding of anti-correlation at the base of the mantle is the difficulty in obtaining good bulk sound speed models. The simplest bulk sound speed models are constructed by combining S and P velocity models, using the relationship given in equation 16. This is not, however, a very safe approach due to trade-offs

with source location (Manners and Masters, 2008a). Simultaneous inversions for shear velocity and bulk sound speed are more complex, however, many trade-offs are possible and changing the smoothing or parameterisation can change the bulk sound speed model significantly.

Unlike with our S and P data, we cannot simply plot residuals at their turning points and verify whether the pattern in the data matches the pattern in the model. To overcome this problem, we have developed a technique to directly image bulk sound speed by combining S and P residuals for matching source-receiver pairs to create a 'bulk sound speed' residual. These residuals can be plotted to determine the coverage and nature of the signal. Not only does such an approach allow us to see the pattern in our data before inverting them, it also allows us to invert directly for bulk sound speed. We also present the results of a joint shear velocity and bulk sound speed inversion.

## 4.2 Method

### 4.2.1 Data

To model the mantle, we use existing data sets of S, Sdiff, SS-S, ScS-S, sS-S, P, Pdiff, PP-P, and pP-P travel times (see Table 4.1) from events occurring between 1976 and 2005. We also include surface wave dispersion measurements (Masters et al., 2000, *Laske*, personal communication) and normal mode coefficients (Masters et al., 2000). The travel time measurements were made on long-period data with a dominant period of 20 s. The arrival times were picked manually or using cluster analysis (Houser et al., 2008), which allows us to process a large amount of data in a short amount of time, while retaining quality control. The data are corrected for the effects of the crust using CRUST 2.0 (Bassin et al., 2000) as well as for the Earth's ellipticity (Kennett and Gudmundsson, 1996).

**Table 4.1**: Phases and number of measurements included in study

| Phase | Number of Picks | Years |
|---|---|---|
| P | 182724 | 1976 - 2005 |
| Pdiff | 34774 | 1986 - 2005 |
| PP-P | 26116 | 1976 - 1999 |
| S | 169832 | 1976 - 2005 |
| Sdiff | 26706 | 1986 - 2005 |
| SS-S | 32266 | 1976 - 1999 |
| ScS-S | 26840 | 1976 - 2005 |
| pP-P | 23184 | 1976 - 2005 |
| sP-P | 26615 | 1976 - 2005 |
| sS-S | 30223 | 1976 - 2005 |

### 4.2.2 Bulk Sound Speed Residuals

We create bulk sound speed rays by combining S and P travel times residuals for common source-receiver pairs. As noted earlier, bulk sound speed can be calculated by combining shear velocity and compressional velocity (equation 16). With a few assumptions, we can combine shear velocity travel times with compressional travel times to obtain bulk sound speed travel times, as given by:

$$\delta T_c = C_1 \delta T_p - C_2 \delta T_s \tag{4.4}$$

where

$$\delta T = - \int_{ray} \frac{\delta v}{v^2} d\Gamma \tag{4.5}$$

The values for C1 and C2 are given by:

$$C_1 = \left( \frac{1}{1-x} \right)^{\frac{3}{2}} \simeq 2.15 \tag{4.6}$$

and

$$C_2 = \sqrt{\frac{3}{4}} \left( \frac{x}{1-x} \right)^{\frac{3}{2}} \simeq 0.47 \tag{4.7}$$

and

$$x = \frac{4 {v_s}^2}{3 {v_p}^2} \tag{4.8}$$

We have assumed that *x* is approximately equal to 0.4 and is largely independent of depth as found in all 1D models. We also assume that the S and P ray paths are sufficiently

similar and sample practically the same structure. In fact, there is a maximum deviation of S and P ray paths of about 150 km, which is sufficiently small for our purposes. After creating bulk sound speed residuals, we calculate bulk sound speed ray paths relative to a 1D bulk sound speed model, which is calculated by combining the 1D S and P models of ak135 (Kennett et al., 1995) using equation 3. We apply this technique to our S and P, Sdiff and Pdiff, and SS-S and PP-P residuals.

### 4.2.3 Locations

Earthquake mislocation is a large source of error in our inversions, particularly for our P data, where the size of the error is similar in size to the signal from 3D structure (Bolton and Masters, 2001). Since bulk sound speed residuals are made using P data, mislocation error must be properly dealt with, lest it propagate into our bulk sound speed models. In previous work (Manners and Masters, 2008a), we handled mislocation error by jointly inverting for velocity structure and hypocenter, as given by:

$$\delta \mathbf{t} = \begin{bmatrix} \gamma \mathbf{A} & \mathbf{B} \end{bmatrix} \begin{bmatrix} \gamma^{-1} \delta \mathbf{h} \\ \delta \mathbf{v} \end{bmatrix} \tag{4.9}$$

where $\mathbf{A}$ is a matrix containing the travel time derivatives with respect to location, $\delta \mathbf{h}$ is a vector representing the perturbation in location and origin time, $\mathbf{B}$ is the matrix of velocity derivatives, and $\delta \mathbf{v}$ is a vector representing the relative 3D perturbations in velocity. The value of $\gamma$ controls how much we weight the velocity versus the relocation part of the inversion.

Since we are not interested in solving for location in this study, we use the locations previously determined using this method (Manners and Masters, 2008a). To investigate how location affects the correlation of shear velocity with bulk sound speed, we create two additional sets of travel time residuals. The first set is made using the locations of Engdahl et al. (1998) (EHB locations). Engdahl et al. (1998) relocated nearly 100,000 events from the ISC catalogue using ak135 as a 1D reference model. The EHB locations, however, are determined using short-period data, which ”see” arrivals

coming from the onset of rupture earlier than long-period data, giving an earlier origin time than would be determined using long-period data. The shift in origin time is also a function of the moment of the event, with offset increasing with moment (Kanamori and Anderson, 1975). If this offset is not corrected for when using long period data, it can be mapped into structure, potentially changing the correlation between shear velocity and bulk sound speed. We correct for this offset by replacing the EHB origin times with the origin times of our new locations which were determined using long period data. These corrected locations are then used to make a third data set of bulk sound speed residuals.

### 4.2.4 Inversions

The following section describes our inversions. Models are parameterized by 18 layers, which are 100 km thick in the upper mantle and 200 km thick in the lower mantle. Each layer is divided into $4^o$ equal area blocks. We apply first difference smoothing both radially and laterally. Data are weighted by their errors in the inversion, so that better quality data are weighted more heavily. The bulk sound speed errors are determined by combining the S and P errors, such that:

$$\sigma_c = \sqrt{{C_1}^2{\sigma_p}^2 + {C_2}^2{\sigma_s}^2} \tag{4.10}$$

where $\sigma_P$ and $\sigma_S$ are the P and S errors and $C_1$ and $C_2$ are defined in equations 6 and 7, respectively. Consequently, bulk sound speed errors are roughly twice as big as the P errors.

#### Direct Inversion for Bulk Sound Speed

To create a bulk sound speed model, we invert our bulk sound speed residuals. We seek to minimize:

$$(\mathbf{Bm} - \mathbf{d})^\mathbf{2} + \lambda^\mathbf{2}(\mathbf{Sm})^\mathbf{2} \tag{4.11}$$

where **B** is a matrix velocity derivatives, **m** is the model, **d** is the data, and **S** is the first difference operator. This leads to the set of equations:

$$\begin{bmatrix} \mathbf{B} \\ \lambda \mathbf{S} \end{bmatrix} \begin{bmatrix} \mathbf{m} \\ 0 \end{bmatrix} = \begin{bmatrix} \mathbf{d} \\ 0 \end{bmatrix} \tag{4.12}$$

which are inverted using LSQR (Paige and Saunders, 1973). We make bulk sound speed models for all three sets of locations. We also create corresponding shear velocity models using the S, Sdiff, SS-S, ScS-S, and sS-S data sets, as well as the surface wave dispersion measurements.

**Joint Inversion**

In order to compare the results of our direction inversion for bulk sound speed, we also jointly invert for bulk sound speed and shear velocity, using all of our data sets simultaneously. Rather than use our new locations, we project our data, in which we take linear combinations of data that are insensitive to location. A vector of travel time residuals $\delta \mathbf{t}$, can be represented as:

$$\delta \mathbf{t} = \mathbf{A} \cdot \delta \mathbf{h} + \mathbf{B} \cdot \delta \mathbf{v} \tag{4.13}$$

where **A** is a matrix containing the travel time derivatives with respect to location and $\delta h$ is a vector representing the perturbation in origin time and location. We multiply the above equation with a projection matrix, **P**, which is chosen such that $\mathbf{P} \cdot \mathbf{A}$ is equal to zero and that $\mathbf{P} \cdot \mathbf{E}\mathbf{P}^{\mathbf{T}}$ is diagonal. **E** is the covariance matrix of the observations, meaning that the projected data are independent, giving us:

$$\mathbf{P} \cdot \delta \mathbf{t} = \mathbf{P} \cdot \mathbf{B} \cdot \delta \mathbf{v} \tag{4.14}$$

where $\mathbf{P} \cdot \delta \mathbf{t}$ are now insensitive to location. The projected data are then jointly inverted for shear velocity and bulk sound speed, solving:

$$\Big[\mathbf{P} \cdot \delta \mathbf{t}\Big] = \begin{bmatrix} x\mathbf{P} \cdot \mathbf{B_p} & (1-x)\mathbf{P} \cdot \mathbf{B_p} \\ \mathbf{P} \cdot \mathbf{B_s} & 0 \end{bmatrix} \begin{bmatrix} \delta \mathbf{v_s} \\ \delta \mathbf{v_c} \end{bmatrix} \tag{4.15}$$

where:

$$\delta \mathbf{v_c} = \frac{\delta v_c}{v_c} = \frac{1}{1-x}\frac{\delta v_p}{v_p} - \frac{x}{1-x}\frac{\delta v_s}{v_s} \tag{4.16}$$

and

$$\delta \mathbf{v_s} = \frac{\delta v_s}{v_s} \tag{4.17}$$

Since the projected data are insensitive to first order to location, having a projected inversion gives us an independent check on the effect of locations on the correlation of shear velocity with bulk sound speed.

## 4.3 Results and Discussion

### 4.3.1 Tests on Synthetics

In order to see how well our bulk sound speed residual technique works, we tested our method on synthetic data. To construct synthetic S, Sdiff, and SS-S data sets, we traced rays through an existing 3D shear velocity model, which was made using our S, Sdiff, SS-S, ScS-S, and sS-S data sets, as well as surface wave dispersion measurements. P, PP-P, and Pdiff synthetic data were created by tracing rays through a scaled version of the shear velocity model. We used a scaling value of 1.7, which is the expected ratio of shear velocity to compressional velocity in the mantle (Woodward and Masters, 1992). Bulk sound speed residuals were then calculated by combining the synthetic data sets as described above.

We created a bulk sound speed model by combining the S and P models that we used to make the synthetic data sets, using equation 16. This model was then used to test the bulk sound speed residuals by looking at the $\chi^2$ fit of the model to the data. Since we use the observed errors for our real data and the synthetic signal is relatively small, we expect the $\chi^2$ fit to be close to zero. We found that the fit of the model to the data is very good, with values of 0.01 for the combined S and P residuals, 0.01 for the combined diffracted residuals, and 0.02 for the combined SS-S and PP-P residuals. This corresponds to a fit, in seconds, of 0.2s for the diffracted and non-diffracted residuals

and 0.3s for the differential residuals, which is significantly smaller than the typical data error, which is approximately 1s for our A quality picks.

As a second test, we did a direct inversion for bulk sound speed and examined the correlation of the resulting bulk sound speed model with the original bulk sound speed model (Figure 4.1). The expected correlation is one, since the P model is a scaled version of our S model. We found that the correlation is between 0.8 and 0.9 in the lower mantle and approximately 0.6 in the upper mantle. The poor correlation in the upper mantle reflects the poor constraint on upper mantle structure, due to the lack of turning rays. As a comparison, we also projected our synthetic data sets and jointly inverted for shear velocity and bulk sound speed. The correlation of the resulting bulk sound speed model with the original bulk sound speed model is plotted in Figure 1. The jointly inverted model correlates better with the original model in the upper mantle, with correlation values of approximately 0.7. In the lower mantle, the model correlates as well as the directly inverted bulk sound speed model, with a correlation of 0.9. Correlation with the original model is improved by reducing the radial and lateral smoothing, however, for the synthetic tests, we show the results of models made using the same smoothing as for our real data.

### 4.3.2 Real Data

**Patterns in the Data**

By combining our S and P, Sdiff and Pdiff, and SS-S and PP-P data sets, we created a data set of roughly 80,000 bulk sound speed residuals, 7600 diffracted bulk sound speed residuals, and 5700 differential bulk sound speed residuals. One of the benefits of having bulk sound speed residuals is that we can now look at patterns in the data before making a bulk sound speed model. To examine the geographical pattern of the residuals as well as the coverage, we plot residuals made using the new locations, the EHB locations, and the corrected EHB locations binned at their turning points (or midpoint of their path on the CMB for diffracted data), where rays are most sensitive to structure (Figures 4.2 and 4.3). The residuals are binned in 5° caps and plotted for

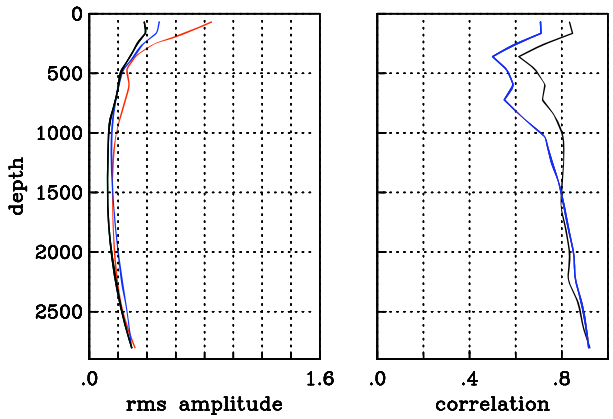


**Figure 4.1**: Amplitudes (left) and correlation (right) of synthetic bulk sound speed models. For the amplitudes, the original bulk sound speed model is plotted in red. The directly inverted model is plotted in black and the jointly inverted model is plotted in blue. For the correlation plot, the blue line is the correlation of the directly inverted bulk sound speed model with the original model, while the black line shows the correlation of the bulk sound speed model from the joint inversion with the original model.

different bins of turning depths in the lower mantle. Since we are ultimately interested in comparing the variations in shear velocity and bulk sound speed, we include plots of our S and Sdiff data as well for comparison. To examine the diffracted bulk sound speed residuals separately, the bottom row of Figure 4.2 and 4.3 plots only the diffracted residuals at their midpoints.

Bulk sound speed coverage is fairly good at the base of the mantle, aided by the ray paths of the diffracted data, with only a few areas not well sampled in the Southern Hemisphere. As we move up from the base of the mantle, coverage deteriorates, and regions of interest, such as underneath the Pacific and Africa, where large slow velocity anomalies are located, are not well sampled at all. Nevertheless, we can still see the signal in the data from 3D bulk velocity structure.

For the new locations, the pattern of anti-correlation in the residuals seen in previous studies is most evident in the plot of only the diffracted bulk sound speed residuals (Figure 4.2). The regions underneath the Pacific and Africa are fast, whereas they are slow in the plots of the Sdiff residuals. When we add in the remaining data, the pattern of anti-correlation becomes less evident, with the region underneath the Pacific

becoming slower. The pattern of anti-correlation is more complex above the base of the mantle and is not as evident. Our understanding of the patterns, however, is hampered by poor coverage in the Southern Hemisphere.

The signal in the data changes significantly for the bulk sound speed residuals made using the EHB locations (Figure 4.3). At the base of the mantle, the diffracted data show the same pattern of anti-correlation that is seen with the new locations. However, unlike the new locations, the pattern of anti-correlation extends above the base of the mantle. The region under the Pacific, in particular, remains negatively correlated with the S residuals to a depth of 2110 km, whereas for the new locations, the region underneath the Pacific is positively correlated with the S data above the base of the mantle. The bulk sound speed residuals made using the corrected EHB locations, on the other hand, resemble those made using the new locations. At the base of the mantle, the residuals are negative for areas underneath Africa and the Pacific. This pattern of anti-correlation, however, does not extend very far above the base of the mantle, with the travel time residuals becoming positive for the region underneath the Pacific, in particular.

Previous studies (e.g. Robertson and Woodhouse, 1995, 1996; Masters et al., 2000; Saltzer et al., 2001; Ritsema and van Heijst, 2002) have examined the relative behavior of shear velocity and compressional velocity, using *R*, which is defined as:

$$R = \frac{\partial ln v_s}{\partial ln v_p} \tag{4.18}$$

By comparing S and P travel times, these studies have shown that *R* increases with depth, with values greater than 2.5 in parts of the lowermost mantle, which implies that the velocity anomalies observed at the base of the mantle cannot be due to thermal effects alone. The maximum possible value of *R* due to thermal effects can be calculated by assuming that $\frac{\delta v_c}{v_c} = 0$, as would be the case in the presence of partial melt. Substituting this into equation 16 gives us a maximum value of 2.5 for *R*. Values of *R* greater than 2.5 cannot be thermally generated. In addition to being determined from seismic data, values of *R* can also be measured in laboratory experiments. Work by Karato and Karki

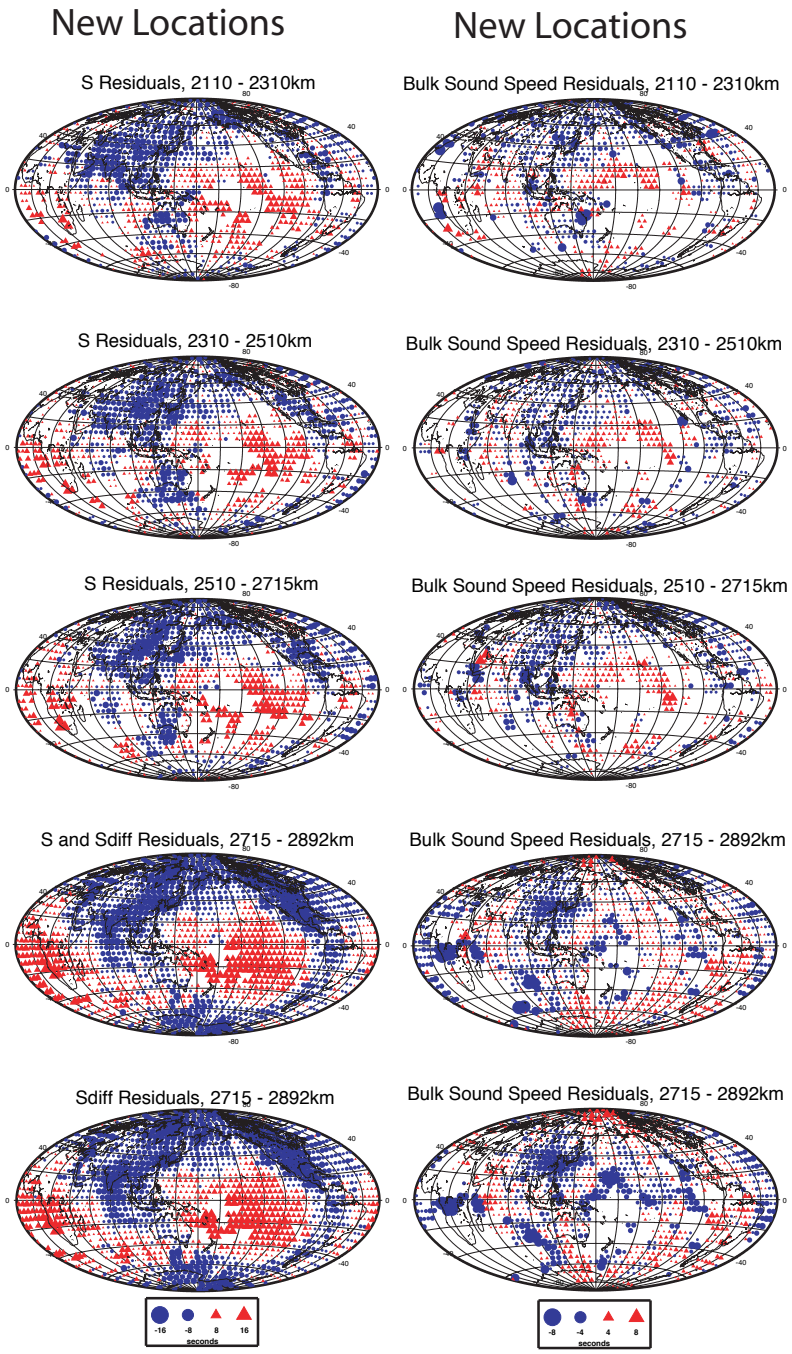


**Figure 4.2**: Coverage plots showing residuals binned in 5° caps and plotted at their turning points for S (top left) and bulk sound speed (right) for the new locations. Residuals for diffracted data are plotted at the midpoint of the path along the CMB. The bottom layer shows residuals of only the diffracted data.

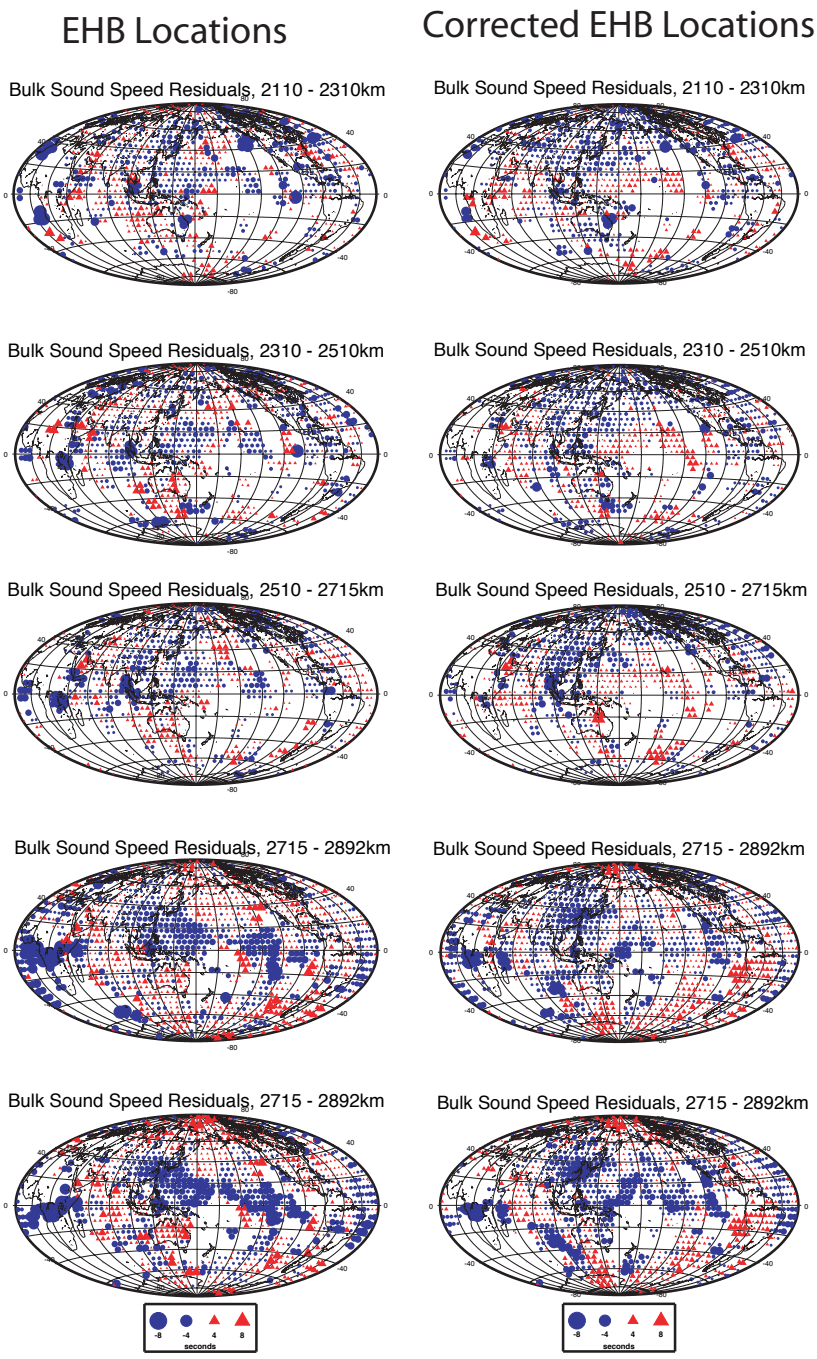


**Figure 4.3**: Coverage plots showing residuals binned in $5^\circ$ caps and plotted at their turning points for bulk sound speed for the EHB locations (left) and the corrected EHB locations (right). Residuals for diffracted data are plotted at the midpoint of the path along the CMB. The bottom layer shows residuals of only the diffracted data.

(2001) suggests that $R$ values above 2.7 need chemical heterogeneity to explain the velocity variations. More recent work by Brodholt et al. (2007) suggests that this value is too high and that the upper bound on $R$ in the lower mantle due to thermal effects is approximately 2.1 in the lower mantle.

Now that we have bulk sound speed residuals, we can similarly examine the correlation of shear velocity with bulk sound speed by looking at travel times. Figure 4.4 shows scatterplots of the binned residuals from Figure 4.2 for the bottom four layers of the mantle. The bottom row of Figure 4.4 plots residuals for just the diffracted data. The second row from the bottom plots both the diffracted and non-diffracted data. We include scatterplots for our new locations, the EHB locations, and for the corrected EHB locations.

For the new locations, only the diffracted bulk sound speed residuals are clearly anti-correlated with the diffracted S residuals. When we include the non-diffracted data at the base of the mantle, the combined data sets are not correlated with shear velocity at all. At shallower depths, the correlation becomes positive.

Using the EHB locations does change the slopes of the scatterplots, indicating that earthquake locations do affect the correlation of shear velocity and bulk sound speed. At the base of the mantle, the diffracted data are negatively correlated with shear velocity, although the slope is much steeper. With the addition of non-diffracted data, the correlation, however, remains negative. Unlike for the new locations, the negative slope extends above the base of the mantle, becoming positive first at 2500 km depth.

As with the plots of residuals at their turning points, the scatterplots made using the corrected EHB locations are similar to the plots made using the new locations. At the base of the mantle, the diffracted data are clearly anti-correlated with the Sdiff data. With the addition of non-diffracted data, the correlation becomes zero at the base of the mantle. Above the base of the mantle, the S and bulk sound speed residuals become positively correlated, with slopes similar to the scatterplots of the residuals made using the new locations.

The differing results depending upon source location illustrate the importance

of using the correct locations for one's data. While the EHB locations are good for short period data, they cannot be used for long period data without correcting for finite frequency effects. A failure to do so results in the origin time offset being mapped into structure, which changes the extent of negative correlation between shear velocity and bulk sound speed in the mantle, thereby changing the interpretation of mantle processes. The differences in hypocenter location appear to be less important, as seen in the similarity between the bulk sound speed residuals made using the new locations and the corrected EHB locations.

**Direct Bulk Sound Speed Inversion**

We present the results of our direct inversion for bulk sound speed in Figure 4.5, along with a shear model for comparison. These models were made using the new locations. The bulk sound speed model displays the same signal seen in the plots of the bulk sound speed residuals. At the base of the mantle, the model is similar to existing models, with fast regions underneath the Pacific and Africa and slow regions circumscribing the Pacific. The pattern of anti-correlation is not as evident above the base of the mantle. The $\chi^2$ fit of the model to the data is 1.33, 1.25, and 1.50 for the residuals made by combining the S and P, Sdiff and Pdiff, and SS-S and PP-P data sets, respectively.

Figure shows the result of a checkerboard resolution test. We test resolution by creating a checkerboard model for a single layer, which is then used to make synthetic data with the same ray geometry as our existing data. The synthetic data are then inverted to see how well our data can retrieve structure and amplitude in the layer. Resolution is only good in the Northern Hemisphere, reflecting the poor sampling by the bulk sound rays in the Southern Hemisphere. Unfortunately, resolution is poor in the regions which are of greatest interest, such as the large slow shear velocity anomalies underneath Africa and the Pacific. While the poor resolution suggests that directly inverting for bulk sound speed is not a satisfactory method at present, it should become more useful as the data set grows.

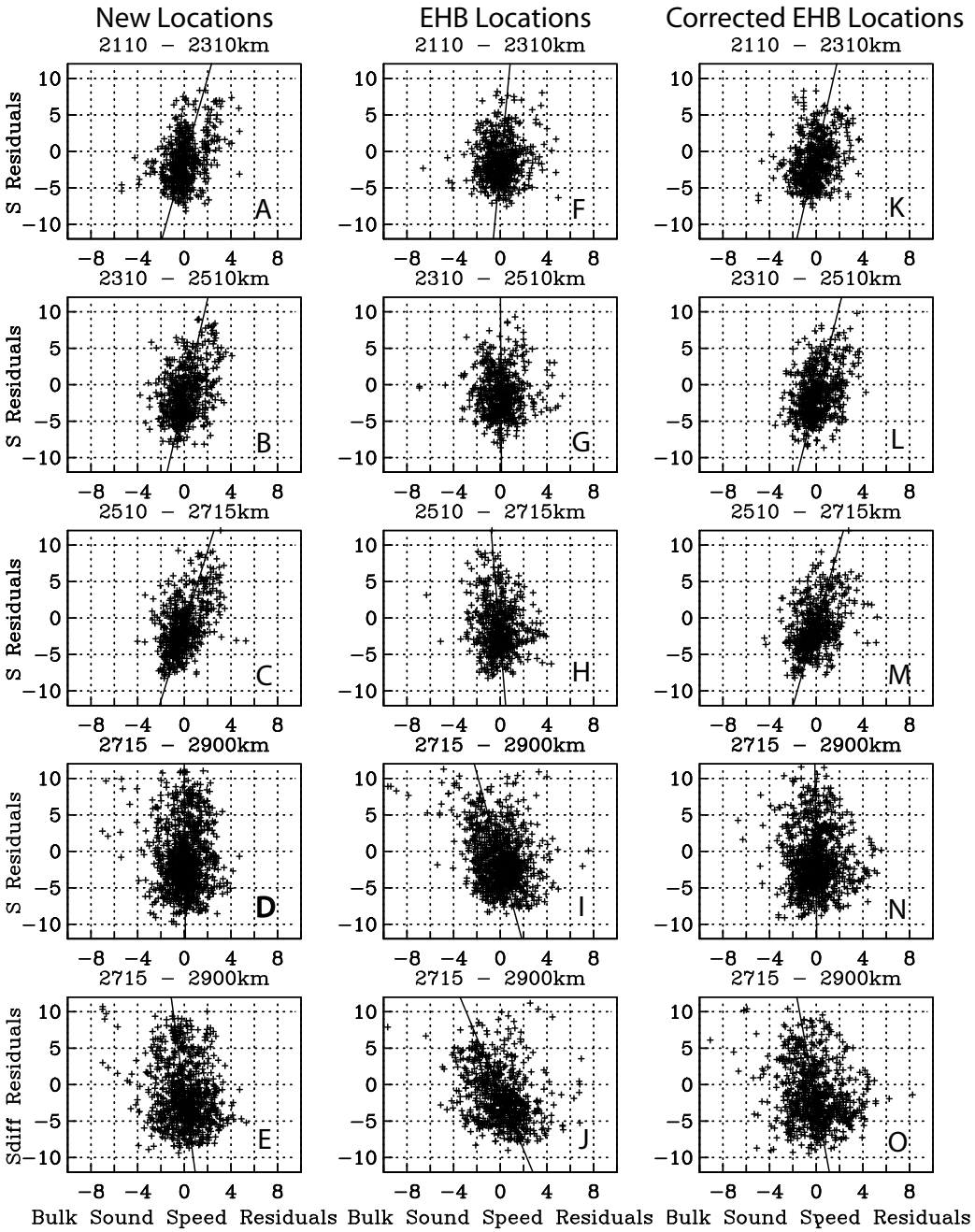


**Figure 4.4**: Scatterplots of S and bulk sound speed residuals for four layers of ray turning depth for the new locations (left), EHB locations (middle), and the corrected EHB locations (right). The lowermost layer shows a plot of just Sdiff and diffracted bulk sound speed residuals. The slopes are A: 5.7 B: 6.8 C: 5.1 D: -243.9 E: -11.6 F: 16.7 G: -250.0 H: -19.2 I: -5.9 J: -3.8 K: 7.0 L: 6.3 M: 5.6 N: -149.3 O: -8.6

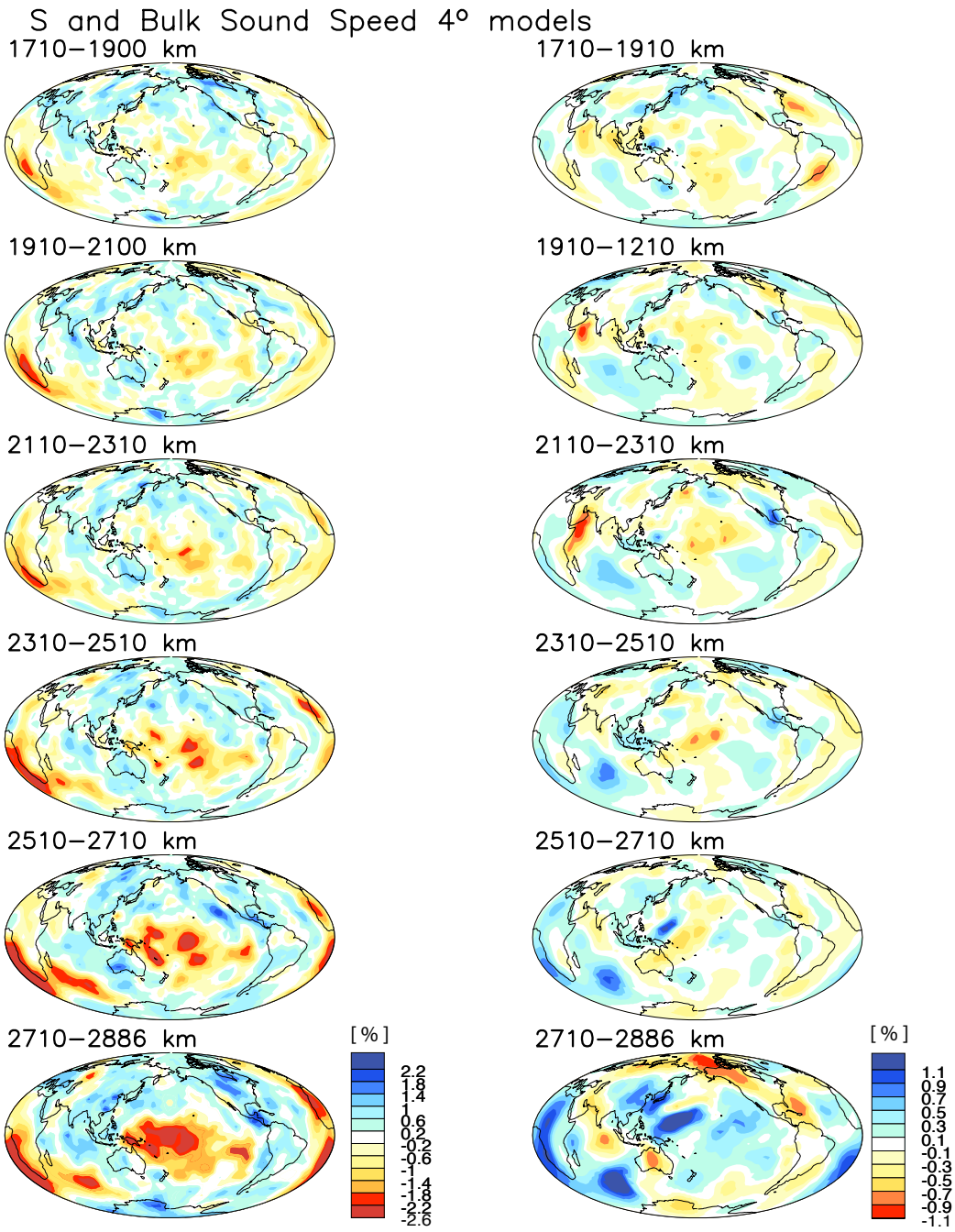


**Figure 4.5**: Slices of the bottom six layers of the mantle showing perturbation in shear velocity (left) and bulk sound speed (right) for our direct bulk sound speed inversion using our new locations.

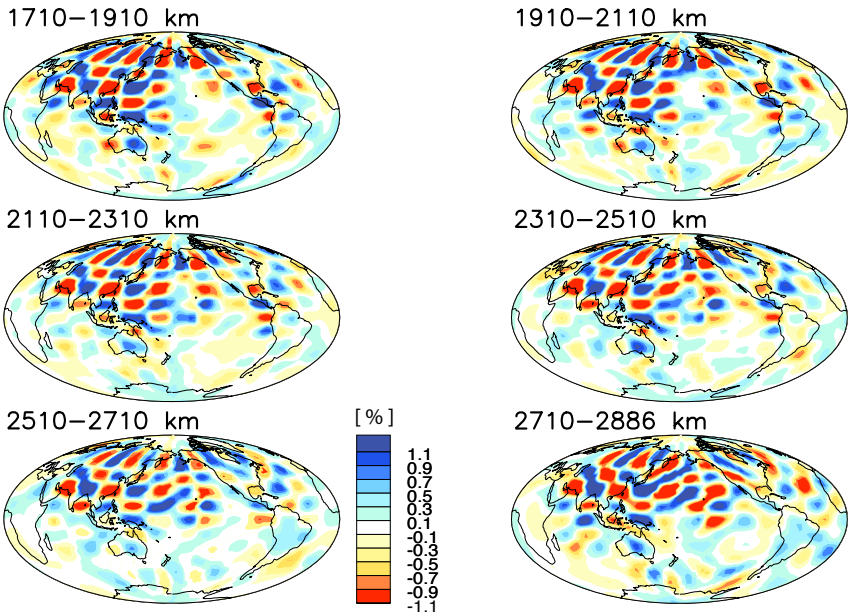


**Figure 4.6**: Slices of the bottom six layers of the mantle showing the results of a checkerboard resolution test.

To test how robust the features in our models are, we make error maps using a Monte Carlo error analysis (Figure 4.7). To estimate error, Gaussian noise is added to our data, which are then inverted. The process is repeated 50 times and the standard deviation of the resulting 50 models is calculated. The standard deviation, which is taken to be an estimate of error, is then plotted. Errors are an order of magnitude lower than the signal from 3D structure, indicating that the structures that we see in our bulk sound speed model are well-constrained. Errors are lowest in the Northern Hemisphere, where coverage is the best. The small errors imply that we could smooth the model less and fit the data better, however, using less smoothing results in the introduction of unlikely structure into the model.

### Joint Inversion

Since the current coverage of bulk sound speed residuals is not as good as we would like, the current best method for determine bulk sound speed is a joint inversion

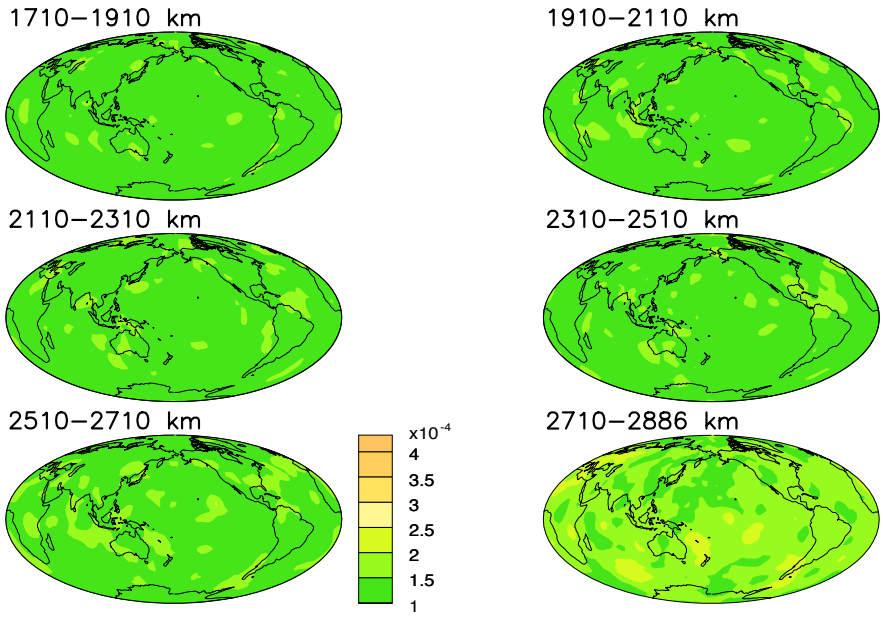


**Figure 4.7**: Slices of the bottom six layers of the mantle showing the errors for our direct bulk sound speed model.

of all our data using the projection technique to remove sensitivity to source location. The result is shown in Figure 4.8. At the base of the mantle, the bulk sound speed model is similar to the direct bulk sound speed model, with fast velocity anomalies underneath the Pacific and Africa, surrounded by slow velocity anomalies. Unlike the direct inversion, the pattern of anti-correlation extends for several layers above the base of the mantle. To determine the fit of the model to the data, we created a P model from our S and bulk sound speed models using equation 16 and calculated the $\chi^2$ fit of the P model to the projected P data. The model fits the data well with $\chi^2$ fit of 0.72. The fit to the projected S data is 1.05.

Figure 4.9 shows the result of our checkerboard resolution test for the lowermost layer of the mantle for bulk sound speed and shear velocity. Resolution is significantly better at the base of the mantle, compared to the direct inversion, with good pattern and amplitude recovery of the velocity perturbations in both the Northern and Southern Hemispheres. Leakage into the layer above the base of the mantle implies

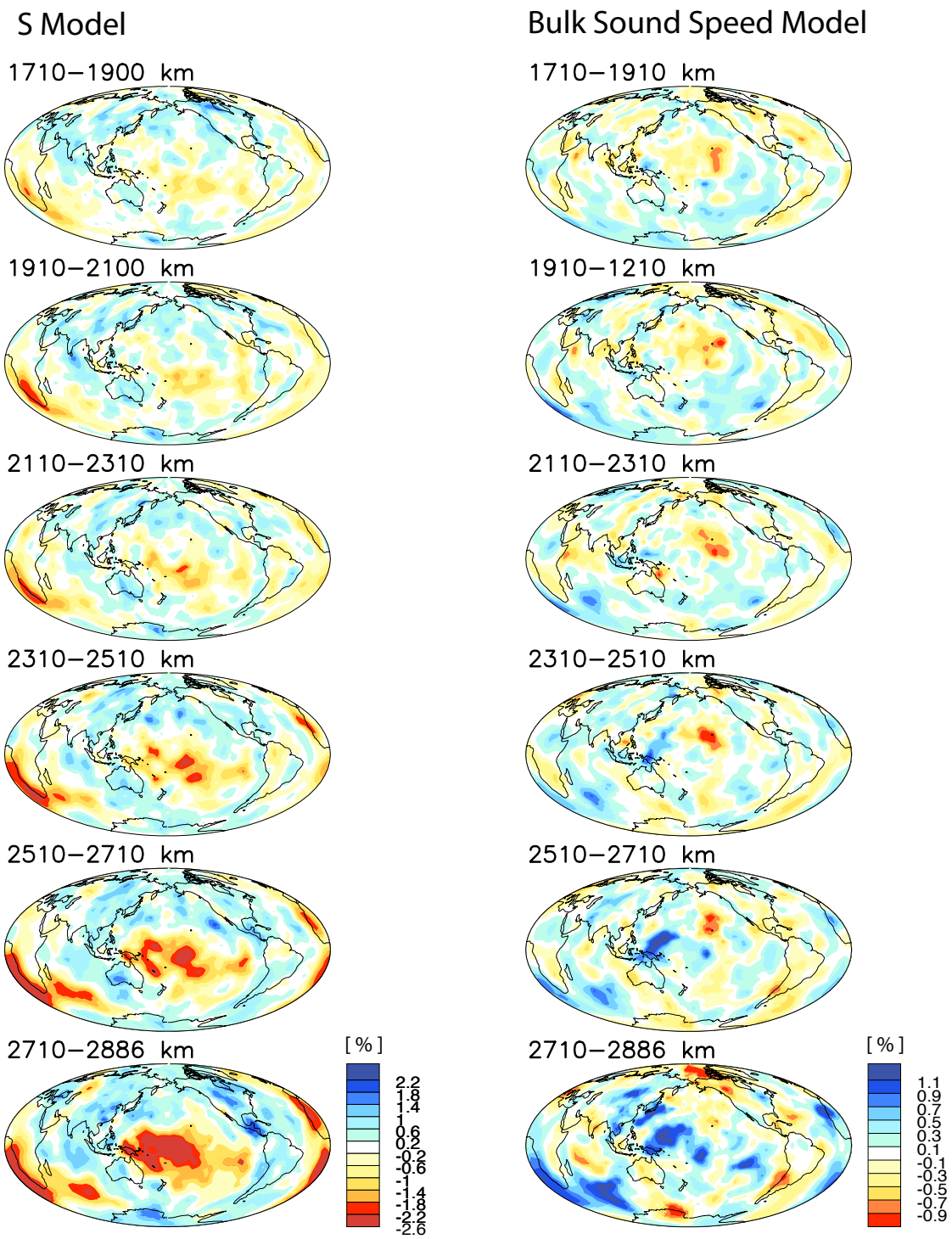


**Figure 4.8**: Slices of the bottom six layers of the mantle showing perturbation in shear velocity (left) and bulk sound speed (right) for our jointly inverted model.

that we could have used less radial smoothing. The improvement in resolution reflects the better coverage in the joint inversion. Unlike the direct inversion, the joint inversion does not require matching S and P pairs, meaning that we can use our entire data set, consisting of approximately 535,000 measurements, in the inversion. Coverage is consequently much better.

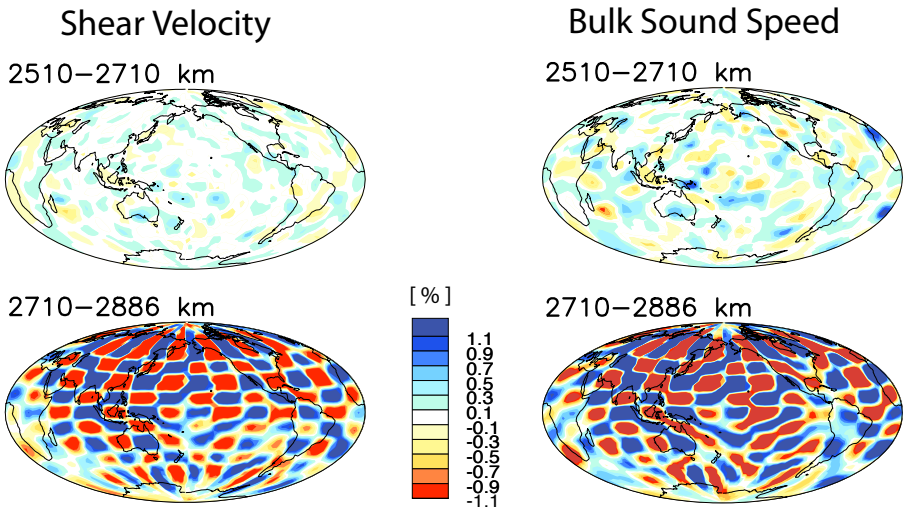


**Figure 4.9**: Slices of the base of the mantle showing the results of a checkerboard resolution test. Resolution is good for both the shear and bulk sound speed models, reflecting the significantly larger data set used in the joint inversion.

### Correlation

We examine the correlation of shear velocity with bulk sound speed by looking at the correlation as a function of wavelength and depth (Figure 4.10). Plots of the amplitudes of the models can be seen in Figure 4.11. A plot of the overall correlation is shown in Figure 4.12. While we are most interested in the correlation of shear velocity and bulk sound speed for our joint inversion, since it is the most reliable model, we include correlation plots for two of the direct inversions (using the new locations and the EHB locations) in order to examine the effects of earthquake location on correlation. The jointly projected model shows a negative correlation between shear velocity and

bulk sound in the lower mantle, extending to a depth of 1500 km, although the extent of negative correlation above the base of the mantle is strongly dependent on harmonic degree. This negative correlation implies the presence of phase change or chemical heterogeneity in the lower mantle. The depth extent of the negative correlation between shear velocity and bulk sound speed for the two direct inversions is clearly dependent on earthquake location. Both models exhibit negative correlation at the base of the mantle. However, whereas the bulk sound speed model made with the new locations shows a negative correlation in only the lowermost mantle, the models made with the EHB locations are negatively correlated up to the transition zone. The effects of earthquake location on correlation are seen most strongly at low harmonic degrees, where the depth extent of negative correlation changes the most. The use of different earthquake locations may explain why the depth at which anti-correlation of shear velocity and bulk sound speed starts varies so much in previous studies.

## 4.4 Conclusions

One of the most interesting features at the base of the mantle is the negative correlation of shear velocity and bulk sound speed, which implies the presence of chemical or phase heterogeneity. Our knowledge of the spatial extent of the negative correlation, however, has been hampered by poor coverage at the base of the mantle and the lack of good bulk sound speed models. To get a better idea of the constraint on bulk sound speed, we create bulk sound speed residuals by combining S and P travel times for common-source receiver pairs, which we can then directly invert for bulk sound speed.

Using our new technique, we created a data set of approximately 93,000 bulk sound speed residuals by combining our S and P, Sdiff and Pdiff, and SS-S and PP-P travel times. To examine the effects of earthquake location on correlation, we created two additional data sets of bulk sound speed residuals using the EHB locations and the EHB locations corrected for finite frequency effects.

Plots of residuals at their turning points show that coverage is fairly good at

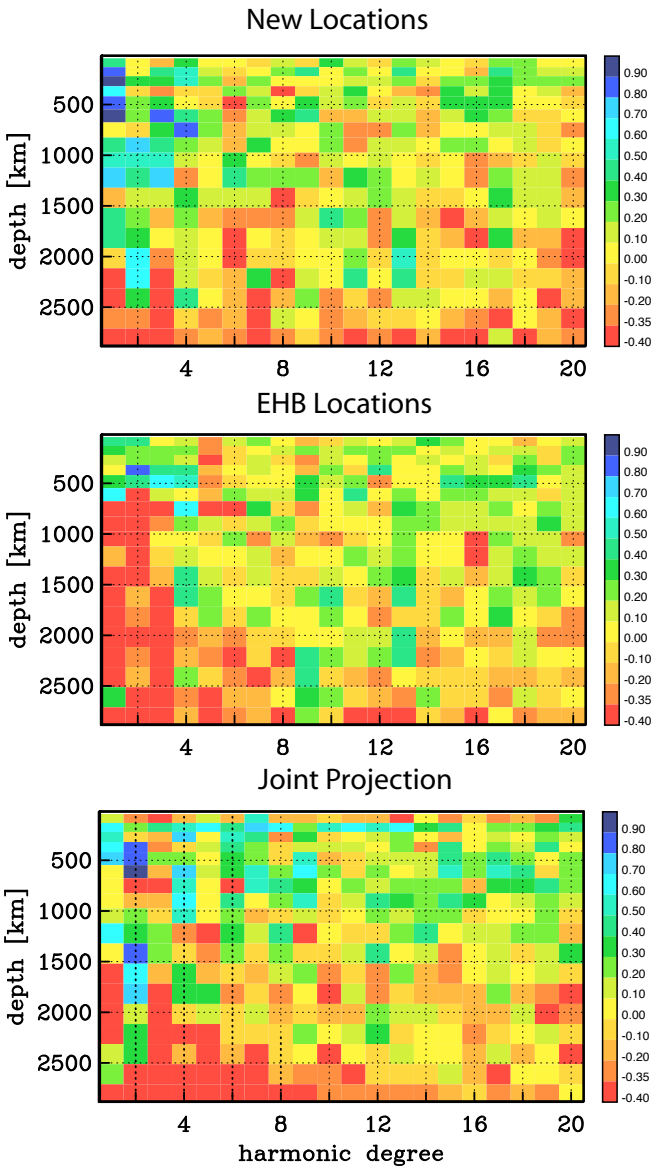


**Figure 4.10**: Correlation between shear velocity and bulk sound speed as a function of depth and harmonic degree for our three models. The top plot shows the correlation of our direct inversion using our new locations. The middle from the top shows the correlation of our direct inversion using the EHB locations. The bottom plot shows the correlation for our jointly inverted model.

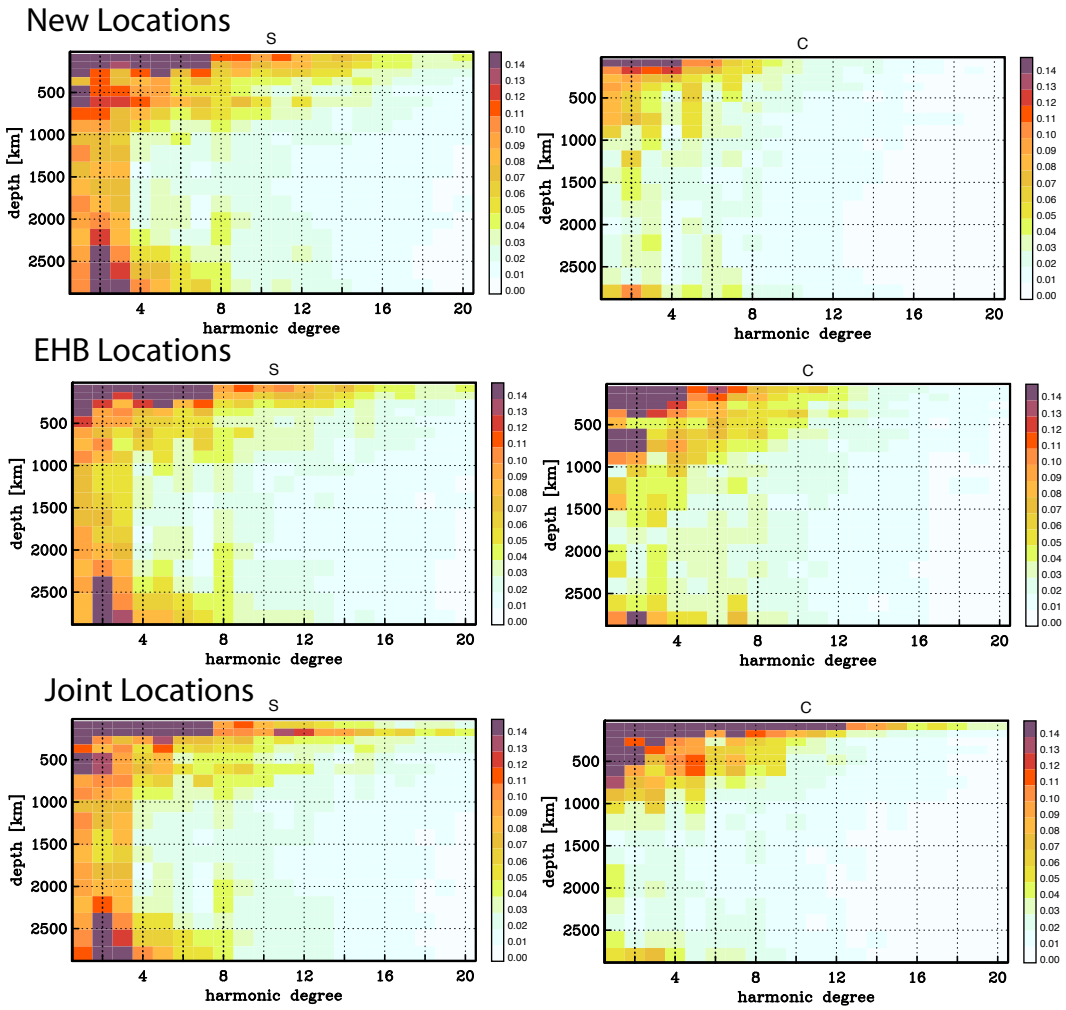


**Figure 4.11**: Amplitudes as a function of a depth and harmonic degree for all three sets of S and bulk sound speed models. The top plots show the amplitudes for the models made with the new locations. The middle plots show the amplitudes of the models made using the EHB locations. The bottom plots show the amplitudes of the joint projection.

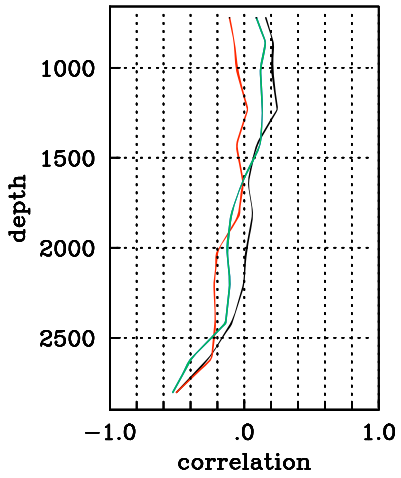


**Figure 4.12**: Overall correlation of shear velocity with bulk sound speed as a function of depth for the lower mantle, for the models made using the new locations (black), the EHB locations (red) and the joint inversion (green).

the base of the mantle, with most of the Northern Hemisphere and some of the Southern Hemisphere sampled. As depth decreases, coverage gets worse, with large parts of the Southern Hemisphere remaining entirely unsampled. Plotting the residuals at their turning points also allows us to see the signal in our data. All three data sets show regions of fast bulk sound speed underneath the Pacific and Africa at the base of the mantle, exhibiting the pattern of negative correlation between shear velocity and bulk sound speed seen in earlier studies. At shallower depths, the pattern changes, depending on the locations used, with the residuals made using the EHB locations remaining negatively correlated with shear velocity to much shallower depths. This same trend is seen in scatterplots of the S residuals versus bulk sound speed residuals. The change in results depending on earthquake location demonstrates that one should not use short-period earthquake locations for long period data, because the offset in origin time adds a significant signal.

We inverted the bulk sound speed residuals made using the new locations. The resulting model is similar to existing bulk sound speed models at the base of the mantle, with fast regions underneath the Pacific and Africa, surrounded by regions of slow velocity. Due to limited sampling in the Southern Hemisphere, resolution is only good in the Northern Hemisphere throughout the lower mantle. At present, there is not

enough data to clearly constrain the bulk sound speed pattern using bulk sound speed residuals, making this model unreliable. However, as the data set grows, this technique should become more useful.

We also simultaneously inverted for shear velocity and bulk sound speed, using projected data, which are insensitive to location. Since the joint inversion does not require matching S and P pairs, we are able to use our entire data set in the inversion, which is significantly larger and provides much better coverage of the mantle. Consequently, resolution is much better in the joint inversion, making this model more reliable. The better resolution also gives us a much stronger constraint on the correlation between shear velocity and bulk sound speed. In the joint inversion, shear velocity and bulk sound speed are negatively correlated to a depth of approximately 2000 km, indicating the presence of chemical or phase heterogeneity in the bottom 800 km of the mantle.

## 4.5 Acknowledgements

Chapter 4 (Manners, U.J. and G. Masters (2008), Relations between shear velocity and bulk sound speed.) has been submitted in full for publication in *Geophysical Journal International*. The dissertation author was the primary investigator and author of this paper.

# 5

# Modeling the lowermost mantle using diffracted phases and finite frequency kernels

**Abstract**

We present the results of inversions using ray theory and finite frequency kernels for a new data set of long period Sdiff and Pdiff travel time measurements. Finite frequency kernels for diffracted phases are quite different from ray theory kernels and have increased sensitivity to structure at depths well above the CMB. Shear velocity models derived from our data are very similar, with the finite frequency model showing larger amplitudes at the base of the mantle. Compressional velocity models display greater differences in the lower mantle, particularly at shorter wavelengths. To model bulk sound speed, we jointly inverted for shear velocity and bulk sound speed. Bulk sound speed is anti-correlated with shear velocity over most of the base of the mantle, starting at a depth of 2000 km, confirming the results of previous studies. This anti-correlation suggests the presence of chemical or phase heterogeneity at the base of the mantle.

## 5.1 Introduction

Measurements of seismic travel times have been the basis of the study of the velocity structure of the Earth. Up until recently, tomographic models of the Earth

have been made by applying ray theory to travel times (e.g. Su and Dziewonski, 1997; Ritsema et al., 1999; Masters et al., 2000; Antolik et al., 2003; Li et al., 2006; Simmons et al., 2006; Houser et al., 2008). Recent advances, however, have allowed tomographic models to be made using finite frequency kernels (e.g. Montelli et al., 2004a, 2006; Zhou et al., 2006), which take into account the frequency dependence of travel times and the effects of wavefront healing.

Ray theory assumes that seismic waves propagate through the Earth as rays, which are sensitive to structure only along the ray path. The travel time of the ray is dependent solely on the speed of the wave between the source and the receiver, with changes in arrival time occurring when a ray passes through a velocity anomaly. Ray theory, however, does not take into account the sensitivity of travel times to structure off the ray path. The size of the sensitivity kernel is a function of wavelength and epicentral distance and, for simple waves like S and P, is shaped like a banana (Nolet et al., 2005). Additionally, and in contrast to ray theory, sensitivity to structure along the ray path itself is zero for finite frequency kernels, hence the name "banana-doughnut kernels" (Nolet and Dahlen, 2000). Another effect that ray theory does not consider is wavefront healing, in which diffraction acts to fill in irregularities in the wavefront. As a result of wavefront healing, travel time delays diminish with distance travelled. Diffraction effects can also distort the waveform, which is a potentially important effect for travel times measured by waveform cross-correlation (Nolet et al., 2005).

Several studies have now used finite frequency kernels in global tomographic models (e.g. Zhou et al., 2006; Montelli et al., 2004a,b, 2006). Zhou et al. (2006) applied 3D finite frequency kernels to the surface wave dispersion measurements of Laske and Masters (1996). Montelli et al. (2004a) used the P and PP-P travel times data sets of Bolton and Masters (2001) to model compressional velocity in the mantle. Updated compressional and shear velocity models were presented in Montelli et al. (2006). In a comparison of finite frequency and ray theoretical models, Montelli et al. (2004b) found that ray-theoretical models underestimate amplitudes, particularly of short wavelength velocity anomalies. While recent studies have examined the importance of finite

frequency kernels for surface wave measurements and body waves, finite frequency kernels, as yet, have not been applied to diffracted phases in global tomographic models. Diffracted waves are ideally suited to studies of the base of the mantle, because they spend a significant portion of their ray path along the CMB.

Studies of the base of the mantle have also examined the correlation between shear velocity, $v_s$, and bulk sound speed, $v_c$, which is defined as:

$$v_c = \sqrt{\frac{K_s}{\rho}} = \sqrt{{v_p}^2 - \frac{4}{3}{v_s}^2} \tag{5.1}$$

Whereas shear velocity is sensitive to only the shear modulus, compressional velocity is sensitive to both the shear and bulk modulus. Thus, using bulk sound speed, which is only sensitive to the bulk modulus, allows us to isolate the effects of compression. Studying the relative variations in shear velocity and bulk sound speed allow us to determine the physical cause of a velocity anomaly. Previous studies (e.g. Su and Dziewonski, 1997; Masters et al., 2000; Antolik et al., 2003) have found that shear velocity and bulk sound speed are negatively correlated in the lower mantle, implying the presence of chemical or phase heterogeneity. The depth extent of this negative correlation, however, is not well constrained and could be potentially affected by the use of ray theory versus finite frequency kernels.

## 5.2 Method

### 5.2.1 Data

Our diffracted data set consists of approximately 35,000 Pdiff and 27,000 Sdiff measurements, picked using cluster analysis, for events occurring between 1986 and 2005. The measurements were made on long period data, with a dominant period of 20 s. Details of the measurement technique can be found in Manners and Masters (2008b).

To constrain structure in the upper and mid-mantle, we include pre-existing data sets of absolute and differential long period body wave travel times (see Table 5.1). The data sets include P, PP-P, S, SS-S, and ScS-S data sets, which were measured manu-

ally or using cluster analysis (Houser et al., 2008), as well as pP-P and sS-S travel times (Manners and Masters, 2008a). We also include a data set of surface wave dispersion measurements to better constrain upper mantle structure (Masters et al., 2000, *Laske*, personal communication). The effects of crustal thickness variations are removed using CRUST 2.0 (Bassin et al., 2000) and the data are corrected for the Earth's ellipticity (Kennett and Gudmundsson, 1996). Data are weighted by their errors during inversion, so that better quality measurements receive more weight.

**Table 5.1**: Phases and number of measurements included in study

| Phase | Number of Picks | Years |
|---|---|---|
| P | 182724 | 1976 - 2005 |
| Pdiff | 34774 | 1986 - 2005 |
| PP-P | 26116 | 1976 - 1999 |
| S | 169832 | 1976 - 2005 |
| Sdiff | 26706 | 1986 - 2005 |
| SS-S | 32266 | 1976 - 1999 |
| ScS-S | 26840 | 1976 - 2005 |
| pP-P | 23184 | 1976 - 2005 |
| sP-P | 26615 | 1976 - 2005 |
| sS-S | 30223 | 1976 - 2005 |

### 5.2.2 Locations

Location error is a large source of error in our data sets and cannot be ignored, since the error is similar in size to the signal from 3D structure for our P data (Bolton and Masters, 2001). We deal with location error by jointly inverting for structure and velocity (Manners and Masters, 2008a), as given by:

$$\delta \mathbf{t} = \begin{bmatrix} \lambda \mathbf{A} & \mathbf{B} \end{bmatrix} \begin{bmatrix} \lambda^{-1} \delta \mathbf{h} \\ \delta \mathbf{v} \end{bmatrix} \tag{5.2}$$

where $\mathbf{A}$ is a matrix containing the travel time derivatives with respect to location, $\delta \mathbf{h}$ is a vector representing the perturbation in location and origin time, $\mathbf{B}$ is the matrix of velocity derivatives, and $\delta \mathbf{v}$ is a vector representing the 3D perturbations in velocity. Ray paths are calculated relative to ak135 (Kennett et al., 1995). A detailed investigation of

the trade-offs between structure and locations is given in Manners and Masters (2008a). We use their preferred locations in the rest of this paper.

### 5.2.3 Inversions

The following sections describe our inversions. Models are parameterized by 18 layers, that are 100 km thick in the upper mantle and 200 km thick in the lower mantle. Each layer is divided into $4^\circ$ equal area blocks, resulting in a total of 46,404 model parameters.

#### S and P Inversions

In our inversions, we minimize:

$$(\mathbf{B}\delta\mathbf{v} - \delta\mathbf{t})^{\mathbf{2}} + \lambda^{\mathbf{2}}(\mathbf{S}\delta\mathbf{v})^{\mathbf{2}} \tag{5.3}$$

where $\mathbf{B}$ is a matrix velocity derivatives, $\delta\mathbf{v}$ is the model, $\delta\mathbf{t}$ is the data, and $\mathbf{S}$ is the roughness matrix given, in our case, by a first difference nearest neighbor operator. This leads to the set of equations:

$$\begin{bmatrix} \mathbf{B} \\ \lambda\mathbf{S} \end{bmatrix} \begin{bmatrix} \delta\mathbf{v} \\ 0 \end{bmatrix} = \begin{bmatrix} \delta\mathbf{t} \\ 0 \end{bmatrix} \tag{5.4}$$

which are inverted using LSQR (Paige and Saunders, 1973). We use the P, Pdiff, PP-P, and pP-P data sets to make the P models and the S, Sdiff, SS-S, ScS-S, and sS-S data sets to make the S models. The ray theory models use ray theory kernels for all the data sets. In order to isolate the effects of the finite frequency kernels for the diffracted data, we use finite frequency kernels for the Pdiff and Sdiff data sets in the finite frequency models and use ray theory kernels for the remaining data sets. Since our library of Sdiff finite frequency kernels is not complete, our Sdiff data set for the models made using finite frequency kernels is smaller, consisting of approximately 17,000 measurements.

The strength of the smoothing is determined by weighing the roughness, *R*, of the model versus the $\chi^2$ fit of the model to the data. The roughness is given by:

$$R = \delta\mathbf{v}^{\mathbf{T}} \cdot \mathbf{S}^{\mathbf{T}} \cdot \mathbf{S} \cdot \delta\mathbf{v} \tag{5.5}$$

where $\mathbf{S}$ is the roughness matrix and $\delta\mathbf{v}$ is the model. To emphasize the effect of the finite frequency kernels, we calculate the roughness of only the bottom three layers of the mantle, since they are most affected by the inclusion of finite frequency kernels.

**Joint Inversion**

Since we are ultimately interested in investigating how using finite frequency theory affects the spatial extent of the negative correlation between shear velocity and bulk sound speed in the mantle, we do a joint inversion for shear velocity and bulk sound speed, solving the following set of equations:

$$\begin{bmatrix} \delta\mathbf{t_p} \\ \delta\mathbf{t_s} \end{bmatrix} = \begin{bmatrix} x\mathbf{B_p} & (1-x)\mathbf{B_p} \\ \mathbf{B_s} & 0 \end{bmatrix} \begin{bmatrix} \delta\mathbf{v_s} \\ \delta\mathbf{v_c} \end{bmatrix} \tag{5.6}$$

where $x = \frac{4}{3}(\frac{{v_s}^2}{{v_p}^2}) \approx 0.4$. We solve for the relative perturbation in velocity, such that $\delta\mathbf{v_s} = \frac{\delta v_s}{v_s}$ and $\delta\mathbf{v_c} = \frac{\delta v_c}{v_c}$. The perturbation in P velocity, $\delta v_p$, is given by:

$$\frac{\delta v_p}{v_p} = (1-x)\frac{\delta v_c}{v_c} + x\frac{\delta v_s}{v_s} \tag{5.7}$$

Due to computational limitations, we are restricted to using the P, Pdiff, PP-P, S, Sdiff, SS-S, and ScS-S data sets in this inversion.

## 5.3 Pdiff and Sdiff finite-frequency sensitivity kernels

Because of its diffracted nature, the Pdiff phase generally has a lower frequency content compared to the direct P phase, and when measured at periods of 20 seconds and longer has significant finite-frequency sensitivity to compressional-wave speed in the mantle. Recent studies demonstrate that the sensitivity of the Pdiff phase not only follows the raypath, but also has an elliptical-shaped footprint on the CMB with a major axis comparable in length to the diffracted portion of the Pdiff raypath along the CMB (Zhao et al., 2000; Zhao and Jordan, 2006; Liu and Tromp, 2008). Therefore, in order to more accurately interpret Pdiff traveltime measurements, we need to take into account this finite-frequency effect and use 3D sensitivity kernels instead of simple geometrical ray paths in global tomographic inversions.

### 5.3.1 Computation of finite-frequency kernels based upon adjoint methods

The calculation of Pdiff kernels using ray-based methods (e.g. banana-doughnut kernels, Dahlen et al., 2000; Hung et al., 2000) is challenging due to the diffracted nature of the phase, which leads to a fractional frequency dependence (e.g. Aki and Richards, 1980). The only available techniques to compute these sensitivity kernels for a 1D reference Earth model are normal-mode based methods (e.g. Zhao et al., 2000; Zhao and Jordan, 2006) and adjoint methods based upon 2D (e.g. Nissen-Meyer et al., 2007, 2008) or 3D numerical simulations (e.g. Liu and Tromp, 2006, 2008). For a fully 3D reference model, the adjoint method is the only available tool for computing finite-frequency kernels. In this article, we choose the adjoint approach to build a Pdiff kernel library for 1D reference model AK135 at various epicentral distances and source depths, and interpolate kernels from this library to obtain finite-frequency sensitivity kernels for specific Pdiff measurements.

In the adjoint method, a particular traveltime measurement $\delta T$ may be related to relative structural perturbations in density $\delta \ln \rho$, shear modulus $\delta \ln \mu$, and bulk modulus $\delta \ln \kappa$, or, alternatively, density $\delta \ln \rho$, shear-wave speed $\delta \ln \beta$, and compressional-wave speed $\delta \ln \alpha$ through the corresponding finite-frequency sensitivity kernels:

$$\delta T = \int_V (\delta \ln \rho K_\rho + \delta \ln \mu K_\mu + \delta \ln \kappa K_\kappa) \, \mathrm{d}^3\mathbf{r} \tag{5.8}$$

$$= \int_V (\delta \ln \rho K'_\rho + \delta \ln \beta K_\beta + \delta \ln \alpha K_\alpha) \, \mathrm{d}^3\mathbf{r}. \tag{5.9}$$

The kernels $K_\rho$, $K_\mu$, and $K_\kappa$, or $K'_\rho$, $K_\beta$, and $K_\alpha$ can be expressed as the interaction of the regular forward wavefield $\mathbf{s}$ and the so-called 'adjoint' wavefield $\mathbf{s}^\dagger$, which is generated by injecting the time-reversed forward synthetic velocity seismograms at the receivers as sources. For simplicity, we examine only the sensitivity kernels for the bulk modulus: other kernels may be found in Tromp et al. (2005). We have

$$K_\kappa(\mathbf{r}) = -\int_0^T \kappa(\mathbf{r})[\nabla \cdot \mathbf{s}(\mathbf{r}, T-t)][\nabla \cdot \mathbf{s}^\dagger(\mathbf{r}, t)] \, \mathrm{d}t, \tag{5.10}$$

where $T$ denotes the record length. All other kernels may be calculated similarly. We

compute both the forward wavefield $\mathbf{s}$ and the adjoint wavefield $\mathbf{s}^\dagger$ based upon 3D spectral-element (SEM) simulations (e.g. Komatitsch and Tromp, 2002a,b). Note that SEM finite-frequency sensitivity kernels for 3D reference models may be calculated for the same numerical cost as for 1D reference models. A typical computation of a Pdiff kernel accurate down to $20$ s takes approximately $2.6$ hours on $48$ nodes of the Dell cluster CITerra (http://citerra.gps.caltech.edu/). Each node has $12$ GB of memory and two Intel Quad Core $2.33$ GHz Clovertown processors. More details regarding the adjoint approach and its practical implementations are discussed in Tromp et al. (2005) and Liu and Tromp (2006, 2008). Figure 5.1 illustrates an example of a Pdiff sensitivity kernel at an epicentral distance of $103^\circ$ and an azimuth of $64^\circ$ from the hypocenter of the June 9, 1994, Bolivia earthquake. Notice that it looks almost like a typical banana-doughnut kernel, but has been cut through at the bottom by the CMB, leaving an elliptical-shaped footprint, and indicating significant sensitivity away from the diffracted portion of the raypath. Also note that these kernels can be sensitive to regions more than $500$ km above the CMB, and therefore may result in significantly different structural images close to the CMB compared to those based upon ray theory.

We average sensitivity kernels calculated based upon the SEM code onto a $4^\circ \times 4^\circ$ block model, which may be used directly as the input matrices for global tomographic inversions. We define the average of $K_\kappa(\mathbf{r})$ onto the $b$th block model as

$$K_\kappa^b = \int_{V_b} K_\kappa(\mathbf{r})\, \mathrm{d}^3\mathbf{r}, \tag{5.11}$$

such that the traveltime anomaly under uniform perturbations ($\delta \ln \kappa = \text{const.}$) is preserved:

$$\sum_b K_\kappa^b = \int_V K_\kappa(\mathbf{r})\, \mathrm{d}^3\mathbf{r}. \tag{5.12}$$

### 5.3.2 Effect of the source radiation pattern

The effect of the earthquake source mechanism on finite-frequency sensitivity kernels for cross-correlation traveltime measurements has been studied by Zhao and

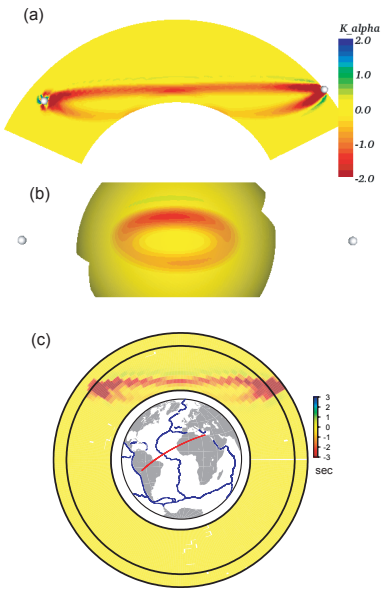


**Figure 5.1**: (a) Source-receiver cross-section of a 20 s $K_\alpha$ kernel for the Pdiff phase recorded at an epicentral distance of $103°$. (b) Map view on the CMB of the same kernel as in (a). (c) Resampling of the same kernel by a $4° \times 4°$ block model.

Jordan (2006) and Liu and Tromp (2008), and is illustrated in Figures 5.1(a) and (b). In general, the elliptical-shaped footprint on the CMB is asymmetric with respect to the source-receiver plane (Figure 5.1b), and the radiation pattern can be clearly identified close to the source (Figure 5.1a). This is readily explained by examining kernel expressions such as ( 5.10). Kernel calculations involve the interaction between the forward wavefield $\mathbf{s}$, which is affected by the radiation pattern of the earthquake, and the adjoint wavefield $\mathbf{s}^\dagger$, which involves the radiation pattern generated by a (vertical) point force exerted at the receiver. Thus, the kernel value at any given point in space will be determined by a combination of these two factors.

It is possible to take into account the effect of the source radiation pattern and build up a complete Pdiff kernel library from which a Pdiff kernel for any given source mechanism can be interpolated. Since the forward wavefield $\mathbf{s}$ for any given moment-tensor source $\mathbf{M}$ can be expressed as a combination of the individual Green's function $\mathbf{s}^{ij}(\mathbf{r}, \mathbf{r}_s; t)$ for each moment-tensor element $M_{ij}$:

$$\mathbf{s}(\mathbf{r}, t) = \sum_{ij} M_{ij} \mathbf{s}^{ij}(\mathbf{r}, \mathbf{r}_s; t), \tag{5.13}$$

and the adjoint wavefield $\mathbf{s}^\dagger$ is generated by convolving the 'adjoint' source-time function $f^\dagger(\mathbf{r}_r, t)$ with the Green's function $\mathbf{s}^r(\mathbf{r}, \mathbf{r}_r; t)$ for a vertical point force at the receiver $\mathbf{r}_r$:

$$\mathbf{s}^\dagger(\mathbf{r}, t) = f^\dagger(\mathbf{r}_r, t) * \mathbf{s}^r(\mathbf{r}, \mathbf{r}_r; t). \tag{5.14}$$

The adjoint source is a synthetic vertical-component velocity pulse, time-reversed and windowed around a specific phase of interest, i.e. Pdiff:

$$f^\dagger(\mathbf{r}_r, t) = \frac{1}{N_r} \sum_{kl} M_{kl} [w_r(T-t) \dot{s}_r^{kl}(\mathbf{r}_r, T-t)]. \tag{5.15}$$

where

$$N_r = \int_0^T w_r(t) s_r(\mathbf{r}_r, t) \ddot{s}_r(\mathbf{r}_r, t)\, \mathrm{d}t. \tag{5.16}$$

Here $w_r(t)$ is the time-windowing function and $*$ denotes time convolution. Substituting equations ( 5.13) and ( 5.14) into the kernel expression ( 5.10), and defining the adjoint

wavefield associated with $M_{kl}$ as

$$\mathbf{s}^{kl\dagger}(\mathbf{r},\mathbf{r}_r;t) = [w_r(T-t)\dot{s}_r^{kl}(\mathbf{r}_r,T-t)] * \mathbf{s}^r(\mathbf{r},\mathbf{r}_r;\tau), \tag{5.17}$$

we obtain

$$K_\kappa(\mathbf{r}) = \frac{1}{N_r}\sum_{ij;kl} M_{ij}M_{kl}\int_0^T \kappa(\mathbf{r})[\nabla\cdot\mathbf{s}^{ij}(\mathbf{r},\mathbf{r}_s;T-t)][\nabla\cdot\mathbf{s}^{kl\dagger}(\mathbf{r},\mathbf{r}_r;t)]\,\mathrm{d}t. \tag{5.18}$$

Note that as a result of the normalization factor $N_r$, this kernel is independent of the scalar moment.

To calculate Pdiff kernels for an arbitrary source mechanism, we need to compute and store one 'sub-kernel' for each pair of $ij$ and $kl$, which leads to a total of $6\times 6 = 36$ kernel simulations. This poses a formidable computation and storage challenge.

### 5.3.3 Pdiff library for explosive sources

We circumvent the kernel storage-CPU-time challenge by computing Pdiff kernels for an explosive source, which exhibits a symmetric pattern across the source-receiver plane on the CMB. To assess the impact in terms of the integrated traveltime anomaly, we consider the Pdiff kernel corresponding to a depth of $0$ km and a distance of $100^\circ$, and select $324$ random source locations on the earth's surface. For every source location, we evenly distribute $36$ receivers in all azimuths, which gives a total of $11664$ source-receiver pairs. We compute the difference between the synthetic traveltime predicted by the finite-frequency Pdiff kernels for a moment-tensor source (for the Bolivia earthquake) and for an explosive source ($M_{11}=M_{22}=M_{33}$, $M_{12}=M_{13}=M_{23}=0$) by integrating the kernels with respect to an actual 3D mantle P-velocity model:

$$\begin{aligned}\Delta T_{mt} &= \sum_b K_{mt}^b(\frac{\delta m}{m})_b \\ \Delta T_{ex} &= \sum_b K_{ex}^b(\frac{\delta m}{m})_b.\end{aligned} \tag{5.19}$$

Figure 5.2 shows a comparison of the resulting synthetic traveltimes.They generally agree very well, to within $\pm 0.5$ s, which is smaller than the measurement error for

these long-period Pdiff waves. In general, the radiation pattern introduces very small variations in the synthetic traveltime for relatively smooth mantle velocity models, and therefore this effect can be safely ignored. This is not surprising, since a straightforward ray-theoretical calculation of the cross-correlation traveltime anomaly is obviously independent of the source mechanism.

For the purpose of the tomographic inversions performed in this paper, we build a Pdiff kernel library for 1D reference model AK135. This library includes Pdiff kernels for stations in the epicentral distance range from $100°$–$140°$ and for earthquakes with a depth range from $0$ km–$700$ km. Figure 5.3 shows that the Pdiff kernel varies smoothly as a function of distance and therefore can be reliably interpolated to obtain Pdiff kernels for any particular distance. The same conclusion can be drawn for the variation and interpolation as a function of depth. In practice, we compute the kernels with distance intervals of $2°$ and depth intervals of $10$ km (for depths $\leq 60$ km, which includes the majority of events) and $20$ km (for depths $> 60$ km). For measurements corresponding to a particular epicentral distance and earthquake depth, we choose the nearest Pdiff kernel in the library to represent its sensitivity to compressional-wave speed structure, which introduces $\pm 0.1$ s errors in the traveltime residuals - far below the measurement errors for long-period Pdiff waves.

## 5.4 Results and Discussion

### 5.4.1 S and P Models

Before presenting the results of our inversions, we must discuss how we chose the roughness of our models. We ordinarily choose the smoothing parameters of our models by weighing the roughness of the model against the $\chi^2$ fit of the model to the data, ultimately looking for a model for which increased roughness does not significantly improve the fit of the model to the data. However, since we are comparing two different theories, we must also choose a finite frequency model that is comparable to our ray theory model, in some sense. One option is to choose models that have the same $\chi^2$ fit

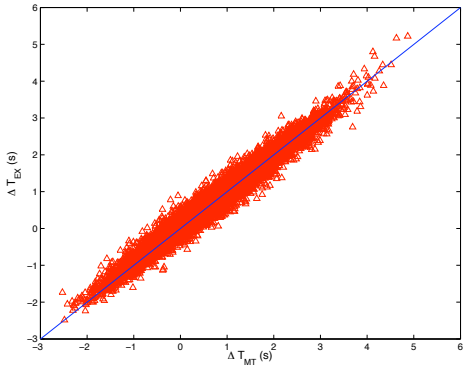


**Figure 5.2**: Comparison of Pdiff synthetic travel times for an explosive source and a moment-tensor source.

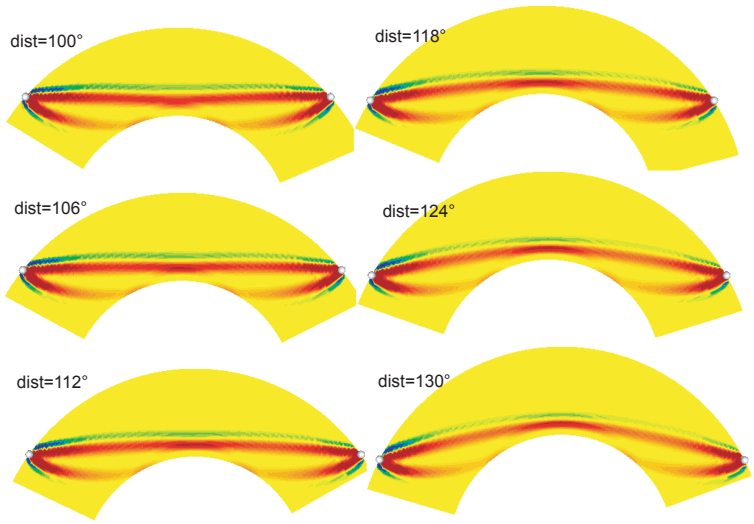


**Figure 5.3**: Variation of the Pdiff kernels as a function of distance for an earthquake on the surface.

to the data, as was done in Montelli et al. (e.g. 2004b). Figure 5.4 shows a plot of the $\chi^2$ fit of a suite of S models made using ray theory kernels and finite frequency kernels to the S, Sdiff, and ScS-S data sets. We note that the ray theory models fit the data better than the finite frequency models and that we are unable to increase the roughness of the models made using finite frequency kernels enough to obtain the same fit. Since we were unable to find models with the same fit to the data, we chose to use models with the same roughness, represented by the vertical line in Figure 5.4. This process was repeated for the P models, where we again found that we were unable to increase the roughness of the models made using finite frequency kernels to obtain the same fit to the data as the models made using ray theory kernels. Consequently, we also chose P models with the same roughness.

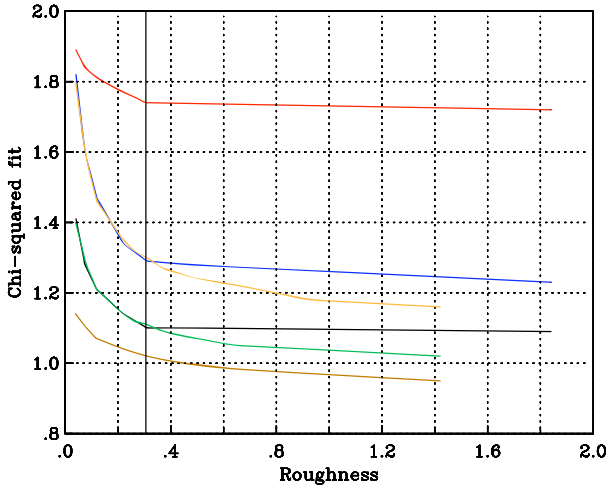


**Figure 5.4**: Trade-off curves for S models showing the $\chi^2/N$ fit as a function of model roughness. For the models made using finite frequency kernels, the curves show the fit of a range of models to the S (black), Sdiff (red) and ScS-S (blue) data. For the models made using ray theory kernels, the curves show the fit of a range of models to the S (green), Sdiff (brown) and ScS-S (yellow). The vertical black line shows the roughness of our chosen models. As a reminder, we are using finite frequency kernels for the diffracted data sets alone.

Figure 5.5 shows our S models made using ray theory and finite frequency kernels, for the bottom three layers of the mantle. The largest differences are in the

lowermost layer of the model, where the model made using finite frequency kernels exhibits much larger amplitudes. In looking at the fit of the models to the data, it is useful to examine how the fit changes depending on the theory used. As discussed earlier, the fit of the ray theory model with the ray theory kernels for the Sdiff data is better, with a $\chi^2$ fit of 1.02, as opposed to 1.74 for the finite frequency model with the finite frequency kernels. If we switch models and kernels for the Sdiff data, we find that the fit of the ray theory model with the finite frequency kernels is 2.39, whereas it is 1.57 for the finite frequency model with the ray theory kernels.

The results of our P inversions can be seen in Figure 5.6. In contrast to the S models, the differences between the finite frequency and ray theory models are much more apparent, affecting the shape of the velocity anomalies in the lowermost three layers of the model. Again, the ray theory model with the ray theory kernels is able to fit the Pdiff data better, with a $\chi^2$ fit of 1.17, as opposed to 1.39 for the finite frequency model with the finite frequency kernels. The fit of the ray theory model with the finite frequency kernels is 2.19 and the fit of the finite frequency model with the ray theory kernels is 2.03. This decreased fit probably reflects the large differences in structure that results from using finite frequency kernels, as opposed to ray theory kernels.

**Resolution and Errors**

To test resolution, we did a checkerboard resolution test, in which a checkerboard pattern for a single layer is used to make synthetic data with the same ray geometry as our existing data sets. The synthetic data are generated using ray theory for the ray theory model and finite frequency theory for the finite frequency model. The synthetic data are then inverted, allowing us to determine how well our data sets are able to resolve structure and amplitude. The results of the resolution tests can be seen in Figure 5.7 for the S models and Figure 5.8 for the P models. In general, the pattern and amplitudes are well resolved for all models in both hemispheres. Regions beneath Southern Africa are less well constrained, reflecting poorer coverage by the data sets. Models constructed using ray theory appear to be better resolved in the lower mantle.

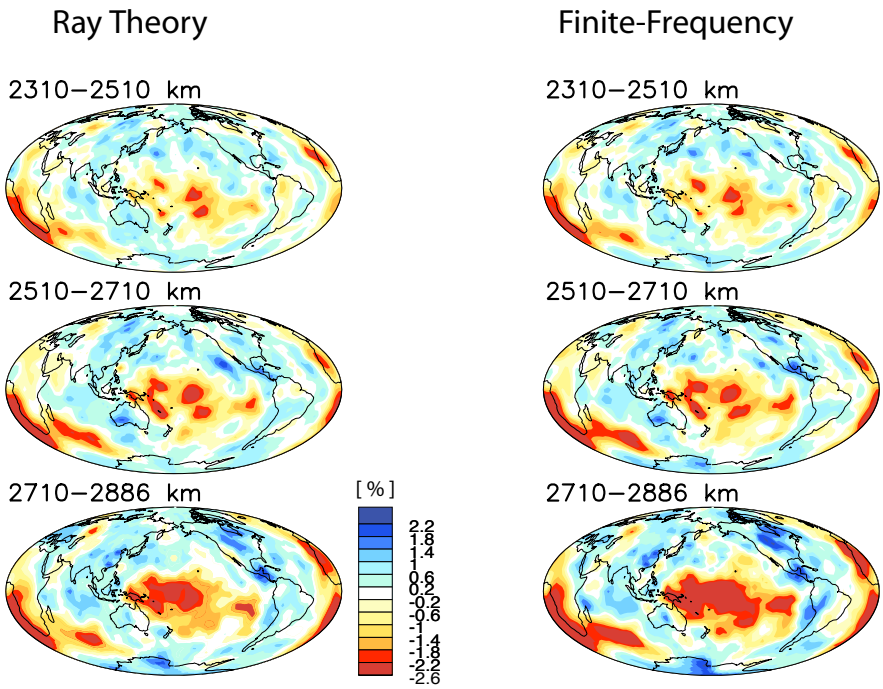


**Figure 5.5**: Slices of the bottom three layers of the mantle showing perturbation in shear velocity for our model made using ray theory kernels (left) and our model made using finite frequency kernels (right).

The finite frequency diffracted data sets, however, are somewhat smaller, since we do not have finite frequency kernels for all events, with the finite frequency Sdiff data set, in particular, having 8000 fewer measurements. Thus, the poorer constraint on structure may be a reflection of the reduced data set.

**Comparison of Models**

To compare the finite frequency and ray theory models, we correlate them as a function of depth and harmonic degree (Figures 5.9 and 5.10). For the S models, the correlation is high throughout the entire lower mantle, with small differences in correlation seen at high harmonic degrees at the base of the mantle. The ray theory and finite frequency P models exhibit greater differences, with correlations close to zero at the base of the mantle at high harmonic degrees. Unlike the S models, the amplitudes, however, are approximately the same in both models. Correlation is also lower above

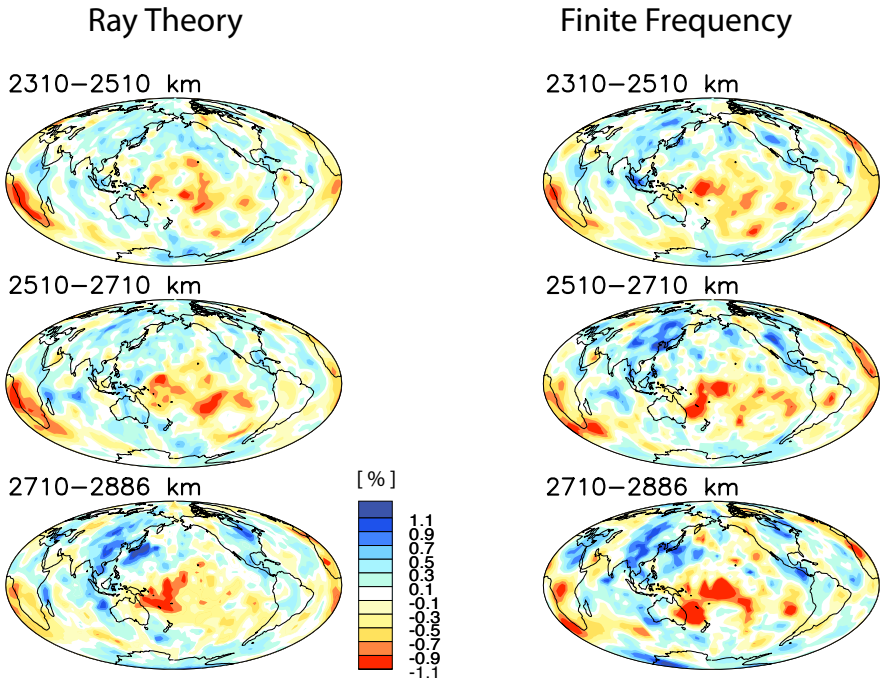


**Figure 5.6**: Slices of the bottom three layers of the mantle showing perturbation in compressional velocity for our ray theory model (left) and finite frequency model (right).

the base of the mantle, extending to a depth of approximately 2000 km. The larger differences between the P models may be a reflection of the relatively larger size of the P sensitivity kernels. For both the S and P models, finite frequency kernels do not appear to affect long wavelength structure as evidenced by the high correlation between the ray theory and finite frequency models at low harmonic degrees.

As another comparison of the models, we create synthetic Pdiff data for the ray theory and finite frequency theory, by dotting the respective matrices with a P model. The resulting synthetic travel time residuals are then plotted against each other. Figure 5.11 shows that the difference between ray theoretical and finite frequency times can be as much as two seconds for a typical 3D model, illustrating that the theories do predict different travel times.

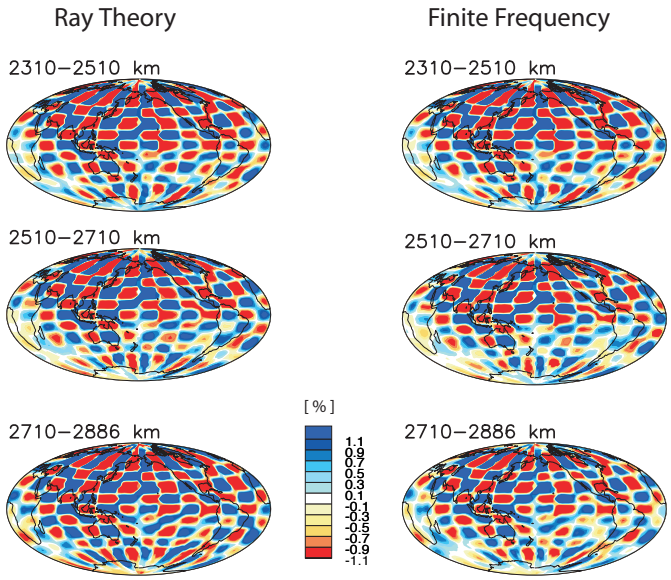


**Figure 5.7**: Slices of the bottom three layers of the mantle showing the results of the checkerboard resolution test for the ray theory (left) and finite frequency (right) S models.

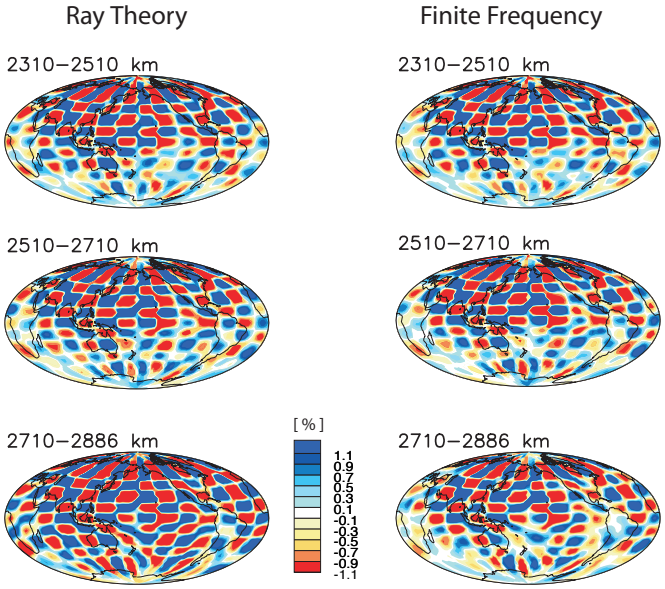


**Figure 5.8**: Slices of the bottom three layers of the mantle showing the results of the checkerboard resolution test for the ray theory (left) and finite frequency (right) P models.

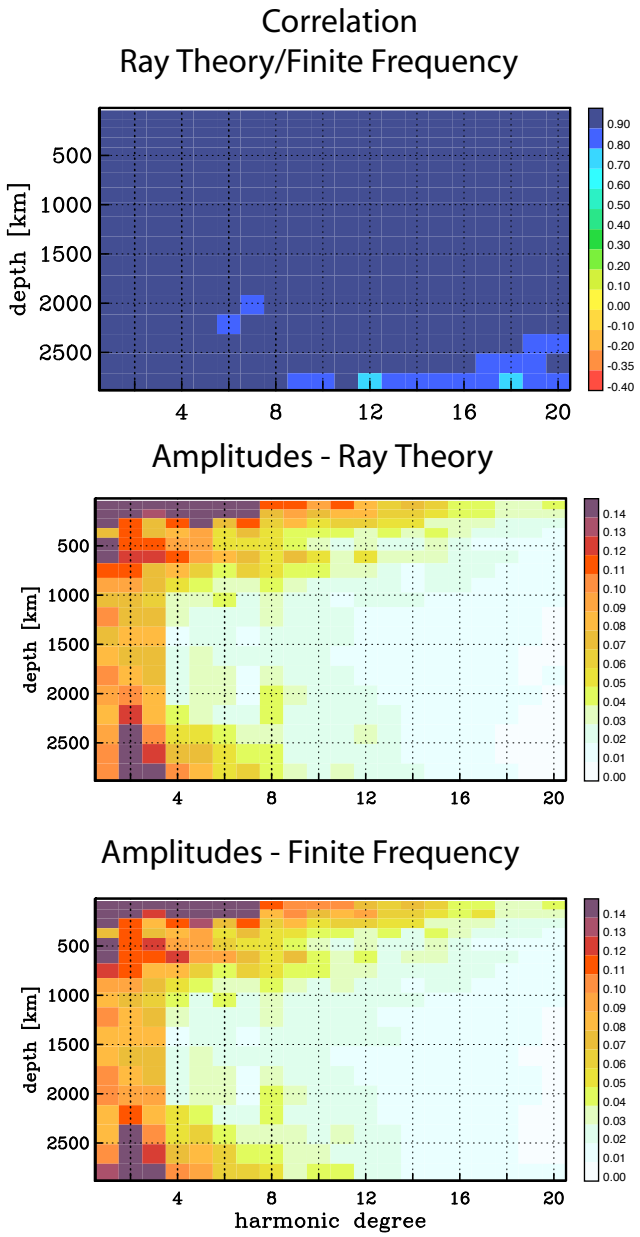


**Figure 5.9**: Correlation (top) as a function of depth and harmonic degree for our S models. The middle and bottom plots show the amplitudes of the ray theory and finite frequency models, respectively.

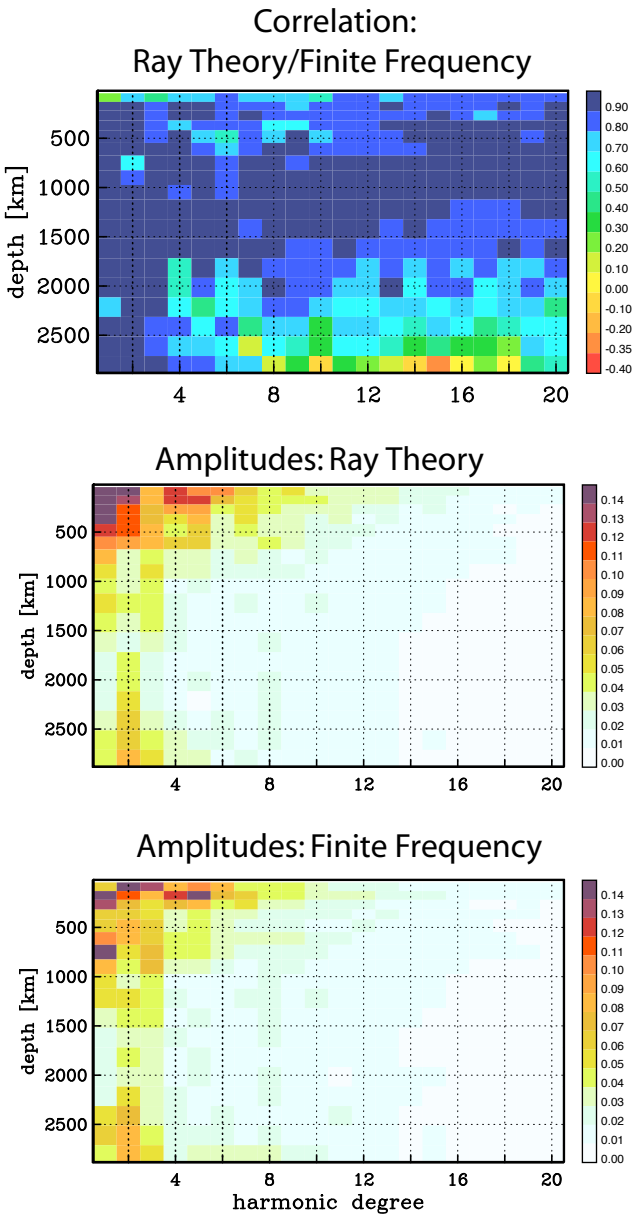


**Figure 5.10**: Correlation (top) as a function of depth and harmonic degree for our P models. The middle and bottom plots show the amplitudes of the ray theory and finite frequency models, respectively.

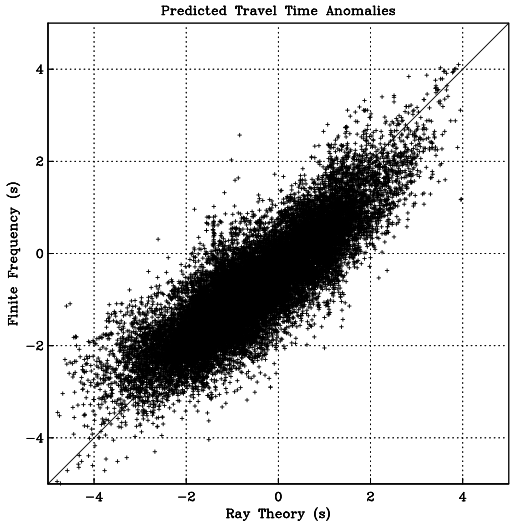


**Figure 5.11**: Pdiff travel time anomalies as predicted using ray theory and finite frequency kernels.

### 5.4.2 Joint Inversion

As discussed earlier, studying the relative variations in shear velocity and bulk sound speed allows one to determine the physical cause of velocity anomalies. Previous studies (e.g. Su and Dziewonski, 1997; Masters et al., 2000; Antolik et al., 2003) have determined that the lower mantle is negatively correlated between shear velocity and bulk sound speed, indicating the presence of chemical and/or phase heterogeneity. However, the depth extent of the anti-correlation is not well constrained. These studies modeled the lower mantle using ray theory, which does not account for the sensitivity of the wave to structure off of the ray path. Taking this sensitivity into account may change the pattern of anti-correlation at the base of the mantle and change the depth extent of the anti-correlation seen.

We modeled bulk sound speed by jointly inverting for shear velocity and bulk sound speed, using our finite frequency diffracted data sets, as well as the P, PP-P, S, SS-S, and ScS-S data sets. The results of the inversion can be seen in Figure 5.12. The pattern of anti-correlation seen in previous studies is apparent in the models, with the bulk sound speed model exhibiting fast velocity anomalies underneath the Pacific and

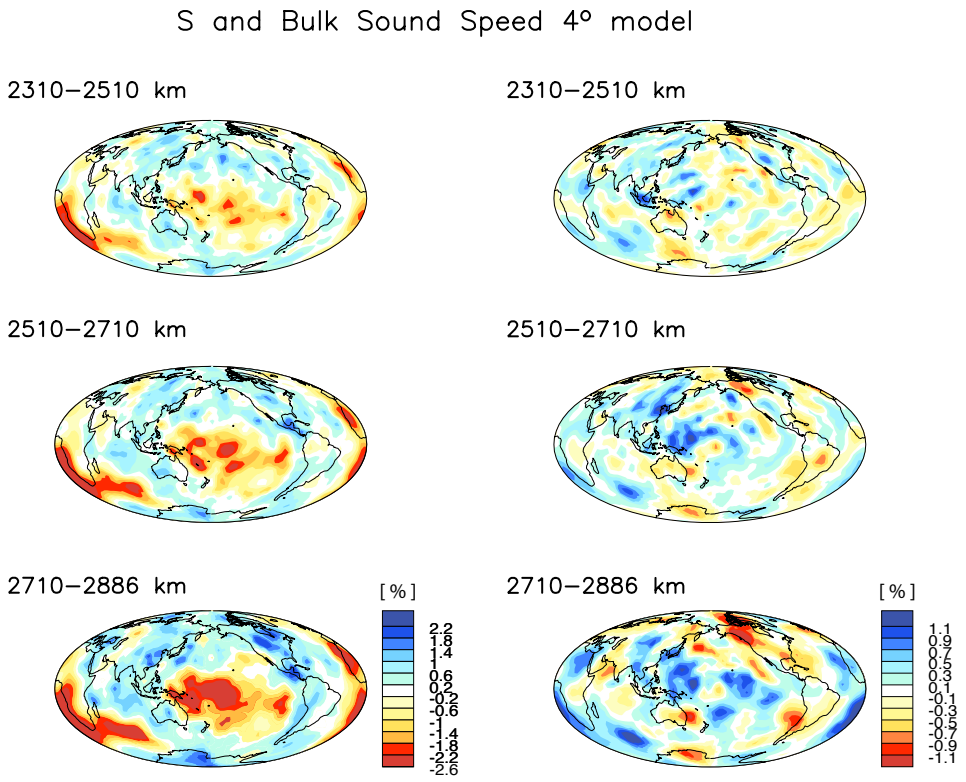


**Figure 5.12**: Slices of the bottom three layers of the mantle showing perturbation in shear velocity (left) and bulk sound speed (right).

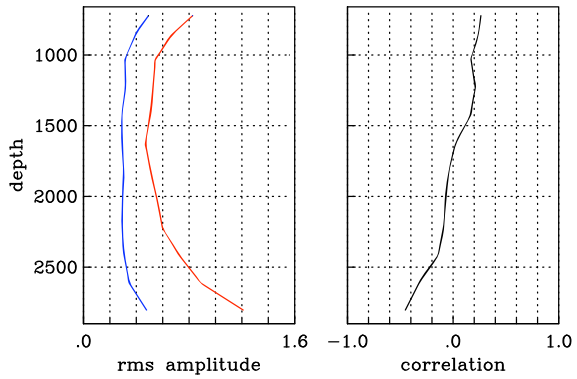


**Figure 5.13**: Amplitudes (left) of our shear (red) and bulk sound speed (blue) models. Correlation as a function of depth for the lower mantle is plotted on the right.

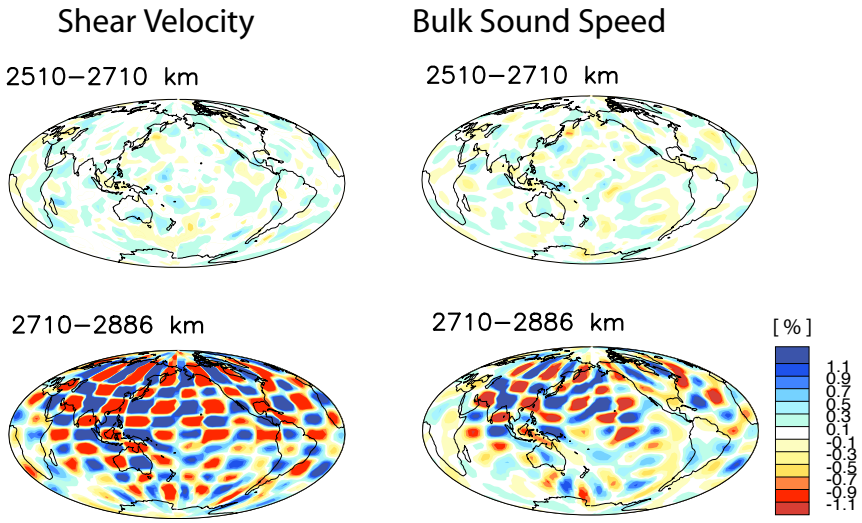


**Figure 5.14**: Slices of the base of the mantle showing the results of the checkerboard resolution test for the joint inversion, for shear velocity (left) and bulk sound speed (right). The layer above the base of the mantle shows how much leakage of structure there is into adjacent layers.

Africa, in contrast to the shear velocity model. To determine the fit of the bulk sound speed model to the data, we combined our shear velocity and bulk sound speed models to create a P model, using equation 7. The model fits the data well, with a $\chi^2$ fit of 1.23 and 1.51 for the P and Pdiff data sets, respectively. For the shear model, the $\chi^2$ fit is 1.73 and 1.65 for the S and Sdiff data sets, respectively. We examine the correlation between shear velocity and bulk sound speed by plotting the correlation as a function of depth (Figure 5.13). The models become negatively correlated at a depth of approximately 2000 km, confirming the results of Masters et al. (2000).

To test the resolution, we did a checkerboard resolution test, as described earlier (Figure 5.14). Resolution for the S model at the base of the mantle is good in both the Northern and Southern Hemisphere. For the bulk sound speed model, resolution is good in the Northern Hemisphere, but pattern recovery is poor in the Southern Hemisphere. Resolution in the Southern Hemisphere should improve when we are able to use our entire Sdiff and Pdiff data sets. Due to the sensitivity of finite frequency kernels to structure above the base of the mantle, models made using finite frequency kernels may

change the amount of leakage of structure into other layers. In comparing the results of checkerboard resolution tests for models made using ray theory kernels to models made using finite frequency kernels for the lowermost four layers of the mantle, we found that leakage into other layers is not affected by the use of finite frequency kernels in inversions. Consequently, the depth extent of the negative correlation between shear velocity and bulk sound speed should not be affected by sensitivity to structure above the base of the mantle.

## 5.5 Conclusions

We created shear and compressional velocity models of the lowermost mantle using finite frequency kernels for diffracted phases, and compared them to models made using ray theory kernels. The finite frequency kernels were constructed using the adjoint method. The finite frequency models are similar to the ray theory models, with the shear velocity models constructed using finite frequency kernels having larger amplitudes, particularly at the base of the mantle. Correlation plots show that the shear velocity models are very similar, with the largest differences occurring at the base of the mantle at short wavelengths. The compressional velocity models correlate less well, with lower correlation extending up higher into the lower mantle. Resolution tests show that the models constructed using ray theory kernels resolve structure at the base of the mantle better, although this may simply be a reflection of the smaller finite frequency data sets, since we currently do not have a complete library of finite frequency kernels.

We modeled bulk sound speed by jointly inverting for shear velocity and bulk sound speed using the finite frequency diffracted data sets. The resulting model is similar to existing models. Resolution at the base of the mantle is good in the Northern Hemisphere, but poor in the Southern Hemisphere. The use of finite frequency kernels does not change the amount of leakage of structure into other layers.

The negative correlation between shear velocity and bulk sound speed starts at a depth of approximately 2000 km, indicating the presence of chemical or phase

heterogeneity over a large part of the lower mantle. The cause of the chemical or phase heterogeneity implied by the anti-correlation is unknown at this time. The recent discovery of the phase transition from perovskite to post-perovskite (Murakami et al., 2004; Oganov and Ono, 2004) has been proposed as a possible source of phase heterogeneity, however, this is unlikely to be the cause of our observations. First principles calculations predict a 2-4% increase in shear velocity and a $\pm 0.5\%$ change in compressional velocity (Tsuchiya et al., 2004; Stackhouse et al., 2005; Wentzcovitch et al., 2006), implying that the increase in shear modulus is much larger than the increase in bulk modulus. Furthermore, the phase transition is strongly temperature dependent and may not even occur in hotter regions of the lowermost mantle (e.g. Wookey et al., 2005). Our models, however, show an increase in bulk sound speed and a corresponding decrease in shear velocity in the large slow shear velocity anomalies underneath the Pacific and Africa, which is the opposite of what is predicted. Wookey et al. (2005) suggests that since velocities in tomographic models are given relative to a global average at each depth, the velocity changes predicted by the phase transition to post-perovskite could result in anti-correlation between shear velocity and bulk sound speed. Houser (2007), however, found that a post-perovskite phase transition is unable to explain the observed relative variation between shear velocity and compressional velocity and that a chemical contribution is still necessary. Furthermore, although the depth extent of post-perovskite is not well constrained, the anti-correlation between shear velocity and bulk sound speed starts at much shallower depths than predicted for the post-perovksite phase transition (e.g. Murakami et al., 2005; Hirose et al., 2006; Hirose, 2007).

## 5.6 Acknowledgments

Chapter 5 (Manners, U.J., Q. Liu, G. Masters, and J. Tromp (2008), Modeling the lowermost mantle using diffracted phases and finite frequency kernels.) has been submitted in full for publication in *Geophysical Journal International*. The dissertation author was the primary investigator and author of this paper. We acknowledge support

by the Green Scholar Postdoctoral Fellowship in IGPP, UCSD and National Science foundation. The numerical simulations for this research were performed on the Caltech GPS Dell cluster.

# 6

# Conclusions

## 6.1 Conclusions

The core-mantle boundary is one of the most enigmatic regions of the Earth. Previous studies (e.g. Su and Dziewonski, 1997; Masters et al., 2000; Antolik et al., 2003; Ishii and Tromp, 2004) have observed a negative correlation between shear velocity and bulk sound speed in the lowermost mantle, indicating the presence of chemical and/or phase heterogeneity. The depth extent of the negative correlation, however, is not well constrained, due to poor coverage at the base of the mantle and sensitivity to earthquake location errors. To improve coverage at the base of the mantle, we created a data set of 27,000 Sdiff and 35,000 Pdiff travel time measurements, using cluster analysis, with the goal of improving the constraint on the depth and spatial extent of the anti-correlation between shear velocity and bulk sound speed.

Prior to inverting our travel time data sets, we investigated several methods of dealing with earthquake mislocation, since it is a large source of error in tomographic inversions. Tests on synthetic data show that both projection and joint inversions for hypocenter and velocity are able to correct for location error. Iterative relocation, however, only performs satisfactorily on 1D synthetic data. Iterative relocation, using 3D synthetic data, results in models that exhibit structures not seen in the original models, suggesting that iterative relocation is not a good approach to use on teleseismic data sets.

Using synthetic data, we also investigated the effects of different relocation methods on the correlation between shear velocity and bulk sound speed. We found that shear velocity and bulk sound speed models made using iterative relocation show lower correlations than models made using projection or a joint inversion for velocity and hypocenter. We also found that combining separate shear and compressional velocity models to create a bulk sound speed model is not a safe approach.

Tests using real data yielded good results for both the projected and jointly inverted data sets. Projection is probably the safest approach to dealing with location error, however, due to its computational expense, a joint inversion for velocity and hypocenter is a suitable substitute. Our earthquake relocations also benefitted from the inclusion of a new data set of depth phases, which improve the constraint on depth of deep earthquakes. The locations determined from our joint inversions show a systematic shift of earthquake hypocenter away from subduction zones, particularly in the Aleutians, which is expected.

We used our diffracted data sets to model the base of the mantle, using our new locations. Our new shear velocity model is similar to existing models, with improved definition of the slow regions underneath Africa and the Pacific. Our new compressional model correlates less well with existing models, with differences in both the shape and amplitudes of the large velocity anomalies underneath the Pacific and Africa. Resolution tests show that the inclusion of the diffracted data sets significantly improves resolution, particularly in the Southern Hemisphere. We also jointly inverted for shear velocity and bulk sound speed. The resulting models show the pattern of anti-correlation seen in previous studies.

We examined the correlation between shear velocity and bulk sound speed in more detail by creating a new data set of bulk sound speed residuals, which were calculated by combining S and P travel times for common source-receiver pairs. Using this technique, we created approximately 93,000 bulk sound speed residuals, using our S and P, Sdiff and Pdiff, and SS-S and PP-P data sets. In order to compare the effects of earthquake location on the correlation between shear velocity and bulk sound speed,

we also created two additional data sets of bulk sound speed residuals using the EHB locations and the EHB locations corrected for finite-frequency effects. Plots of residuals at their turning points show that coverage is fairly good at the base of the mantle but gets worse with decreasing depth, with large parts of the Southern Hemisphere remaining unsampled. Scatterplots of the S versus the bulk sound speed residuals show a negative correlation at the base of the mantle. The extent of the negative correlation, however, is dependent on the set of earthquake locations used, with the residuals made using the EHB locations remaining negatively correlated to much shallower depths. The residuals made using the corrected EHB locations behave similarly to the new locations, implying that one should not use earthquake locations determined using short-period data for long-period data, due to the apparent shift in origin time. Due to limited coverage of the bulk sound speed residuals in the lower mantle, bulk sound speed models are poorly resolved, particularly in the Southern Hemisphere. This technique should become more useful, however, as the data set grows.

We also jointly inverted for bulk sound speed and shear velocity using projected data, which are insensitive to location. Since we were not limited to using matching S and P pairs, we were able to use our entire data set, which provides much better coverage of the entire mantle. Consequently, the resulting models are much better resolved, giving us a much stronger constraint on the correlation between shear velocity and bulk sound speed. For the joint inversion, shear velocity and bulk sound speed are negatively correlated to a depth of 2000 km, indicating the presence of chemical or phase heterogeneity in the bottom 800 km off the mantle.

In the last chapter, we compared models of the lower mantle made using ray theory and finite-frequency kernels. Models derived from our data show that the shear models are very similar, with the largest differences occurring at the base of the mantle at short wavelengths. The compressional models correlate less well, with differences in the shape of the large slow velocity anomalies underneath the Pacific. In comparison to the S models, the P models exhibit greater differences higher up into the mantle. To test how finite frequency kernels change the correlation between shear velocity and bulk

sound speed, we did a joint inversion for shear velocity and bulk sound speed. The resulting model is similar to existing models, with the anti-correlation between shear velocity and bulk sound speed starting at a depth of approximately 2000 km.

The cause of the chemical or phase heterogeneity implied by the anti-correlation is unknown at this time. It is unlikely, however, to be due to the perovskite to post-perovskite phase transition. First principles calculations predict a 2-4% increase in shear velocity and a $\pm 0.5\%$ change in compressional velocity (Tsuchiya et al., 2004; Stackhouse et al., 2005; Wentzcovitch et al., 2006), implying that the increase in shear modulus is much larger than the increase in bulk modulus. Furthermore, the phase transition is strongly temperature dependent and may not even occur in hotter regions of the lowermost mantle (e.g. Wookey et al., 2005). Our models, however, show an increase in bulk sound speed and a corresponding decrease in shear velocity in the large slow shear velocity anomalies underneath the Pacific and Africa, which is the opposite of what is predicted. Wookey et al. (2005) suggest that since velocities in tomographic models are given relative to a global average at each depth, the velocity changes predicted by the phase transition to post-perovskite could result in anti-correlation between shear velocity and bulk sound speed. Houser (2007), however, found that a post-perovskite phase transition is unable to explain the observed relative variation between shear velocity and compressional velocity and that a chemical contribution is still necessary. Furthermore, although the depth extent of post-perovskite is not well constrained, the anti-correlation between shear velocity and bulk sound speed starts at much shallower depths than predicted for the post-perovskite phase transition (e.g. Murakami et al., 2005; Hirose et al., 2006).

## 6.2 Future Work

As we have seen, earthquake location error can significantly change the results of our inversions. This gives us an incentive to obtain the best set of earthquake locations possible. Due to the inclusion of depth phase travel time measurements, the locations of

our deep earthquakes are very well constrained. The locations, and in particular, depths, of shallow earthquakes, however, can still be improved upon. One approach is to modify our method of earthquake relocation to incorporate the nonlinear behavior of travel time as a function of source location. Standard location algorithms, which employ the Gauss-Newton method, are prone to failure (Thurber, 1985). In particular, the depths of very shallow earthquakes are poorly constrained, often resulting in above-ground earthquakes (Thurber, 1985). In tests on synthetic data, Thurber (1985) investigated the possibility of using Newton's method for earthquake location by including second-order partial derivatives and found that they improved the stability of the location algorithm. In our relocations, we dealt with above-ground earthquakes by limiting how far the source was allowed to move in depth. An alternative, and possibly better approach, may be to incorporate second-order partial derivatives instead.

Much of our work has focused on improving resolution at the base of the mantle and constraining the depth extent of the negative correlation between shear velocity and bulk sound speed. We have not, however, investigated the cause of the chemical and/or phase heterogeneity believed to exist at the base of the mantle. Houser (2005) modeled thermo-chemical heterogeneity using seismic tomography. Incorporating our diffracted travel time data sets into such an inversion could improve resolution at the base of the mantle and improve our understanding of the composition of the base of the mantle.

Models derived from our data show that models made using finite frequency kernels do differ from ray-theoretical models, particularly when using Pdiff data. Our finite frequency models, however, used ray theory for all of the non-diffracted phases. A natural extension of this work would be to use finite frequency kernels for our entire data set. Finally, our joint inversion for shear velocity and bulk sound speed using finite frequency kernels was done using our new set of earthquake locations. A joint inversion using projected finite frequency data was not included in Chapter 5, since it is very computationally expensive, but could be done in the future.

# References


Aki, K., and Richards, P. G., 1980: *Quantitative seismology, theory and methods*. W. H. Freeman, San Francisco.

Alexander, S., and Phinney, R. A., 1966: A study of the core-mantle boundary using P waves diffracted by the earth's core. *J. Geophys. Res.*, **71**, 5943–5958.

Antolik, M., Ekström, G., and Dziewonski, A., 2001: Global event location with full and sparse datasets using three-dimensional models of mantle P wave velocity. *Pure Appl. Geophys.*, **158**, 291–317.

Antolik, M., Gu, Y. J., Ekstrom, G., and Dziewonski, A. M., 2003: J362d28: a new joint model of compressional and shear velocity in the Earth's mantle. *Geophysical J. Int.*, **153**(2), 443–466.

Bassin, C., Laske, G., and Masters, G., 2000: The current limits of resolution for surface wave tomography in north america. *EOS Trans AGU*, **81**.

Bataille, K., Wu, R., and Flatte, S. M., 1990: Inhomogeneities near the core-mantle boundary evidenced from scattered waves: A review. *Pure Appl. Geophys.*, **132**, 151–174.

Beghein, C., Resovsky, J., and Trampert, J., 2002: P and S tomography using normal-mode and surface waves data with a neighbourhood algorithm. *Geophysical J. Int.*, **149**, 646–658.

Bijwaard, H., Spakman, W., and Engdahl, E. R., 1998: Closing the gap between regional and global travel time tomography. *J. Geophysical Research-solid Earth*, **103**(B12), 30055–30078.

Bolton, H., and Masters, G., 2001: Travel times of P and S from the global digital seismic networks: Implications for the relative variation of P and S velocity in the mantle. *J. Geophysical Research-solid Earth*, **106**(B7), 13527–13540.

Bolton, M., Storchak, D., and Harris, J., 2006: Updating default depths in the ISC bulletin. *Phys. Earth Planetary Interiors*, **158**, 27–45.

Bondar, I., Myers, S., Engdahl, E., and Bergman, E., 2004: Epicentre accuracy based on seismic network criteria. *Geophys. J. Int.*, **156**, 483–496.

Boschi, L., and Dziewonski, A. M., 2000: Whole Earth tomography from delay times of P, PcP, and PKP phases: Lateral heterogeneities in the outer core or radial anisotropy in the mantle? *J. Geophysical Research-solid Earth*, **105**(B6), 13675–13696.

Brodholt, J., Helffrich, G., and Trampert, J., 2007: Chemical versus thermal heterogeneity in the lower mantle: the most likely role of anelasticity. *Earth Planetary Science Lett.*, **262**, 429–437.

Buland, R., 1976: Mechanics of locating earthquakes. *Bulletin Seismological Soc. Am.*, **66**(1), 173–187.

Bullen, K., 1949: Compressibility-pressure hypothesis and the Earth's interior. *Month. Not. R. Astr. Soc., Geophys. Suppl.*, **5**, 355–368.

Chapman, C., and Phinney, R., 1972: Diffracted seismic signals and their numerical solution. *Methods in Computational Physics*, **12**, 165–230.

Chapman, C. H., and Phinney, R. A., 1970: Diffraction of P waves by core and an inhomogeneous mantle. *Geophysical J. Royal Astronomical Soc.*, **21**(2), 185–205.

Creager, K., and Boyd, T., 1992: Effects of earthquake mislocation on estimates of velocity structure. *Phys. Earth Planetary Interiors*, **75**, 63–76.

Dahlen, F. A., Nolet, G., and Hung, S.-H., 2000: Fréchet kernels for finite-frequency traveltimes – I. Theory. *Geophys. J. Int.*, **141**, 157–174.

Davies, G. F., and Gurnis, M., 1986: Interaction of mantle dregs with convection - lateral heterogeneity at the core mantle boundary. *Geophysical Research Lett.*, **13**(13), 1517–1520.

Davies, J. H., 1992: Lower bound estimate of average earthquake mislocation from variance of travel-time residuals. *Phys. Earth Planetary Interiors*, **75**(1-3), 89–101.

Doornbos, D. J., and Mondt, J. C., 1979: P-waves and S-waves diffracted around the core and the velocity structure at the base of the mantle. *Geophysical J. Royal Astronomical Soc.*, **57**(2), 381–395.

Duwalo, G., and Jacobs, J., 1959: Effects of a liquid core on the propagation of seismic waves. *Can. J. Phys.*, **37**, 109–128.

Dziewonski, A., 1984: Mapping the lower mantle: determination of lateral heterogeneity in P velocity up to degree and order 6. *J. Geophys. Res.*, **89**, 5929–5952.

Dziewonski, A. M., and Anderson, D. L., 1983: Travel-times and station corrections for P-waves at teleseismic distances. *J. Geophysical Research*, **88**(NB4), 3295–3314.

Engdahl, E., van der Hilst, R., and Buland, R., 1998: Global teleseismic earthquake relocation with improved travel times and procedures for depth determination. *Bull. Seism. Soc. Am.*, **88**, 722–743.

Engdahl, E. R., 2006: Application of an improved algorithm to high precision relocation of ISC test events. *Phys. Earth Planetary Interiors*, **158**(1), 14–18.

Engdahl, E. R., and Gubbins, D., 1987: Simultaneous travel time inversion for earthquake location and subduction zone structure in the central aleutian islands. *J. Geophysical Research-solid Earth Planets*, **92**(B13), 13855–13862.

Fujita, K., Engdahl, E. R., and Sleep, N., 1981: Subduction zone calibration and teleseismic relocation of thrust zone events in the central aleutian islands. *Bull Seism. Soc. Am.*, **71**, 1805–1828.

Garnero, E., 2000: Heterogeneity of the lowermost mantle. *Annu. Rev. Earth Planet. Sci.*, **28**, 477–507.

Grand, S., 1997: Mantle shear structure beneath the Americas and surrounding oceans. *J. Geophys. Res.*, **99**, 11591–11621.

Haddon, R., and Cleary, J. R., 1974: Evidence for scattering of seismic PKP waves near the mantle-core boundary. *Physics of the Earth and Planetary Interiors*, **8**, 211–234.

He, X., and Tromp, J., 1996: Normal-mode constraints on the structure of the Earth. *J. Geophysical Research*, **101**, 20053–20082.

Hernlund, J. W., and Houser, C., 2008: The statistical distribution of seismic velocities in Earth's deep mantle. *Earth Planetary Science Lett.*, **265**(3-4), 423–437.

Hirose, K., 2007: Discovery of post-perovskite phase transition and the nature of the D" layer. In *Post-Perovskite: The last mantle phase transition, Geophysical Monograph Series*, volume 174, 19–35. AGU,Washington D.C.

Hirose, K., Sinmyo, R., Sata, N., and Ohishi, Y., 2006: Determination of post-perovskite phase transition boundary in MgSiO3 using Au and MgO pressure standards. *Geophys. Res. Lett.*, **33**, doi:10.1029/2005GL024468.

Houser, C., 2005: *New Techniques for Analyzing Long-Period Seismic Data to Determine 3D Thermal and Compositional Structure of the Earths Mantle*. Ph.D. thesis, University of California San Diego.

Houser, C., 2007: Constraints on the presence or absence of post-perovskite in the lowermost mantle from long-period seismology. In *Post-Perovskite: The last mantle phase transition, Geophysical Monograph Series*, volume 174, 191–215. AGU,Washington D.C.

Houser, C., Masters, G., Shearer, P., and Laske, G., 2008: Shear and compressional velocity models of the mantle from cluster analysis of long-period waveforms. *Geophys. J. Int.*, **174**, 195–212.

Hung, S.-H., Dahlen, F. A., and Nolet, G., 2000: Fréchet kernels for finite-frequency traveltimes – II. Examples. *Geophys. J. Int.*, **141**, 175–203.

Ishii, M., and Tromp, J., 1999: Normal-mode and free-air gravity constraints on lateral variations in velocity and density of Earth's mantle. *Science*, **285**(5431), 1231–1236.

Ishii, M., and Tromp, J., 2001: Even-degree lateral variations in the Earth's mantle constrained by free oscillations and the free-air gravity anomaly. *Geophysical J. Int.*, **145**(1), 77–96.

Ishii, M., and Tromp, J., 2004: Constraining large-scale mantle heterogeneity using mantle and inner-core sensitive normal modes. *Phys. Earth Planetary Interiors*, **146**(1-2), 113–124.

Kanamori, H., and Anderson, D. L., 1975: Theoretical basis of some empirical relations in seismology. *Bulletin Seismological Soc. Am.*, **65**(5), 1073–1095.

Karason, H., and van der Hilst, R. D., 2001: Tomographic imaging of the lowermost mantle with differential times of refracted and diffracted core phases (PKP, p-diff). *J. Geophysical Research-solid Earth*, **106**(B4), 6569–6587.

Karato, S., and Karki, B. B., 2001: Origin of lateral variation of seismic wave velocities and density in the deep mantle. *J. Geophysical Research-solid Earth*, **106**(B10), 21771–21783.

Kellogg, L. H., Hager, B. H., and van der Hilst, R. D., 1999: Compositional stratification in the deep mantle. *Science*, **283**(5409), 1881–1884.

Kendall, J. M., and Shearer, P. M., 1994: Lateral variations in D" thickness from long-period shear-wave data. *J. Geophysical Research-solid Earth*, **99**(B6), 11575–11590.

Kendall, J. M., and Silver, P. G., 1996: Constraints from seismic anisotropy on the nature of the lowermost mantle. *Nature*, **381**(6581), 409–412.

Kennett, B., Engdahl, E., and Buland, R., 1995: Constraints on seismic velocities in the Earth from travel times. *Geophys. J. Int.*, 429–465.

Kennett, B. L. N., 2006: Non-linear methods for event location in a global context. *Phys. Earth Planetary Interiors*, **158**(1), 46–54.

Kennett, B. L. N., and Engdahl, E. R., 1991: Traveltimes for global earthquake location and phase identification. *Geophysical J. Int.*, **105**(2), 429–465.

Kennett, B. L. N., and Gudmundsson, O., 1996: Ellipticity corrections for seismic phases. *Geophysical J. Int.*, **127**(1), 40–48.

Kennett, B. L. N., Widiyantoro, S., and van der Hilst, R. D., 1998: Joint seismic tomography for bulk sound and shear wave speed in the Earth's mantle. *J. Geophysical Research-solid Earth*, **103**(B6), 12469–12493.

Kissling, E., 1988: Geotomography with local earthquake data. *Rev. Geophys.*, **26**, 659–698.

Knittle, E., and Jeanloz, R., 1991: Earths core-mantle boundary - results of experiments at high-pressures and temperatures. *Science*, **251**(5000), 1438–1443.

Komatitsch, D., and Tromp, J., 2002a: Spectral-element simulations of global seismic wave propagation-I. validation. *Geophys. J. Int.*, **149**, 390–412.

Komatitsch, D., and Tromp, J., 2002b: Spectral-element simulations of global seismic wave propagation-II. 3-D models, oceans, rotation, and self-gravitation. *Geophys. J. Int.*, **150**, 303–318.

Laske, G., and Masters, G., 1996: Constraints on global phase velocity maps from long-period polarization data. *J. Geophys. Res.*, **101**, 16,05916,075.

Lay, T., and Helmberger, D., 1983: A lower mantle S-wave triplication and the velocity structure of D". *Geophys. J. R. astron. Soc.*, **75**, 799–837.

Li, C., van der Hilst, R. D., and Toksoz, A. N., 2006: Constraining P-wave velocity variations in the upper mantle beneath Southeast asia. *Phys. Earth Planetary Interiors*, **154**(2), 180–195.

Liu, Q., and Tromp, J., 2006: Finite-frequency Kernels based upon adjoint method. *Bull. Seism. Soc. Am.*, **96**(6), 2383–2397.

Liu, Q., and Tromp, J., 2008: Finite-frequency sensitivity kernels for global seismic wave propagation based upon adjoint methods. *Geophys. J. Int.* Accepted.

Manners, U., and Masters, G., 2008a: A comparison of methods for global teleseismic earthquake relocation.

Manners, U., and Masters, G., 2008b: Analysis of core-mantle boundary structure using S and P diffracted waves.

Masters, G., Laske, G., Bolton, H., and Dziewonski, A., 2000: The relative behavior of shear velocity, bulk sound speed, and compressional velocity in the mantle: implications for chemical and thermal structure. In *Earth's Deep Interior: Mineral Physics and Tomography From the Atomic to the Global Scale, Geophys. Monograph Ser.*, volume 117, 63–87. AGU, Washington, DC.

McSweeney, T., 1995: *Seismic constraints on core structure and dynamics*. Ph.D. thesis, Univ. of Wash., Seattle.

Megnin, C., and Romanowicz, B., 2000: The three-dimensional shear velocity structure of the mantle from the inversion of body, surface and higher-mode waveforms. *Geophysical J. Int.*, **143**(3), 709–728.

Montelli, R., Nolet, G., Dahlen, F. A., and Masters, G., 2006: A catalogue of deep mantle plumes: New results from finite-frequency tomography. *Geochemistry Geophysics Geosystems*, **7**.

Montelli, R., Nolet, G., Masters, G., Dahlen, F., and Hung, S., 2004a: Finite-frequency tomography reveals a variety of plumes in the mantle. *Science*, **303**, 338–343.

Montelli, R., Nolet, G., Masters, G., Dahlen, F., and Hung, S., 2004b: Global P and PP traveltime tomography: rays versus waves. *Geophys. J. Int.*, **158**, 637–654.

Mula, A. H. G., 1981: Amplitudes of diffracted long-period P-waves and S-waves and the velocities and Q-structure at the base of the mantle. *J. Geophysical Research*, **86**(NB6), 4999–5011.

Murakami, M., Hirose, K., Kawamura, K., Sata, N., and Ohishi, Y., 2004: Post-perovskite phase transition in MgSiO3. *Science*, **304**(5672), 855–858.

Murakami, M., Hirose, K., Sata, N., and Ohishi, Y., 2005: Post-perovskite phase transition and mineral chemistry in the pyrolitic lowermost mantle. *Geophys. Res. Lett.*, **32**, doi:10.1029/2004GL021956.

Nataf, H. C., and Houard, S., 1993: Seismic discontinuity at the top of D" - a worldwide feature. *Geophysical Research Lett.*, **20**(21), 2371–2374.

Nicholson, T., 2006: Application of 3D empirical travel times to routine event location. *Phys. Earth Planetary Interiors*, **158**(1), 67–74.

Nicholson, T., Sambridge, M., and Gudmundsson, O., 2004: Three-dimensional empirical traveltimes: construction and applications. *Geophysical J. Int.*, **156**(2), 307–328.

Nieman, T., Fujita, K., and Rogers, W., 1986: Teleseismic mislocation of earthquakes in island arcs - theoretical results. *J. Phys. Earth*, **34**, 43–70.

Nissen-Meyer, T., Fournier, A., and Dahlen, F. A., 2007: A 2-D spectral-element method for computing spherical-earth seismograms–I. Moment-tensor source. *Geophys. J. Int.*, **168**, 1067–1093.

Nissen-Meyer, T., Fournier, A., and Dahlen, F. A., 2008: A 2-D spectral-element method for computing spherical-earth seismograms–II. Waves in solid-fluid media. *Geophys. J. Int.* In press.

Nolet, G., and Dahlen, F., 2000: Wavefront healing and the evloution of seismic delay times. *J. Geophys. Res.*, **105**, 19043–19054.

Nolet, G., Dahlen, F., and Montelli, R., 2005: Traveltimes and amplitudes of seismic waves: a re-assessment. In *Array analysis of broadband seismograms, AGU Monograph Ser.*, 37–48. AGU, Washington, DC.

Oganov, A. R., and Ono, S., 2004: Theoretical and experimental evidence for a post-perovskite phase of MgSiO3 in Earth's D " layer. *Nature*, **430**(6998), 445–448.

Oki, S., Fukao, Y., and Obayashi, M., 2004: Reference frequency of teleseismic body waves. *J. Geophysical Research-solid Earth*, **109**(B4).

Paige, C., and Saunders, M., 1973: Solution of sparse indefinite systems of equations and least squares problems. *Res. Rep*.

Panning, M., and Romanowicz, B., 2006: A three-dimensional radially anisotropic model of shear velocity in the whole mantle. *Geophysical J. Int.*, **167**(1), 361–379.

Pavlis, G. L., and Booker, J. R., 1980: The mixed discrete-continuous inverse problem - application to the simultaneous determination of earthquake hypocenters and velocity structure. *J. Geophysical Research*, **85**(NB9), 4801–4810.

Phinney, R., and Alexander, S., 1969: The effect of a velocity gradient at the base of the mantle on diffracted P waves in the shadow. *J. Geophys. Res.*, **74**, 4967–4971.

Phinney, R. A., and Alexander, S., 1966: P wave diffraction theory and structure of core-mantle boundary. *J. Geophysical Research*, **71**(24), 5959–5975.

Phinney, R. A., and Cathles, L. M., 1969: Diffraction of P by core - a study of long-period amplitudes near edge of shadow. *J. Geophysical Research*, **74**(6), 1556–1574.

Resovsky, J., and Ritzwoller, M. H., 1998: New and refined constraints on three-dimensional Earth structure from normal modes below 3 mHz. *J. Geophysical Research*, **103**, 783–810.

Revenaugh, J., and Jordan, T. H., 1991: Mantle layering from ScS reverberations: 4. The lower mantle and core-mantle boundary. *J. Geophysical Research-solid Earth*, **96**(B12), 19811–19824.

Ritsema, J., van Heijst, H., and Woodhouse, J., 1999: Complex shear velocity structure imaged beneath Africa and Iceland. *Science*, **286**, 1925–1928.

Ritsema, J., and van Heijst, H. J., 2002: Constraints on the correlation of P- and S-wave velocity heterogeneity in the mantle from P, PP, PPP and PKPab traveltimes. *Geophysical J. Int.*, **149**(2), 482–489.

Ritzwoller, M. H., Shapiro, N. M., Levshin, A. L., Bergman, E. A., and Engdahl, E. R., 2003: Ability of a global three-dimensional model to locate regional events. *J. Geophysical Research-solid Earth*, **108**(B7).

Robertson, G. S., and Woodhouse, J. H., 1995: Evidence for proportionality of P and S heterogeneity in the lower mantle. *Geophysical J. Int.*, **123**(1), 85–116.

Robertson, G. S., and Woodhouse, J. H., 1996: Ratio of relative S to P velocity heterogeneity in the lower mantle. *J. Geophysical Research-solid Earth*, **101**(B9), 20041–20052.

Rodi, W., 2006: Grid-search event location with non-Gaussian error models. *Phys. Earth Planetary Interiors*, **158**(1), 55–66.

Saltzer, R., van der Hilst, R., and Karason, H., 2001: Comparing P and S wave heterogeneity in the mantle. *Geophys. Res. Lett.*, **28**, 1335–1338.

Scholte, J., 1956: On seismic waves in a spherical earth. *Koninkl. Ned. Meterol. Inst. Publ.*, **65**.

Shearer, P., Hedlin, M., and Earle, P., 1998: PKP and PKKP precursor observations: Implications for the small-scale structure of the deep mantle and core. In *The Core-Mantle Boundary region, AGU Geodynamics series*, volume 28, 37–55. AGU,Washington D.C.

Simmons, N. A., Forte, A. M., and Grand, S. P., 2006: Constraining mantle flow with seismic and geodynamic data: A joint approach. *Earth Planetary Science Lett.*, **246**(1-2), 109–124.

Smith, G., and Ekström, G., 1996: Improving teleseismic event locations using a three-dimensional earth model. *Bulletin of the Seismological Society of America*, **86**, 788–796.

Spencer, C., and Gubbins, D., 1980: Travel-time inversion for simultaneous earthquake location and velocity structure determination in laterally varying media. *Geophys. J. R. Astr. Soc.*, **63**, 95–116.

Stackhouse, S., Brodholt, J., Wookey, J., Kenall, J., and Price, G., 2005: The effect of temperature on the seismic anisotropy of the perovskite and post-perovskite polymorphs of MgSiO3. *Earth Planetary Science Lett.*, **230**, 1–10.

Su, W., and Dziewonski, A., 1997: Simultaneous inversion for 3-D variations in shear and bulk velocity in the mantle. *Phys. Earth Planet. Inter.*, **100**, 135–136.

Su, W., Woodward, R., and Dziewonski, A., 1994: Degree-12 model of shear velocity heterogeneity in the mantle. *J. Geophys. Res.*, **99**, 6945–6980.

Thurber, C., 1985: Nonlinear earthquake location: Theory and examples. *Bull. Seism. Soc. Am.*, **75**, 779–790.

Thurber, C., 1992: Hypocenter-velocity structure coupling in local earthquake tomography. *Phys. Earth Planet. Inter.*, **75**, 55–62.

Tromp, J., Tape, C. H., and Liu, Q., 2005: Seismic tomography, adjoint methods, time reversal, and banana-doughnut kernels. *Geophys. J. Int.*, **160**, 195–216.

Tsuchiya, T., Tsuchiya, J., Umemoto, K., and Wentzcovitch, R., 2004: Phase transition in MgSiO3 perovskite in the Earth's lower mantle. *Earth planet. Sci. Lett.*, **224**, 241–248.

Valenzuela, R. W., Wysession, M. E., Neustadt, M. O., and Butler, J. L., 2000: Lateral variations at the base of the mantle from profiles of digital S-diff data. *J. Geophysical Research-solid Earth*, **105**(B3), 6201–6220.

van der Hilst, R. D., and Engdahl, E. R., 1992: Step-wise relocation of isc earthquake hypocenters for linearized tomographic imaging of slab structure. *Phys. Earth Planetary Interiors*, **75**(1-3), 39–53.

van der Hilst, R. D., and Karason, H., 1999: Compositional heterogeneity in the bottom 1000 kilometers of Earth's mantle: Toward a hybrid convection model. *Science*, **283**(5409), 1885–1888.

Vasco, D. W., and Johnson, L. R., 1998: Whole earth structure estimated from seismic arrival times. *J. Geophysical Research-solid Earth*, **103**(B2), 2633–2671.

Vinnik, L., Romanowicz, B., Lestunff, Y., and Makeyeva, L., 1995: Seismic anisotropy in the D" layer. *Geophysical Research Lett.*, **22**(13), 1657–1660.

Wentzcovitch, R., Tsuchiya, T., and Tsuchiya, J., 2006: MgSiO3 postperovskite at the D" conditions. *Proc. Nat. Acad. Sci.*, **103**, 543–546.

Woodward, R. L., and Masters, G., 1992: Upper mantle structure from long-period differential travel-times and free oscillation data. *Geophysical J. Int.*, **109**(2), 275–293.

Wookey, J., Stackhouse, S., Kendall, J. M., Brodholt, J., and Price, G. D., 2005: Efficacy of the post-perovskite phase as an explanation for lowermost-mantle seismic properties. *Nature*, **438**(7070), 1004–1007.

Wysession, M. E., 1996: Large-scale structure at the core-mantle boundary from diffracted waves. *Nature*, **382**(6588), 244–248.

Zhao, L., and Jordan, T. H., 2006: Structure sensitivities of finite-frequency seismic waves: A full-wave approach. *Geophys. J. Int.*, **165**, 981–990.

Zhao, L., Jordan, T. H., and Chapman, C. H., 2000: Three-dimensional Frèchet differential kernels for seismic delay times. *Geophys. J. Int.*, **141**, 558–576.

Zhou, Y., Nolet, G., and Dahlen, F., 2006: Global upper-mantle structure from finite-frequency surface-wave tomography. *J. Geophysical Research*, **111**, doi:10.1029/2005JB003677.